FOSSIL ENERGY

DOE/BC/14851-3
(OSTI ID: 15156)

PREDICTION OF GAS INJECTION PERFORMANCE FOR HETEROGENEOUS RESERVOIRS

Annual Report
October 1, 1998-September 30, 1999

By
Martin J. Blunt
Franklin M. Orr Jr.

Date Published: December 1999

Work Performed Under Contract No. DE-FG22-96BC14851

Stanford University
Stanford, California

National Petroleum Technology Office
U. S. DEPARTMENT OF ENERGY
Tulsa, Oklahoma

DISCLAIMER

This report was prepared as an account of work sponsored by an agency of the United States Government. Neither the United States Government nor any agency thereof, nor any of their employees, makes any warranty, expressed or implied, or assumes any legal liability or responsibility for the accuracy, completeness, or usefulness of any information, apparatus, product, or process disclosed, or represents that its use would not infringe privately owned rights. Reference herein to any specific commercial product, process, or service by trade name, trademark, manufacturer, or otherwise does not necessarily constitute or imply its endorsement, recommendation, or favoring by the United States Government or any agency thereof. The views and opinions of authors expressed herein do not necessarily state or reflect those of the United States Government.

This report has been reproduced directly from the best available copy.

DOE/BC/14851-3
Distribution Category UC-122

Prediction of Gas Injection Performance for Heterogeneous Reservoirs

By
Martin J. Blunt
Franklin M. Orr, Jr.

December 1999

Work Performed Under Contract No. DE-FG22-96BC14851

Prepared for
U.S. Department of Energy
Assistant Secretary for Fossil Energy

Purna Halder, Project Manager
National Petroleum Technology Office
P.O. Box 3628
Tulsa, OK 74101

Prepared by
Stanford University
Department of Petroleum Engineering
Stanford, CA 94305-2220

Contents

List of Tables v
List of Figures vii
Acknowledgements xi
1 Introduction 1
2 Three-Phase Relative Permeability of Water-Wet, Oil-Wet, and Mixed-Wet Sandpacks 3
2.1 Introduction 3
2.2 Materials and Methods 4
2.2.1 Capillary Pressure Curves 5
2.2.2 Oil and Water Relative Permeabilities 6
2.2.3 Gas Relative Permeability 8
2.3 Results 9
2.3.1 Capillary Pressure Curves 9
2.3.2 Three-Phase Relative Permeability 10
2.4 Pore Scale Explanation 14
2.5 Discussions 20
2.6 Conclusions 20
2.7 Nomenclature 21

3. Fast Approximate Solutions for 1D Multicomponent Gas Injection Problems 23
3.1 Introduction 23
3.2 Analytical Theory of 1D Miscible Displacements 24
3.3 Self-Sharpening Systems 25
3.4 Solution Example for Fully Self-Sharpening System 28
3.5 Systems with Nontie-Line Rarefactions 30
3.6 Prediction of Spreading Waves in 1D Solutions 31
3.7 The Fanning Rule (Envelope Rule) 32
3.8 Algorithm for Systems with Nontie-line Rarefactions 34
3.9 Solution Example with Nontie-line Rarefaction 35
3.10 Conclusions 35
3.11 Nomenclature 37

4. Nested Gridding and Streamline Simulation 39
4.1 Introduction 39
4.2 The streamline method 41
4.3 Description of the new method 43
4.3.1 The upscaling step 44
4.3.2 Pressure solve on the coarse grid 46
4.3.3 Computation of the pressure on the fine grid 46

4.4 CPU cost evaluation for the nested gridding method 47
4.5 CPU requirements of different pressure solvers 49
4.6 Results 51
4.6.1 Numerical results for two-dimensional reservoirs 52
4.6.2 Numerical results for three-dimensional reservoirs 56
4.7 Discussion and conclusions 61

List of Tables

2.1 Interfacial tensions 5
2.2 Wettability Indices 9
2.3 Experiments 10

3.1 Characterized fluid description (SRK - Equation of state) 29
3.2 MOC solution for displacement of Oil A by Gas A at 275 atm and 387 K 29
3.3 Summary of the fanning (envelope) rule 34
3.4 Comparison of tie line found by MOC integration and by the tie line intersection approach. Gas A displaced by pure N_2 at 275 atm and 387 K 36

4.1 CPU time (in *s*) and memory (in MB) comparisons for a pressure solve on *3D* permeability fields of varying size 42
4.2 Speed-up factor and memory requirements of the nested grid method for a pressure solve and for the whole simulation on the two *2D* examples presented in the chapter 56
4.3 Speed-up factor and memory requirements of the nested gridding method for a pressure solve and for the whole simulation on the *3D* example presented in the chapter. The numbers in parenthesis in the third column are speed-up factors for the case where $N_g = 2$ 61

List of Figures

2.1 Oil (octane) and water saturation profiles versus time during gravity drainage. The sand was water-wet and the initial condition was connate water saturation S_{wc}. Oil and water permeabilities can be calculated directly from the measured distributions 7

2.2 Measured two-phase (water/oil) capillary pressure curves and three-phase oil and water relative permeabilities with n-octane as the oil for water-wet, oil-wet, mixed-wet, and fractionally-wet sand. Open symbols are drainages which started from residual oil saturation (S_{or}), and closed symbols are drainages which started from connate water saturation (S_{wc}) 11

2.3 Measured oil relative permeabilities with hexane, octane, and decane as the oil in water-wet sand and with octane in water-wet sandstone[58] during three-phase gravity drainage 12

2.4 Measured water relative permeabilities for a) the two-phase (gas/water) system and for b) the three-phase (gas/oil/water) system from gravity drainages in water-wet sand 13

2.5 Measured gas relative permeabilities for a) the two-phase gas/water system for media of varying wettability and the two-phase gas/oil system for oil-wet media, and for b) the three-phase gas/oil/water system for water-wet and oil-wet media. The gas relative permeability in oil-wet sand is roughly a factor of two smaller than that for identical water-wet sand for two-phase gas/water systems 13

2.6 Configuration of fluids on : a) a flat water-wet surface, b) a flat oil-wet surface (shown bold) 16

2.7 Possible configuration of fluids in a pore space corner of half-angle, β: a) water-wet surfaces, b) oil-wet surfaces (shown bold). Note that configuration b) is not allowed as $\Theta_{gw} > 90°$ 16

2.8 Pore-scale arrangements of fluid for water-wet, oil-wet, and mixed-wet corners. A thick line represents an oil-wet surface. Notice that oil layers sandwiched between water and gas are present for both the water-wet and mixed-wet media, leading to similar k_{ro} at low S_{or}. In oil-wet media, oil is confined to the crevices, leading to a lower k_{ro} 18

2.9 Comparison of relative permeabilities. (a) A spreading system ($\Theta_{go} \approx 0$) : Octane in water-wet sand. (b) A nonspreading system : Decane in water-wet sand. (e) A nonwetting system : Water in oil-wet sand. (d) A mixed-wet system : Octane in mixed-wet sand. The solid lines in (a) and (d) show $k_{ro} \sim S_o^2$. The data, while consistent with this trend, only follows it approximately 19

3.1 Construction of tangent shocks 26

3.2 Illustration of downstream solution path construction 27

3.3 Comparison of analytical and numerical saturation profiles for displacement of Oil A by Gas A at 275 atm and 387.45 K. The finite difference (FD) solutions were obtained with 100, 1000, and 10,000 grid blocks and $\Delta z/\Delta t = 10$ 32

3.4 Illustration of envelope curve 32
3.5 Vaporizing wave with liquid side envelope. Upstream (u), Downstream (d) 33
3.6 Condensing wave with vapor side envelope 33
3.7 Condensing wave with liquid side envelope 33
3.8 Vaporizing wave with vapor side envelope 34
3.9 Comparison of analytical solutions (with and without integration) with numerical saturation profiles for the displacement of Oil A by pure n_2 at 275 atm and 387.45 K. The finite difference (FD) solutions were obtained using 100 and 10,000 grid blocks and $\Delta z/\Delta t = 10$ 36

4.1 Description of the streamline method. Consider a permeability map *(a)* with injector and a producer wells. Solve the pressure field *(b)*. Compute the velocity field and trace streamlines *(c)*. Move saturation along streamlines and compute the values of the saturation on the grid *(d)* 42
4.2 Representation of the coarse grid superimposed on a fine grid. The right figure represents a particular coarse grid block 43
4.3 Upscaling of the transmissivities: the fine transmissivity map is divided into coarse grid blocks. The pressure equation is solved independently on each coarse grid block with a no flux boundary on all the faces except two opposing faces across which a prescribed pressure drop is applied. The upscaled values of the transmissivities are then obtained from the computation of the flux across the system 45
4.4 Upscaling of the transmissivity in the three directions *(a-c)* where a constant pressure drop ΔP_d is applied on the direction d and the gravity is set to $g = 0$. (d) depicts the upscaling of the gravity transmissivity where $\Delta P_z = 0$ and $g \neq 0$ 45
4.5 Computation of the fine grid pressure field using the pressure of the coarse grid and the fluxes coming from the neighboring coarse grid blocks. The fluxes are computed using Darcy's law and are weighted by the inter-blocks transmissivities 46
4.6 Description of the different steps of the nested gridding method. We first consider a fine description of the reservoir *(a)*. The transmissivities are then upscaled on a coarse scale *(b)* and a pressure solution on the coarse grid is computed *(c)*. The next step is the computation of the pressure on the fine grid *(d)* which leads to the velocity field. The streamlines are traced from the injector to the producer *(e)* and saturation is moved using the classical streamline method *(f)* 48
4.7 *2D* grid with n_x., = 5, n_y = 5 and the corresponding transmissivity sparse matrix. Only nonzero elements are represented 49
4.8 *3D* grid with n_x., = 2, n_z= 5 and n., =: 5 and the corresponding sparse matrix. Only nonzero elements axe represented 50
4.9 Heterogeneous permeability fields (a), in a log-scale, used to compare the CPU time needed to solve the pressure. There are all extracted from a 600 x 500 permeability field. (b) is the CPU time comparison for a pressure solve using different solvers for *2D* problems 50

4.10 Permeability field containing 270 x 270 grid blocks with two facies. Permeability: *k*(black) = 100 *m*D and *k*(white) = 0.1 *m*D. Proportion of black facies: 90%. Correlation length: 10 grid blocks in the *x* and *y* directions with an anisotropy angle of 45° 52
4.11 Fractional flow of oil at the producer for different upscaling factors and for the three methods (fine grid, nested gridding and upscaling). Case *RES1* 52
4.12 Water saturation maps from the fine grid simulation *(a)*, from the nested gridding simulation *(b)* and from the simulation on the upscaled absolute permeabilities *(c)* for 0.35 *PVI*. The upscaling factor is 9 x 9. Case *RES1*..... 53
4.13 Permeability field containing 270 x 270 grid blocks with two facies. Permeability: *k*(black) = 100 *m*D and *k*(white) = 0.1 *m*D. Proportion of black facies: 90%. Correlation length: 20 grid blocks in the *x* and 2 grid blocks in the *y* direction..... 54
4.14 Fractional flow of oil at the producer for different upscaling factors and for the three methods (fine grid, nested gridding and upscaling). Case *RES2* 54
4.15 Water saturation maps from the fine grid simulation *(a)*, from the nested gridding simulation *(b)* and from the simulation on the upscaled absolute permeabilities *(c)* for 0.8 *PVI*. The upscaling factor is 27 x 27. Case *RES2*..... 55
4.16 Case *RES3*. 99 x 99 x 99 permeability field. The two wells are located on two opposing corners of the reservoir and they penetrate all the layers. The correlation length is equal to 2 grid blocks in all 3 directions. The permeability of the black facies is 100 *m*D and 0.1 *m*D for the white facies 57
4.17 Fractional flow of oil at the producer for different upscaling factors and for the three methods (fine grid, nested gridding and upscaling) for the case *RES3*. The gravity number is set to $N_g = 0$..... 58
4.18 Fractional flow of oil at the producer for different upscaling factors and for the three methods (fine grid, nested gridding and upscaling) for the case *RES3*. The gravity number is set to $N_g = 2$..... 58
4.19 Saturation maps for 0.15 *PVI* using the three methods (fine grid, nested gridding and upscaling) with an upscaling factor equal to (3 x 3 x 3). The gravity number is set to $N_g = 0$ 59
4.20 Saturation maps for 0.15 *PVI* using the three methods (fine grid, nested gridding and upscaling) with an upscaling factor equal to (3 x 3 x 3). The gravity number is set to $N_g = 2$ 60

Acknowledgements

We would like to thank the many students, post-docs and research associates who contributed to this work. There have been some changes in personnel this year. As of June 1999, Martin Blunt became Professor of Petroleum Engineering at Imperial College in London. His daily presence at Stanford and his energy and enthusiasm will be greatly missed, but we anticipate and look forward to active collaboration in the future. David DiCarlo, the research associate in charge of our experimental program, has been promoted to Acting Assistant Professor. Chapter 2 on three-phase relative permeability describes the work that he has performed over the last two years. He was also responsible for preparing this report. Chapter 3 on the analytical solutions for one-dimensional gas/oil displacements was the result of a lively collaboration of students and faculty from two institutions. Kristian Jessen, a PhD student from the Danish Technical University in Copenhagen, spent six months with our group this year, and during that time worked closely with current Stanford students Jichun Zhu and Pavel Ermakov to develop the automatic method for compositional displacements described in Chapter 3. Yun Wang, who received his PhD a year ago and is now working for Arco, started this work in his PhD research. We are also grateful to Dr. Michael Michelsen of the Danish Technical University for allowing us to make use of his very fast and robust algorithms for phase equilibrium calculations. Chapter 4 describes research performed by Yann Gautier, who is a research associate. He will be leaving to join the Institut Francais du Petrole in Paris at the end of the year. The work in Chapter 4 was a joint project with Mike Christie of BP Amoco, who has recently joined Heriot-Watt University in Scotland.

We would like to thank Yolanda Williams who somehow keeps our busy research group organized from an administrative and financial standpoint, and makes sure that our reports are on time.

We gratefully acknowledge the support of the Department of Energy under Grant No. DE-FG22-96BC14851. We thank Jerry Casteel, Purna Halder and their colleagues for their continued support and encouragement. We are also grateful for funding from the members of the SUPRI-C Gas Injection Affiliates Group: Arco, BP Amoco, Chevron, Elf, Exxon, Japan National Oil Corporation, Norsk Hydro and Statoil. Without this generous support this work would not have been possible.

Lynn Orr
Stanford
October 1999

1. Introduction

This report describes research carried out in the Department of Petroleum Engineering at Stanford University from September 1998 - September 1999 under the third year of a three-year grant from the Department of Energy on the "Prediction of Gas Injection Performance for Heterogeneous Reservoirs." The research effort is an integrated study of the factors affecting gas injection, from the pore scale to the field scale, and involves theoretical analysis, laboratory experiments and numerical simulation. The research is divided into four main areas: (1) Pore scale modeling of three phase flow in porous media; (2) Laboratory experiments and analysis of factors influencing gas injection performance at the core scale with an emphasis on the fundamentals of three phase flow; (3) Benchmark simulations of gas injection at the field scale; (4) Development of streamline-based reservoir simulator. The chapters that follow give a detailed account of our progress in these areas. We have now completed all the work planned in the original proposal, and in some areas, such as the solution of multicomponent gas injection problems, and the development of a nested gridding approach to streamline-based simulation, we have considerably extended the research beyond what was originally planned.

Chapter 2 describes the final phase of our work using CT scanning to measure three-phase relative permeabilities and represents the completion of our experimental effort under the proposal. We have extended our previous work to study mixed-wet systems. Here the wettability of a sand-pack is altered using a physically-based sequence of saturation changes that mimics the displacement processes observed in oil reservoirs. An initially water-filled and water-wet pack is flooded with a heavy crude oil/octane mixture. The pack is then left to age for several days. During this time, surface active components of the oil in direct contact with the solid surfaces of the pore space absorb to the surface and alter its wettability. Regions that remain water-filled or are protected by a thick wetting film of water remain water-wet. We then perform a series of three phase displacements and use CT scanning to measure the three phase relative permeabilities. The results are very intriguing and are compared with measurements on water-wet, uniformly oil-wet and fractionally-wet media. We show that having a physically-based pattern of wettability makes a significant difference to the relative permeabilities, compared to a medium where surfaces are either uniformly water- or oil-wet.

Chapter 3 represents a major advance in our research on analytical solutions to gas injection problems. Last year we presented a semi-analytical technique to predict the minimum miscibility pressure (MMP) for gas injection projects. Here we build on that method and develop an automatic procedure for finding the one-dimensional composition profile for gas injection below the MMP. The theory is based on method-of-characteristics solutions to the flow equations coupled with the phase behavior. The method can be used for gas and oil mixtures containing arbitrary numbers of chemical components. Injection, initial and cross-over tie lines are constructed for a general n component system. The method is considerably faster than direct compositional simulation and suffers from no numerical dispersion. While the method developed applies to systems in which components do not change volume as they transfer between phases, we are confident that we can extend the method to account for effects of volume change on mixing.

Chapter 4 reports extensions to our work on streamline-based simulation. We develop a nested-gridding technique that offers a direct alternative to upscaling. Both conventional and streamline-based simulation approaches are limited by the memory and computer time requirements to solve for the pressure field. We propose a method where the pressure field is found approximately. First the pressure is computed on a coarse grid using averaged mobilities. This pressure solution is then used as a boundary condition for finding the pressure within each coarse grid block. In this

way an approximate pressure distribution for the entire domain on the fine grid is computed. The velocity is everywhere continuous and streamlines are traced throughout the system. The fluids are transported along these streamlines and we account for the fine grid details of the flow field. In this way, all small scale details of the flow are captured, while being up to 10 times faster than streamline simulation on the full grid. Since the streamline method is itself around 100 times faster than grid-based approaches for displacement-type problems, the nested gridding approach offers huge speed advantages over conventional methods. Where traditionally upscaling, with its inherent inaccuracies may have been required to perform a simulation on a fine scale reservoir description, this approach offers the possibility of running simulations directly on the fine grid.

The work summarized in this report sets the stage for future work to combine better models of three-phase flow, analytical solutions of gas injection processes, and very fast streamline methods to create future reservoir simulation tools that are based on the physics of the displacements and are very efficient. The goal is to build physics-based techniques that give accurate predictions of displacement processes at field scale.

2. Three-Phase Relative Permeability of Water-Wet, Oil-Wet, and Mixed-Wet Sandpacks

David A. DiCarlo, Akshay Sahni, and Martin J. Blunt

In this chapter we present experimental studies of three-phase flow in water-wet, oil-wet, mixed-wet, and fractionally-wet sandpacks. In oil reservoirs, three-phase flow will occur during immiscible gas injection, gas cap expansion, and thermal flooding among other processes. All of these processes are affected by the wettability of the reservoir. We use sandpacks as our model porous medium, and affect the wettability of the sand by aging it in crude oil. We make the mixed-wet pack by invading a water-filled water-wet pack with crude oil and aging for a week. This process mimics wettability changes in reservoir settings, leading to a realistic arrangement of wettability at the pore scale. We characterize the wettability of each sand pack by measuring the capillary pressure curves. We obtain the oil and water relative permeabilites during three-phase gravity drainage, by measuring the saturation in-situ using CT scanning. In another experiment, we measure pressure gradients in the gas phase to obtain the gas relative permeability. Thus we determine all three relative permeabilities as a function of saturation for each wettability. We find that under uniform wetting, the relative permeabilities of the most-wetting phase (water in a water-wet pack, oil in an oil-wet pack) are similar. However, the relative permeabilities of the intermediate-wet phase (oil in a water-wet pack, water in a oil-wet pack) are very different at low saturations, with spreading oils showing a characteristic layer drainage regime. The mixed-wet pack also shows the layer drainage regime. We also find that the gas relative permeability is smaller in an oil-wet medium than in a water-wet medium. We explain the observations in terms of wetting, spreading, and the pore scale configurations of fluid.

2.1 Introduction

A knowledge of three-phase (water, oil, and gas) flow in porous media is essential for predicting enhanced oil recovery and the migration of nonaqueous phase pollutants. In two-phase flow, one phase will wet the porous medium more than the other phase. This wetting phase occupies the smaller pores, crevices, and corners while the nonwetting phase occupies the larger pores with the exact arrangement determined by the capillary pressure. Regardless of which pair of fluids is used (gas/water, oil/water, gas/oil) the positioning of the fluids are likely to be similar at the same saturations. In contrast, for three-phase flow there will be an intermediate wetting phase which will be positioned uniquely in the porous medium, affecting macroscopic properties such as relative permeability and residual saturation.

We measure three-phase relative permeabilities during the gravity driven displacement of oil and water by gas, which is called gravity drainage. This is an important three-phase process that occurs during gas cap expansion in an oil reservoir and when nonaqueous phase pollutants migrate through an unsaturated soil. Gravity drainage is also relatively easy to study experimentally and its analysis avoids consideration of hysteresis effects, which can be very significant in three-phase flow [60, 24].

Several authors[21, 37, 72] have shown that low oil saturations can be reached during three-phase displacements. Most experiments have been performed on uniformly water-wet media (see

[1]The material in this chapter will be published in SPEJ.

Baker[5] for a review). Oak *et al.*[47] studied three-phase relative permeabilities in an intermediate-wet Berea sandstone. Vizika and Lombard[69] studied three-phase drainage for water-wet, oil-wet, and fractionally-wet systems. Jerauld[32] developed a model for three-phase relative permeability based on two-phase measurements for Prudhoe Bay, which is a mixed-wet reservoir.

Sahni *et al.*[58] used CT scanning to measure oil and water relative permeability in water-wet media and studied the effect of spreading coefficient. Zhou and Blunt[73] performed three-phase gravity drainage in fractionally-wet sandpacks. They measured the saturation distribution at the end of drainage and interpreted the results in terms of the pore scale arrangement of fluid. DiCarlo *et al.*[17] measured three-phase relative permeabilities for oil-wet and fractionally-wet packs.

The fractionally-wet media studied in the literature were composed of mixtures of oil-wet and water-wet grains. While this is a convenient way of varying the wettability, it does not necessarily represent the real distribution of wettability in a natural setting. An alternative approach is to mimic a physical sequence of wettability changes in the laboratory, leading to a medium whose pore-scale pattern of wettability represents reservoir rocks. This is achieved by flooding a water-wet water-filled pack with a crude oil and then aging for several days. This induces a wettability change on the sand surfaces contacted by oil (see, for example Buckley *et al.* [12]). Smaller pores that are water-filled and the corners of the pore space will remain water-wet. We will call such systems mixed-wet.

In this chapter we extend the work of Sahni *et al.*[58] and DiCarlo *et al.*[17] to mixed-wet media. The description of the experiments follows DiCarlo *et al.*[17], and for the sake of completeness, we present all our results in water-wet, oil-wet, fractionally-wet, and mixed-wet media. We characterize the wettability by measuring two-phase (water/oil) capillary pressure curves. We measure the gas relative permeability using an analogue experiment in which we directly measure the gas saturation and pressure gradient. Thus we obtain all three permeabilities for three-phase gravity drainage, in water-wet, oil-wet, mixed-wet and fractionally-wet sandpacks. We explain the results in terms of the pore scale fluid arrangements.

2.2 Materials and Methods

We chose sandpacks as our porous media as they are easy to characterize and they are easily sectionable for destructive saturation measurements. We used clean industrial sand (no. 60, Corona Industrial Sand Co., Corona, CA) which was initially water-wet. The sand was sieved with a size 120 sieve to remove any fine particles. We made 15 kg of the sand oil-wet by soaking initially dry sand in a mixture of 20% crude oil (Thums Inc., Long Beach, CA) and 80% iso-octane for 24 hours [13]. This oil-wet sand was then rinsed with iso-octane and air-dried. The fractionally-wet sand was a 50-50 mixture of the oil and water-wet sands.

Mixed-wet sandpacks were created from water-wet packs, by first saturating the pack with a 0.01M NaBr brine (pH 4). We then displaced the brine with 5 pore volumes (PV) of the crude/iso-octane mixture, yielding a pack with a water saturation of $S_w \approx 0.2$. The column was then left to age for a week. After the aging the crude mixture was displaced with iso-octane until the effluent ran clear. Finally, the pack was flooded by n-octane, replacing the iso-octane, then flooded with the working water phase (either distilled water or 10% NaBr brine, see below) to replace the brine.

For our fluids, we chose n-hexane, n-octane, or n-decane for the oil phase, distilled water or 10% NaBr by weight brine for the water phase, and air for the gas phase. The density of the brine was measured volumetrically, and the density of the oils was taken from the CRC Handbook [15]. Viscosities were measured using a viscometer. Interfacial tensions were measured using the pendant drop technique [1]. Table 2.1 shows the fluid properties. All experiments were performed at room temperature and pressure.

Table 2.1: Fluid densities [$\rho_w = 1069$ kg/m^3], viscosities [$\mu_w = 1.23$ cP], and interfacial tensions [$\gamma_{gw} = 72.0$ mN/m].

Oil	ρ_o (kg/m^3)	μ_o (cP)	γ_{ow} (mN/m)	γ_{go} (mN/m)
n-hexane	659	0.30	50.5	18.0
n-octane	703	0.51	51.2	21.1
n-decane	730	0.84	51.4	23.7

In all of the experiments, the sandpacks were set to connate water saturation (S_{wc}) or residual oil saturation (S_{or}) by the following procedure. For uniform-wet packs (water-wet and oil-wet), the core was saturated with the most wetting fluid (water for water-wet, oil for oil-wet) and then displaced with 5 PV of the intermediate wetting fluid (oil or water). This produced an initial condition of S_{wc} for the water-wet pack and S_{or} for the oil-wet pack. Initial conditions of S_{or} for the water-wet pack and S_{wc} for the oil-wet pack were achieved by an additional 5 PV flooding of the most-wetting fluid. For the fractionally-wet pack there is no most-wetting fluid, so an initial condition of S_{or} was achieved by flooding a 100% oil-saturated pack with water, and S_{wc} was achieved by flooding a 100% water-saturated pack with oil. For the mixed-wet pack, since its last flood was by the water phase, it was already at S_{or}. An additional flood of oil was used to achieve S_{wc}. For each experiment, a new mixed-wet pack was created from water-wet sand except for the three-phase drainage from S_{wc}. In this case, due to a need to recalibrate the CT scanner, the core that was used for the drainage from S_{or} was dried out completely by flowing dry air through the column for 4 weeks. The column was then filled with oil. This was followed by 2 PV of isopropanol to miscibly displace the oil, and then 5 PV of brine. Finally, 5 PV of octane was injected to produce the initial condition of S_{wc}. All displacements were performed in a gravitational stable configuration.

2.2.1 Capillary Pressure Curves

To characterize the wettability changes, we measured two-phase water/oil capillary pressure curves using a gravitational equilibrium technique. Distilled water was used for the water phase, and n-octane for the oil phase. The desired medium was packed through a continuous pour into a 72 cm column (2.54 cm inner diameter) and sealed at both ends with rubber stoppers. The column consisted of 24 separate 3 cm long polycarbonate sections held together with teflon shrink tubing, which made it easier for accurate sectioning of the column for saturation measurements. For water injection (which we will call imbibition even for nonwater-wet media), the medium was initially set to S_{wc} (see above). The imbibition began by connecting the bottom of the column to a large tank of water (whose height and thus the water head did not change during the imbibition) and the top to a smaller volumetric tank of oil (whose height changed slightly during the imbibition). Using calculations described below, the oil and water heads were chosen such that the water would imbibe throughout the porous medium. An identical technique was used for drainage curves (oil invasion), except that the column was initially set to S_{or}, and the heads set for drainage. Thus the curves obtained are for secondary imbibition and secondary drainage.

Once the tanks were attached, the columns were left for roughly 1 week to reach gravitational equilibrium. Then the columns were sectioned, their contents were dropped into a flask containing 25 ml of isopropanol, which created a single-phase mixture suitable for analysis, and the oil and

water saturations were measured using a gas chromatograph (GC). From this we obtained the saturation profile versus vertical position.

Assuming that the column is at capillary equilibrium, the profile can be described in terms of the capillary pressure. We define z positive downward and $z = 0$ at the top of the column. Let z_o be the final height of the oil level in the oil tank, and z_w the final height of the water in the water tank. Since the column is at equilibrium, the pressure of each phase i as a function of z is given by

$$P_i = \rho_i g(z - z_i), \tag{2.1}$$

where ρ is the density, and g the gravitational constant. Thus the capillary pressure is

$$P_c = P_o - P_w = (\rho_o - \rho_w)gz - (\rho_o g z_o - \rho_w g z_w). \tag{2.2}$$

The water and oil heads were chosen such that the capillary fringe would be roughly in the center of the column after imbibition. If this did not occur, the experiment was repeated with different heads.

2.2.2 Oil and Water Relative Permeabilities

Before and during gravity drainage, we used a dual energy CT scanner to obtain in-situ measurements of the water and oil saturations[58]. To achieve good CT contrast, the 10% NaBr brine was used for the water phase, and either n-hexane, n-octane, or n-decane was used for the oil phase. The core holders were standard Hassler-type with an overburden fluid (water at 50 psi) and a rubber sleeve. The sand was packed into the rubber sleeve of diameter 7.6 cm and length 67 cm (87 cm sleeves were used for water-wet sand). The core was mounted on a vertical positioning system in a Picker 1200X CT machine, which scanned in the horizontal plane. Scans of width 5 mm were taken every 2 cm along the core and at energy levels of 80 kV and 140 kV.

The experiment was calibrated by scanning the core when it was dry, when it was saturated with brine, and when it was saturated with oil. Using this calibration and a standard linear interpolation of CT number (i.e. attenuation coefficient), the water, oil, and air saturations could be obtained during a three-phase experiment. The saturations were observed to be uniform over each slice, except within 2 cm of the capillary fringe where the scans showed regions of high and low saturations. In either case, the saturations were averaged over each slice to give the average water, oil, and air saturation every 2 cm.

We can estimate the accuracy of the saturation by measuring the standard deviation on a pixel basis, and then assuming the standard deviation of the average saturation is the standard deviation of the mean. This gives a typical accuracy of $\Delta S_i \approx 0.0002$. This is likely to be too small due to nonlinear systematic variations such as beam hardening. In practice, when the core is at its initial condition with water and oil, but no gas, we measure a typical gas saturation value of $S_g \approx \pm 0.01$. Thus we estimate our accuracy for each phase to be $\Delta S_i \approx 0.01$.

Before drainage each core was set to connate water S_{wc} or residual oil S_{or} saturation as described before. Once the desired initial condition was reached, gas (air) was allowed to enter the top of the system, while water and oil drained out of the bottom under gravity. Before entering the column the air passed through a bubbler filled with water and a bubbler filled with oil to saturate the air with water and oil vapor. The bubblers also provided a one-way pathway for the air such that no oil and water vapor could leave the column through the top port. The height of oil and water that the entering air bubbled through was less than 1 cm, so the pressure boundary conditions were $P_g = 0$ Pa at the outlet and $P_g \approx -100$ Pa at the inlet.

The pack was periodically scanned over a period of several weeks to record the saturation distribution versus time. Figure 2.1 shows the saturation profile of octane and water at various times for a water-wet column that was initially at S_{wc}.

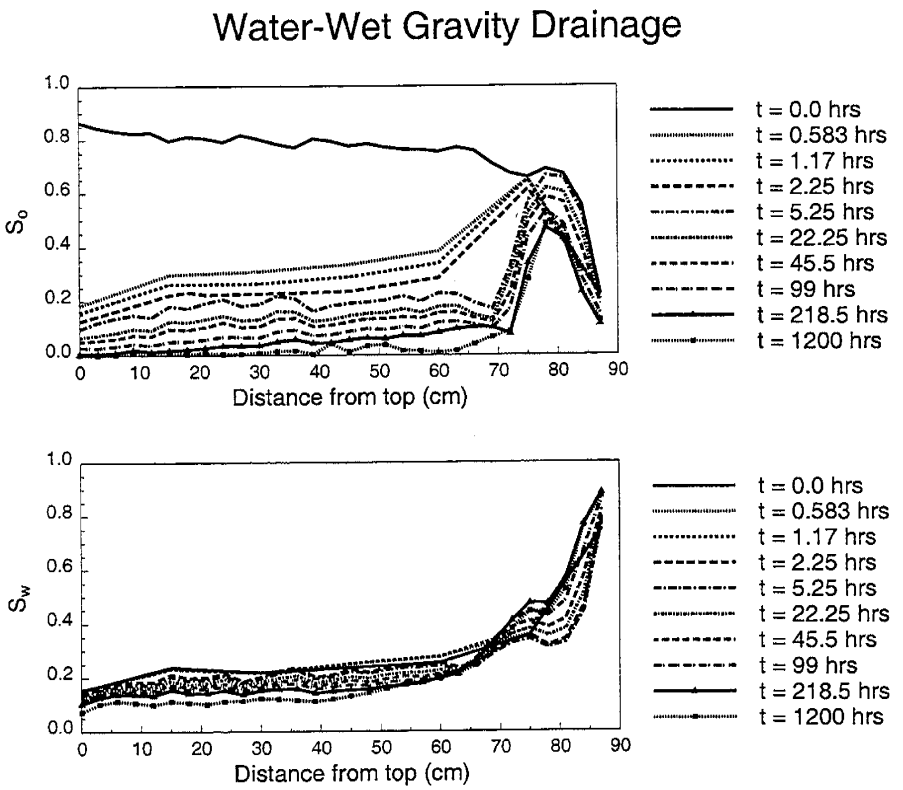

Figure 2.1: Oil (octane) and water saturation profiles versus time during gravity drainage. The sand was water-wet and the initial condition was connate water saturation S_{wc}. Oil and water permeabilities can be calculated directly from the measured distributions.

We can compute the oil and water relative permeabilities at each measured position along the column and for each time from the known time evolution of the saturation profile $S_i(z,t)$. We begin with Darcy's law for each phase in a 1-dimensional vertical displacement,

$$u_i = -\frac{kk_{ri}}{\mu_i}\left(\frac{\partial P_i}{\partial z} - \rho_i g\right), \tag{2.3}$$

where u is the flux, k is the permeability (20 Darcy for our sand), k_r is the relative permeability, μ is the viscosity, and z is the vertical distance taken to be positive downward. We calculate the flux past position z for time interval t_1, t_2 by integrating the change in the saturation of each phase between scans at times t_1 and t_2,

$$u_i(z,t_1,t_2) = \frac{\phi}{(t_2-t_1)}\int_0^z S_i(z',t_1) - S_i(z',t_2)dz', \tag{2.4}$$

where ϕ is the porosity.

The only remaining unknown is the pressure gradient $(\partial P_i/\partial z)$. This can be found directly using tensiometers, or indirectly by calculating the pressures from the saturations and a known capillary pressure curve[58]. In practice the indirect method has difficulties for column positions near and below the capillary fringe as the quantity $\partial S_i/\partial z$ is large, and the capillary pressure gradient is very close to the gravitational gradient. Thus any small errors in the saturation measurement correspond to large errors in the measured permeability.

Fortunately, we notice that near the top of the column the saturation is roughly constant with position $(\partial S_i/\partial z \approx 0)$. Thus we assume that $\partial P_i/\partial z << \rho_i g$ and ignore the capillary pressure gradient for positions over a region were the saturation data satisfies the above condition (between 20 and 50 cm in Fig. 2.1). For the shorter oil-wet, mixed-wet, and fractionally-wet cores, the above condition was satisfied only between 10 and 30 cm from the top of the chamber. In essence, the CT scanner allows us to avoid capillary end effects in the determination of relative permeability, as we can choose a section over which the capillary pressure gradients are negligible compared to gravity.

For this region the relative permeability as a function of z and time interval t_1, t_2 can be found by combining Eqs. 2.3 and 2.4 and dropping the pressure gradient,

$$k_{ri}(z,t_1,t_2) = \frac{\mu_i\phi}{k\rho_i g(t_2-t_1)}\int_0^z S_i(z',t_1) - S_i(z',t_2)dz'. \tag{2.5}$$

Calculating the saturation as a function of z and time interval t_1, t_2 as the average of the t_1 and t_2 saturations,

$$S_i(z,t_1,t_2) = (S_i(z,t_1) + S_i(z,t_2))/2, \tag{2.6}$$

we can then plot k_{ri} as a function of S_i.

The accuracy of the technique is a function of the accuracy of the saturations, fluxes, and pressure gradients. The saturation accuracy is estimated previously to be ± 0.01. The flux accuracy is also likely to be good, as we know the time accurately and by integrating the saturations, the deviations are minimized further. The largest uncertainty is in the estimate of the pressure gradient. Simple two-phase simulations suggest that the assumption that the pressure gradient is small compared to the gravitational gradient is very good for short time scales (< 2 weeks), but can be in error by up to 30% at long time scales (> 6 weeks).

2.2.3 Gas Relative Permeability

We have developed a procedure to measure the gas relative permeability in the sand packs. Distilled water was used for the water phase, and n-octane for the oil phase. The sand is packed

Table 2.2: Amott indices, and residual saturations from the two-phase (water/oil) pressure - saturation curves.

Wettability	I_w	I_o	S_{or}	S_{wc}
water-wet	1	0	0.20	0.15
oil-wet	0	0.05	0.05	0.20
mixed-wet	0.10	0	0.10	0.10
fractionally-wet	1.0	0	0.25	0.20

through a continuous pour into a 60 cm column made out of 20 separate 3 cm long sections similar to that used in the capillary pressure curve measurements. Additionally, nine of the plastic sections in the column contain a small port through which the pressure of the gas phase can be measured. Thus we can measure eight separate pressure drops along the column during gas flow.

We first measure the single phase gas permeability by flowing known rates of CO_2 (between 5 and 10 ml/sec) through the column and measuring the pressure drops across each section using a water manometer. For two-phase measurements, the column is then filled with degassed water from below and the water is circulated until all of the original CO_2 is displaced or dissolved. The column is then allowed to drain under gravity for about 1 hour, after which air is injected at a rate between 0.1 and 1 ml/sec at the top of the column, displacing additional water out the bottom. This injection is continued for several hours until the pressures have stabilized and the gas and water phases are in equilibrium. Due to capillary effects, the distribution of water varies along the sand pack, with a high water saturation (and low gas saturation) near the outlet and a low water saturation (and high gas saturation) near the inlet. The pressure drop is measured between each section, which in turn gives the gas relative permeability. The column is sectioned and the water and gas saturations are obtained gravimetrically. Low injection rates retained more water in the column and were used for low gas saturation measurements. There was no measurable effect on the gas relative permeabilities from the different gas injection rates.

For three-phase measurements a nearly identical procedure is used. The only differences are 1) the column is first filled to S_{wc} and 2) the oil, water, and gas saturations are measured using the GC rather than gravimetrically. We did not measure the gas relative permeability for the mixed-wet sands.

2.3 Results

2.3.1 Capillary Pressure Curves

The first column of Figure 2.2 shows the drainage and imbibition curves for the sandpacks of different wettabilities. The curves are for two-phase water/oil displacements. From these curves, the calculated Amott wettability indices[2] and two-phase residual saturations are shown in Table 2.2.

For the oil-wet medium, the procedure we used to make the oil-wet pack should produce a uniform wettability on all the pore surfaces. The large hysteresis when compared to the water-wet case, the lack of spontaneous water imbibition, and the capillary pressures of the transition zones suggest that the water/oil contact angle is greater than 90°. Also, S_{or} is smaller than the water-wet case, implying that the oil remains connected at low saturations.

Measurements of contact angles in glass capillary tubes that had been treated by crude oil in the same manner as our sand found an oil/water contact angle of 152°.[25] Contact angles this

Table 2.3: Drainage experiments from which three-phase oil and water relative permeabilities were obtained. The figure column shows where the data is displayed. The initial condition (I.C.) before drainage was either waterflood residual (S_{or}) or connate water (S_{wc}).

Expt.	Figure(s)	Oil	Porous Medium	I.C.
1	2.1, 2.2, 2.3, 2.9	octane	water-wet sand	S_{wc}
2	2.2, 2.9	octane	water-wet sand	S_{or}
4	2.3	hexane	water-wet sand	S_{wc}
5	2.3,2.9	decane	water-wet sand	S_{wc}
6	2.3	octane	water-wet sandstone	S_{or}
7	2.2,2.9	octane	oil-wet sand	S_{or}
8	2.2	octane	oil-wet sand	S_{wc}
9	2.2	octane	fractionally-wet sand	S_{or}
10	2.2	octane	fractionally-wet sand	S_{wc}
11	2.2,2.9	octane	mixed-wet sand	S_{or}
12	2.2,2.9	octane	mixed-wet sand	S_{wc}

large in a porous medium should result in a significant degree of spontaneous oil imbibition.[20] However, the low oil Amott index of 0.05 shows that this is not the case. Overall, the oil-wet sandpack is only weakly oil-wet or almost neutrally-wet. While a direct measurement of oil/water contact angle on the sand grains is not possible, it is likely to be only slightly greater than 90°.

For the mixed-wet medium, we will assume that our procedure induced wettability changes as described by Salathiel [59] and Kovscek *et al.*[41]. When the crude oil contacts the solid, it can deposit surface active agents rendering these surfaces oil-wet. The larger pore spaces will tend to be oil-wet, as the smaller pores and throats remain water-filled. The corners and crevices of the large pore spaces will also remain water-filled and thus water-wet. Thus the oil-wet and water-wet portions will be discriminated by pore size.

The irreducible water saturation, S_{wc} is slightly lower than in the water-wet sand, while the residual oil saturation, S_{or}, is between the water-wet and oil-wet cases. Also, the capillary pressures in the transition zone lie between the water-wet and oil-wet sands. The mixed-wet pack does not imbibe oil, while it imbibes some water. Overall its Amott indices imply a weakly water-wet or neutrally-wet system. It is possible that in our experiments the crude oil only renders the surfaces it contacts weakly oil-wet.

For the fractionally-wet media, since each sand grain is either water or oil-wet, each side of a pore will be either water or oil-wet. There will be no pore size discrimination for oil-wet and water-wet portions. Also the oil-wet and water-wet surfaces will be connected only randomly, producing pockets of oil-wet and water-wet regions. This description agrees with the observed large residual water S_{wc} and large residual oil S_{or}, as each fluid can get trapped in their isolated pockets [73]. But the observed capillary pressures in the transition zones are much closer to the water-wet sands, which is unexpected.

2.3.2 Three-Phase Relative Permeability

Table 2.3 lists all the three-phase drainage experiments and the figures which display the data. The experiments studied how the three-phase relative permeabilities varied as a function of the oil phase, the porous medium, and the initial condition of the pack. The second and third

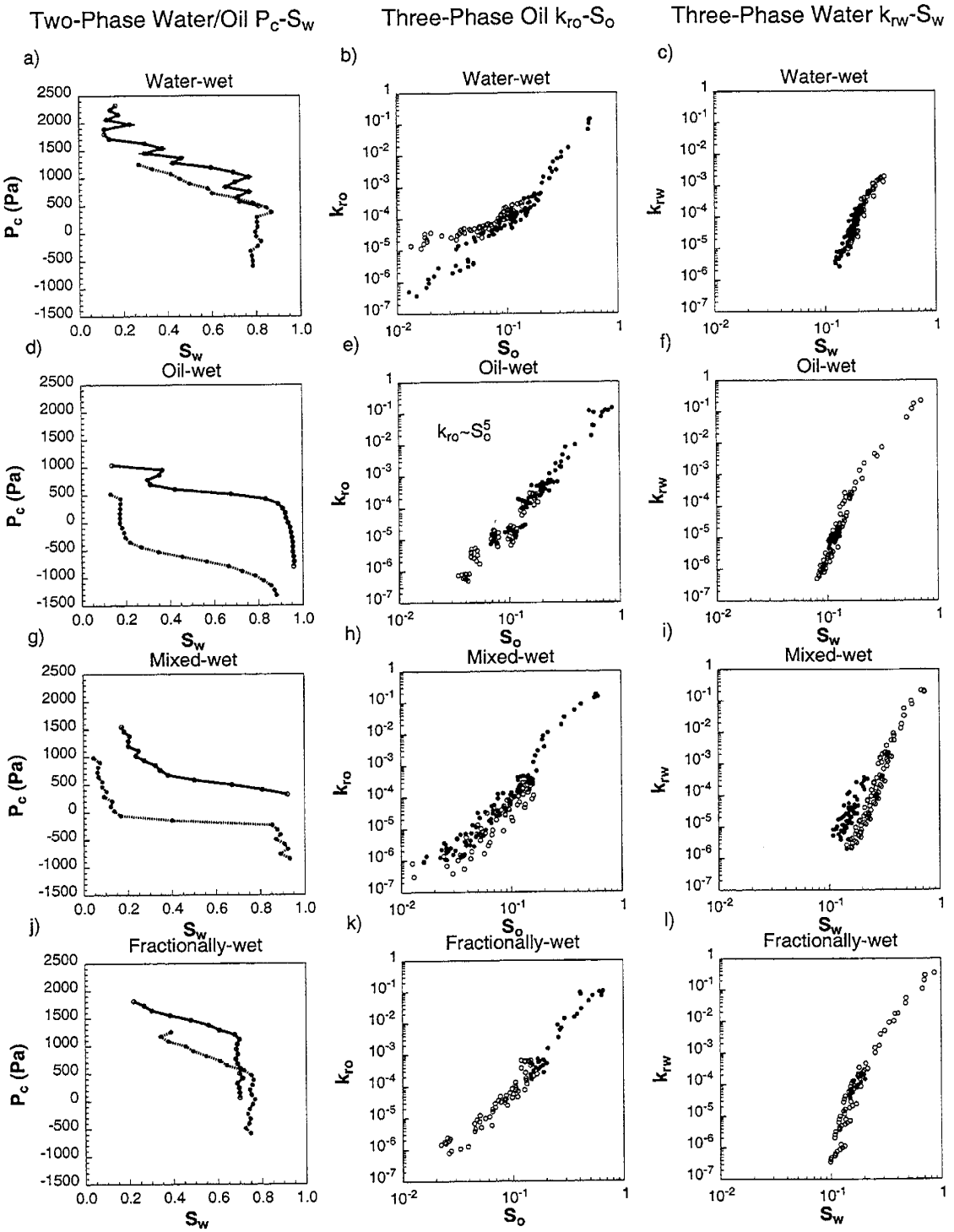

Figure 2.2: Measured two-phase (water/oil) capillary pressure curves and three-phase oil and water relative permeabilities with n-octane as the oil for water-wet, oil-wet, mixed-wet, and fractionally-wet sand. Open symbols are drainages which started from residual oil saturation (S_{or}), and closed symbols are drainages which started from connate water saturation (S_{wc}).

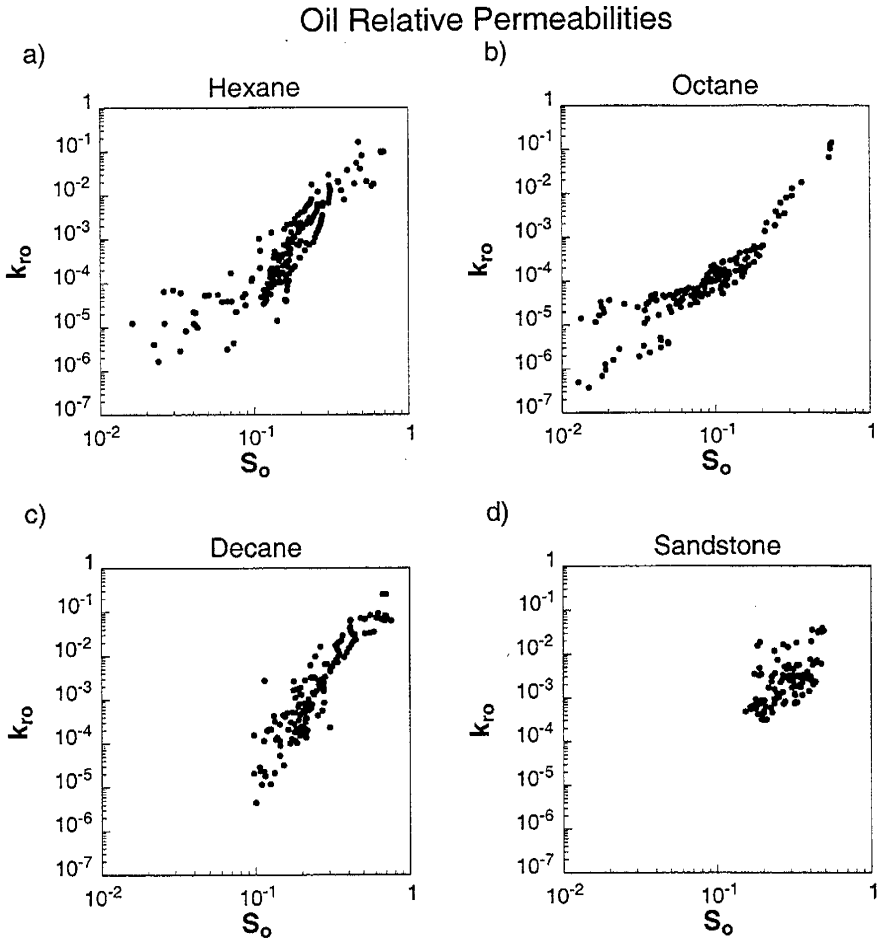

Figure 2.3: Measured oil relative permeabilities with hexane, octane, and decane as the oil in water-wet sand and with octane in water-wet sandstone[58] during three-phase gravity drainage.

columns of Figure 2.2 show the measured relative permeabilities for oil and water for the water-wet, oil-wet, mixed-wet, and fractionally-wet sandpacks with octane as the oil.

The open symbols are from the initial condition of S_{or} while the closed symbols are from drainages that started from initial condition S_{wc}. Note that we can measure saturations as low as $S = 0.01$, with relative permeabilities spanning over six orders of magnitude. The observed scatter in the data is likely a result of the combination of uncertainty in the pressure gradient and the natural variations in the porous medium. For ease in viewing the data, each relative permeability (in this figure and the following figures) is shown as a function of only the particular phase's saturation. The relative permeability can also depend on how the rest of the pore space is partitioned between the other two fluids. This can appear as additional scatter in the above plots, and is discussed later.

Figure 2.3 shows the measured oil relative permeability for hexane, octane, and decane in water-wet sand, and for octane in a water-wet consolidated sandstone. Figure 2.4 shows the measured water relative permeability for two-phase (gas/water) and three-phase drainages in water-wet sand. Figure 2.5 shows the measured gas relative permeabilities for a) the two-phase gas/water system for different wettabilities and the two-phase gas/oil system for oil-wet media, and for b) the three-phase system for water-wet and oil-wet media. Notice that for the gas permeability the plots are on linear axes.

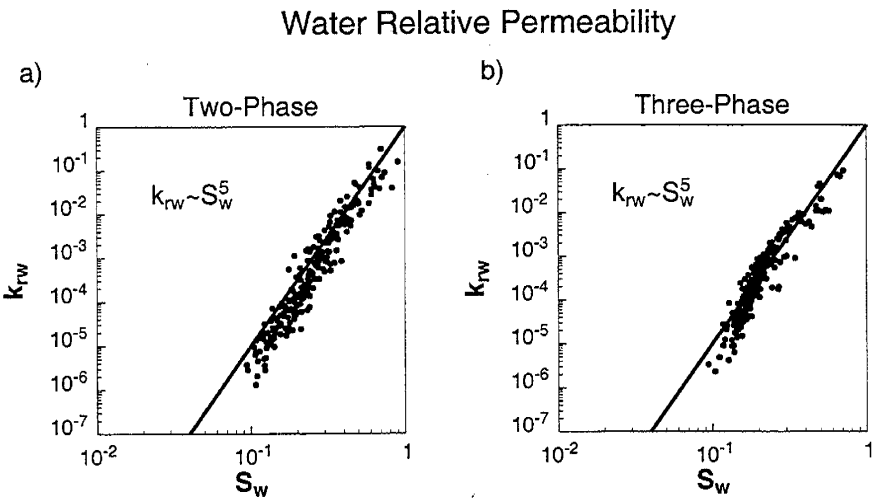

Figure 2.4: Measured water relative permeabilities for a) the two-phase (gas/water) system and for b) the three-phase (gas/oil/water) system from gravity drainages in water-wet sand.

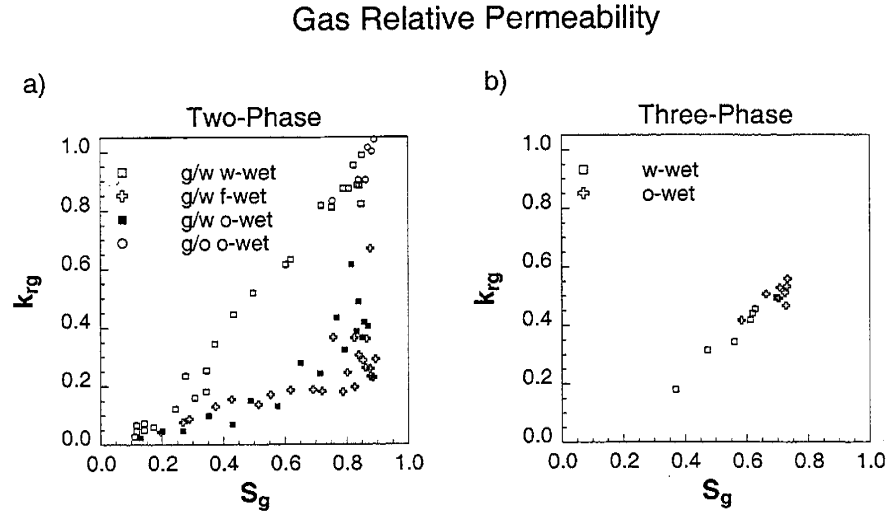

Figure 2.5: Measured gas relative permeabilities for a) the two-phase gas/water system for media of varying wettability and the two-phase gas/oil system for oil-wet media, and for b) the three-phase gas/oil/water system for water-wet and oil-wet media. The gas relative permeability in oil-wet sand is roughly a factor of two smaller than that for identical water-wet sand for two-phase gas/water systems.

The following features are observed in the measured relative permeabilities:

1. Except for the water in the mixed-wet sand, the oil and water relative permeabilities during three-phase drainage are independent of initial condition to within experimental scatter (Fig. 2.2).

2. The three-phase relative permeabilities of the most wetting fluid (water in water-wet media, oil in oil-wet media) and the two-phase water relative permeability in water-wet media are similar. All can be well described by a simple power law $k_r \sim S^\alpha$, where $\alpha \approx 5$ (Figs. 2.4a, 2.4b, 2.2c and 2.2e). For the most wetting fluid the permeability is the same for two and three phase displacements. However, for the most wetting phase, a lower saturation is reached in the oil-wet medium (Fig. 2.2e) than in the water-wet medium (Fig. 2.2c).

3. At low saturations, $S < S_{or}$ (S_{wc}), the relative permeabilities of oil in water-wet media (Fig. 2.2b) and water in oil-wet media (Fig. 2.2f) are very different. For hexane and octane, the oil relative permeability remains finite at low saturations with a power law of $k_r \sim S^\alpha$, where $\alpha \approx 2$ (Figs. 2.2b, 2.3a and 2.3b). The water relative permeability drops off quickly, tending to zero at water saturations of $S_w \approx 0.1$ (Fig. 2.2f).

4. For the mixed-wet sandpack, the oil relative permeability is similar to the water-wet sandpack at low saturations (Figs. 2.2h and 2.2b). It has the largest k_{ro} of any wettability at moderate saturations ($S_o = 0.2 - 0.4$). The water relative permeability is the smallest of all the wettabilities, and it depended on the initial condition (Fig. 2.2i).

5. When water is the main liquid phase, the gas relative permeability for the oil-wet and fractionally-wet medium is roughly a factor of two smaller than that for an identical water-wet medium (Fig. 2.5a). When oil is the main liquid phase, the gas relative permeability is independent of the wettability (Fig. 2.5a).

6. For the fractionally-wet sandpack, the oil, water and gas relative permeabilities are between the oil, water and gas relative permeabilities in the water-wet and oil-wet sands (Figs. 2.2k, 2.2l and 2.5a).

Although exact functional forms of relative permeabilities can be dependent on the specific porous medium, we believe that many of the above features are universal for three-phase displacements. We discuss this by considering the effects of pore scale configuration on the relative permeabilities.

2.4 Pore Scale Explanation

1. The oil and water relative permeabilities are independent of initial condition during three-phase drainage (except for the mixed-wet case).

In water-wet media, the water occupies the smallest pores, regardless of the saturations of oil and gas. Thus in a drainage-type experiment with the water saturation decreasing, the relative permeability of water should be insensitive to initial condition. This behavior has been seen by other researchers [5, 23]. Oil, however, occupies the intermediate sized pores, and its pore occupancy does depend on the saturations of both water and gas: in a gas/oil displacement, oil occupies the smaller pores, whereas for an oil/water displacement, oil occupies the larger pores. Reviews of the literature have shown that the oil relative permeability is sensitive to initial condition [5, 23]. We do not see this for $S_o > 0.05$, and the oil relative permeability appears to be a function only of its own

saturation. There is a significant effect of initial condition on k_{ro} for $S_o < 0.05$ in Fig. 2.2b. However, it is difficult to make a definitive comment because of considerable experimental inaccuracies in this low saturation region. The lack of sensitivity to initial condition at moderate oil saturations, could be due to the narrow pore size distribution of the sandpacks, and is consistent with other results in uniform media [27, 5]. Similarly, for water in oil-wet media, we see no sensitivity to initial condition, although the water is no longer the wetting phase.

In the mixed-wet media, we do see a measurable dependence on the initial condition for the water relative permeability. The water relative permeability is noticeably larger when starting from S_{wc} then from S_{or}. The water saturation does not drop below $S_w = 0.15$ when starting from S_{or}, while it reaches less than $S_w = 0.10$ when starting from S_{wc}. When the initial condition is S_{wc}, water is only present in the smaller pores and corners. In this sense it resembles a water-wet medium, and as can be seen in Figs. 2.2i and 2.2c, the water relative permeability is similar to the water-wet case. When drainage (gas invasion) starts from S_{or}, water is also present in the centers of larger pores. If these pores are oil-wet, then water can be trapped in them during drainage. In the oil-wet system, a residual water saturation of around $S_w = 0.10$ is observed (Fig. 2.2f). In the mixed-wet pack, the final water saturation is approximately $S_w = 0.15$, or the sum of the oil-wet residual and the remaining water saturation in the corners.

2. The relative permeability of the most wetting phase in water-wet and oil-wet media are similar.

The most wetting phase occupies the smallest pores, and corners, grooves, and crevices in the wider pores. If we compare strongly and uniformly water-wet and oil-wet media, we would expect the configuration of the most wetting fluid to be similar for both systems at the same saturation. The exact functional form of the relative permeability depends on the porous medium and is not universal. The only general feature is that k_r should asymptotically approach zero saturation at a sufficiently high capillary pressure, indicating that the wetting phase remains connected, albeit poorly, through wetting layers in crevices of the medium down to very low saturation.

In the experiments, the lowest wetting phase saturation observed depends on the largest capillary pressure reached – it takes an infinite capillary pressure to reach zero saturation. It is possible to show [17] that at the top of the column smaller interfacial radii of curvature are achieved for oil in the oil-wet system than for water in the water-wet system. This explains why in our experiments the lowest water saturation reached in the water-wet pack ($S_w \approx 0.1$) is higher than that reached in the oil-wet pack ($S_o \approx 0.04$) – see Fig. 2.2.

3. The relative permeability of the intermediate wetting phase (oil in water-wet media, water in oil-wet media) at low saturation are very different.

At low saturation phases may remain connected through wetting layers in crevices in the pore space. It is this connectivity which controls k_r at low saturation. The pore scale configuration and connectivity of oil and water is very different for water-wet and oil-wet media. Consider first flat water-wet and oil-wet surfaces as shown in Figure 2.6.

The most wetting fluid coats the surface. The contact angle between oil or water and gas, which will control the position of the phase in the pore space, is given by the balance of interfacial tensions, assuming that the solid is coated with a thick wetting film.

For oil in water-wet media, (Fig. 2.6a)

$$\cos\,\theta_{go} = \frac{\gamma_{gw} - \gamma_{ow}}{\gamma_{go}} = 1 + \frac{C_{so}}{\gamma_{go}}, \tag{2.7}$$

where

$$C_{so} = \gamma_{gw} - \gamma_{ow} - \gamma_{go} \tag{2.8}$$

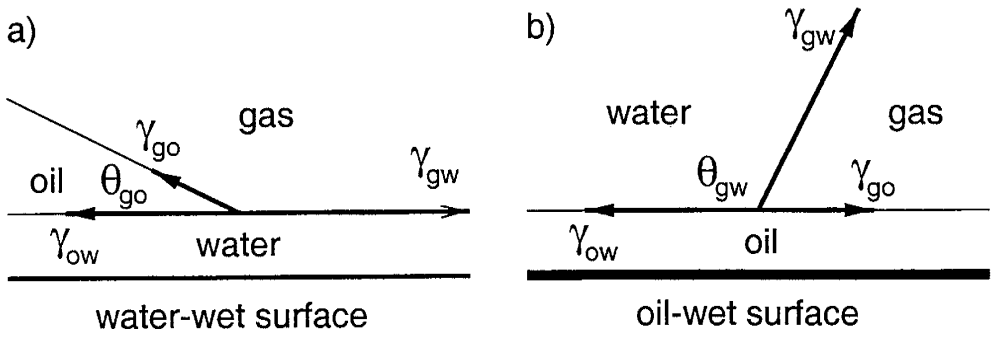

Figure 2.6: Configuration of fluids on : a) a flat water-wet surface, b) a flat oil-wet surface (shown bold).

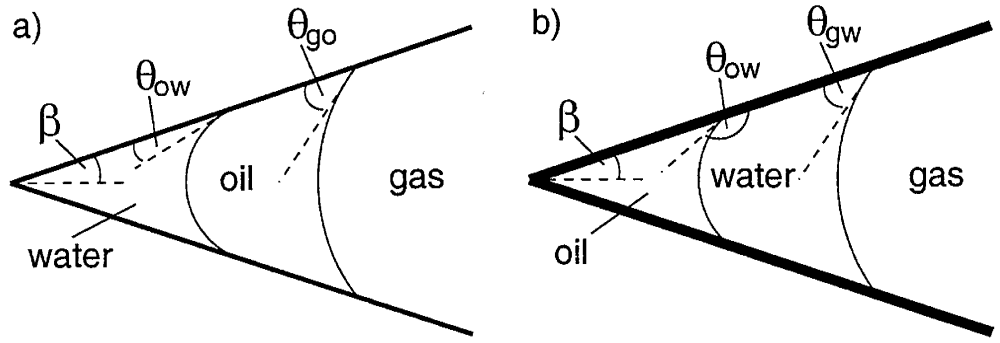

Figure 2.7: Possible configuration of fluids in a pore space corner of half-angle β: a) water-wet surfaces, b) oil-wet surfaces (shown bold). Note that configuration b) is not allowed as $\theta_{gw} > 90°$.

is the spreading coefficient for oil. Using our data in Table 2.1 we find C_{so} = 3.5, -0.3, and -3.1 mN/m for hexane, octane, and decane, respectively. For octane (the most used fluid) this results in $\theta_{go} \approx 10°$.

Now consider the three fluids in a corner of the pore space as shown in Fig. 2.7a. If $\theta_{ow} + \beta < 90°$ and $\theta_{go} + \beta < 90°$, where β is the half-angle of the corner, then a layer of oil may be present [50, 24]. These layers are on the order of micrometers thick and have been observed in micromodel experiments [48, 61, 38]. Drainage through oil layers is the mechanism by which very low oil saturations are reached during gas displacement in water-wet media [21, 37, 72]. Final oil saturations as low as $S_o = 0.001$ have been reached [72]. For a system with $\theta_{ow} = \theta_{go} = 0$, the oil layers can drain to infinitesimal thickness at a *finite* gas/oil capillary pressure, meaning that in theory, $S_o = 0$ can be achieved through gravity drainage[11, 72]. In our experiments the lowest saturation obtained is $S_o \approx 0.01$ after 7 weeks of drainage.

Displacement of oil below the waterflood residual oil saturation, S_{or}, requires layer drainage. In our experiments, and others on bead packs, sandpacks and consolidated sandstones a layer drainage regime consistent with $k_{ro} \sim S_o^2$ has been observed for $S_o < S_{or}$ (see Figs. 2.3a, 2.3b, and 2.9a) [58, 46, 27]. This is readily explained by examining the flow in a single angular pore (see Fig. 2.7a). S_o is proportional to the area of the oil in the layer. The oil conductance for Poiseuille type flow is approximately proportional to the area squared, leading to $k_{ro} \sim S_o^2$ [24, 74]. This may seem a simple argument, but it is confirmed by more detailed analysis of layer flow that has been verified against numerical solutions of the Navier Stokes equation and experiments in square[74]

and triangular[25] capillary tubes.

We observe layer drainage for a spreading system – loosely defined as one with $C_{so} \approx 0$, or $\theta_{go} \approx 0$. However, the situation is different for oils with a large and negative spreading coefficient. For decane in water-wet media, our measurements of interfacial tension result in $\theta_{go} \approx 30°$. Decane layers have been seen in micromodels [38]. However, decane layers cannot form in oblique wedges ($\beta > 60°$), and are present for a more restricted range of capillary pressures than for octane [24]. If oil layers are not present, oil can be trapped, leaving a residual saturation at the end of drainage. In our experiments we do not observe a layer drainage regime, as shown in Fig. 2.9b.

For water in strongly oil-wet media, (Fig. 2.6b)

$$\cos \theta_{gw} = \frac{\gamma_{go} - \gamma_{ow}}{\gamma_{gw}} = 1 + \frac{C_{sw}}{\gamma_{gw}}, \tag{2.9}$$

where

$$C_{sw} = \gamma_{go} - \gamma_{ow} - \gamma_{gw} \tag{2.10}$$

is the spreading coefficient for water. Using Table 2.1 we find $C_{sw} = -102.1$ mN/m and $\theta_{gw} \approx 115°$. Even if the surface is not strongly oil-wet, there is a constraint between the interfacial tensions and contact angles[74],

$$\gamma_{gw} \cos \theta_{gw} = \gamma_{ow} \cos \theta_{ow} + \gamma_{go} \cos \theta_{go} \tag{2.11}$$

Using the octane data, if $\theta_{ow} > 110°$ then $\theta_{gw} > 90°$. Thus water is less wetting than gas, unless we have a very weakly oil-wet system ($\theta_{ow} < 110°$).

Measurements on oil-treated glass surfaces have found $\theta_{gw} = 103°$, consistent with Eq. 2.9. In Fig. 2.7b, water layers can occur for $\theta_{gw} + \beta < 90°$, and gas layers can occur for $90° + \beta < \theta_{gw}$, neither of which are possible except for gas in exceptionally sharp crevices. The absence of a layer drainage regime is evident in Fig. 2.9c.

Note that k_{ro} for decane in a water-wet system is similar to k_{rw} in an oil-wet system. Both represent cases where the intermediate-wet fluid is nonspreading and there is no layer drainage regime.

We do not observe the same layer drainage regime for the most wetting phase – instead of $k_r \sim S^2$, we observe $k_r \sim S^5$. The most wetting phase occupies the small pores and all the narrow nooks and crannies, where it is held by strong capillary forces and where it may be poorly connected. In contrast, oil layers in spreading systems reside over the water, and by construction therefore, are well connected throughout the porous medium.

4. The mixed-wet sandpack has an oil relative permeability similar to the water-wet pack at low saturations, while it was the largest of any wettability at moderate saturations ($S_o = 0.2-0.4$). The water relative permeability is the smallest observed for any wettability.

Figure 2.8 shows schematic arrangements of oil, water and gas in water-wet, oil-wet, and mixed-wet pores. In both water-wet and mixed-wet media water fills the corners of the pore space, even if oil fills the pore center. During gas injection, gas is nonwetting to oil, and thus in both cases, layers of oil between water in the corners and gas in the pore centers may be present. As a consequence, k_{ro} at low S_o is similar for mixed-wet and water-wet media, with a characteristic layer drainage regime. This implies a possible universal form for k_{ro} at low S_o in mixed-wet reservoir settings, since the behavior is independent of the oil/water contact angle. Notice that the layers can form in a mixed-wet system, even if water is in the center of the pores. This agrees with the observations that k_{ro} at low saturations is independent of the initial condition even when more water is trapped in the pores when starting from S_{or}. In contrast, in uniformly oil-wet media, oil is confined to the corners. The oil is held by strong capillary forces and has a lower k_{ro} as discussed before.

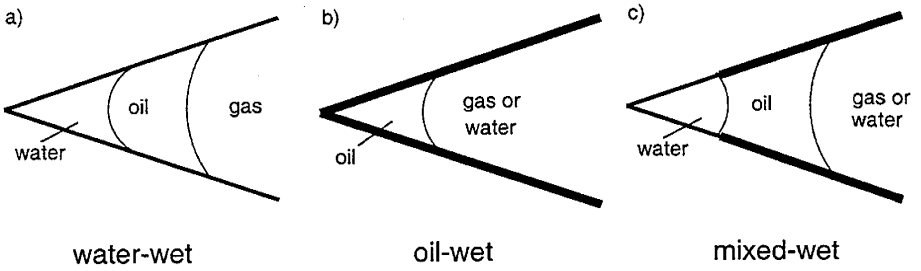

Figure 2.8: Pore-scale arrangements of fluid for water-wet, oil-wet, and mixed-wet corners. A thick line represents an oil-wet surface. Notice that oil layers sandwiched between water and gas are present for both the water-wet and mixed-wet media, leading to similar k_{ro} at low S_o. In oil-wet media, oil is confined to the crevices, leading to a lower k_{ro}.

Although it is difficult to see from the log-log plots of Fig. 2.2, between $S_o = 0.2 - 0.4$, k_{ro} was noticeably the largest in the mixed-wet packs. In this saturation range, the fluids will be contacting both oil-wet and water-wet surfaces. This being said, it seems most likely that k_{ro} would be *smaller* than the water-wet case, as the oil is most wetting on some of these surfaces. Thus, there is not a simple explanation of this phenomena, although it would be interesting what behavior is seen in a three-phase, mixed-wet network model.

The low water relative permeability is due to the large trapped water saturation during drainage. As explained in item 1, this is greatest in mixed-wet packs, as the water can get trapped in the big pores, and held by capillary forces in the small pores.

5. When water is the main liquid phase, The gas relative permeabiltiy is lower in an oil-wet medium than in a water-wet medium.

For the two-phase gas/water system in water-wet media, the water phase will occupy the smallest pores and crevices while the gas phase occupies the large pore spaces. In oil-wet media, the contact angle is such that neither the water phase nor the gas phase wets the pore surfaces and thus the water and gas phases compete for the largest pores. Thus at equivalent gas saturations, in the oil-wet system the gas is in smaller pathways leading to a lower permeability.

For the three-phase gas/oil/water system in water-wet media, the gas is nonwetting to both oil and water, and so k_{rg} is expected to be a function only of gas saturation. In oil-wet media, gas is nonwetting to oil, but is not strongly nonwetting to water. Thus it is expected that in this case k_{rg} depends on both the oil and water saturations. From Fig. 2.5b we see that the three-phase k_{rg} in the oil-wet system is between the two-phase gas/water k_{rg} and gas/oil k_{rg}. Most three-phase models [62, 23, 5] assume that gas is always the nonwetting phase and is a function of gas saturation only, which is not supported by these measurements.

We also see that the three-phase k_{rg} in the water-wet system is lower than the two-phase water-wet gas/water k_{rg} and oil-wet gas/oil k_{rg}. Since the gas is the most nonwetting phase in all of these experiments, we expect the gas relative permeabilities to be similar. Why this is not the case is currently unknown.

6. The fractionally-wet sand has behavior intermediate between oil-wet and water-wet sand.

This last observation seems intuitively obvious. However, there are three important points to make. First, the oil in a spreading system is always connected regardless of the oil-wet fraction,

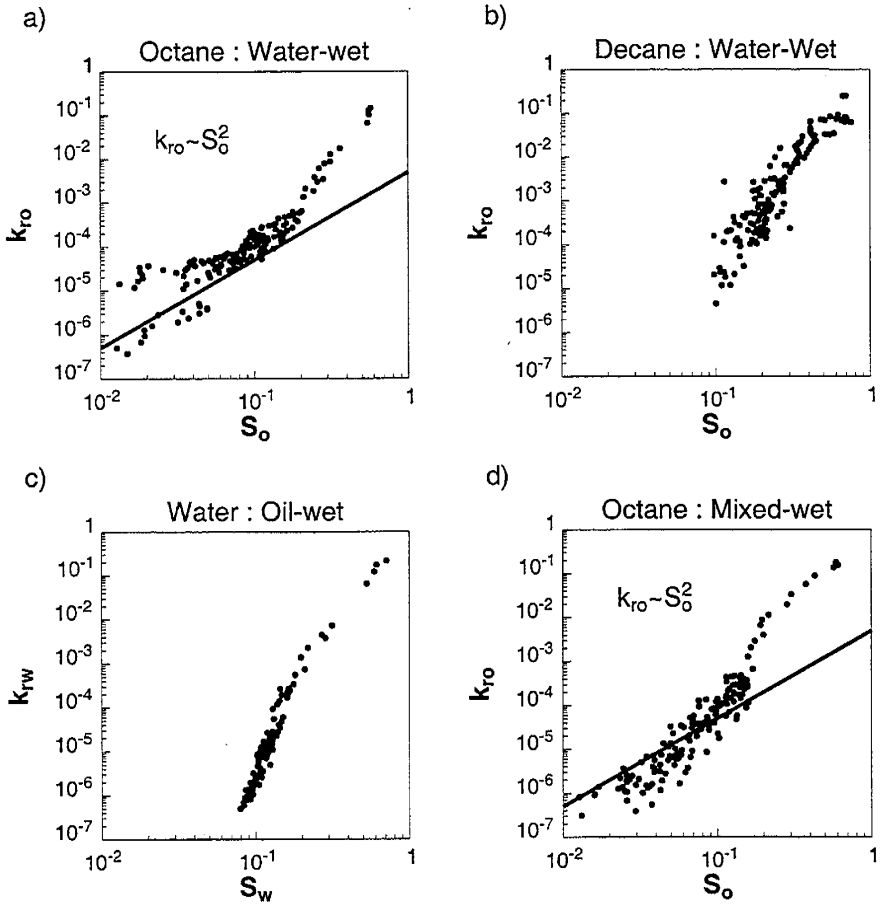

Figure 2.9: Comparison of relative permeabilities. (a) A spreading system ($\theta_{go} \approx 0$) : Octane in water-wet sand. (b) A nonspreading system : Decane in water-wet sand. (c) A nonwetting system : Water in oil-wet sand. (d) A mixed-wet system : Octane in mixed-wet sand. The solid lines in (a) and (d) show $k_{ro} \sim {S_o}^2$. The data, while consistent with this trend, only follows it approximately.

since it can reside in corners as the most wetting phase or in layers as the intermediate wetting phase. Consistent with this is the observation that k_{ro} asymptotically approaches zero residual oil saturation, for all wettabilities, as shown in Fig. 2.2. However, unless the small pores, corners and crevices are completely water-wet, an infinite capillary pressure is required to achieve this. Second, note that the trapped water saturation for the fractionally-wet sand is slightly *higher* than for the oil-wet sand. This is because in the fractionally-wet sand, the oil-wet regions are poorly connected in the pack leading to significant trapping of water. This percolation-type argument has been explored in more detail by Zhou *et al.* [73]. Third, the gas relative permeability for the fractionally-wet sand is very close to the oil-wet case. This shows that the gas mobility is significantly affected even if a fraction of the pores are oil-wet.

2.5 Discussion

Recently, there has been renewed interest in predicting capillary pressure curves and relative permeabilities from basic physics and the pore structure using pore network models (see, for instance [49]). One of our objectives in this study was to obtain a complete data set (capillary pressure curves and relative permeabilities) as a function of wettability. We hope that this data can provide a benchmark with which to test the various three-phase, mixed-wettability network models now being proposed. In this vein, the data can all be found by following links from our web site: http://ekofisk.stanford.edu/supric.html/ .

2.6 Conclusions

We used CT scanning and analogue experiments to measure oil, water and gas relative permeabilities during three-phase gravity drainage. Mixed-wet sandpacks were made by flooding a water-filled, water-wet pack with crude oil. The capillary pressure curve of the resultant medium indicated that it was neither strongly oil-wet nor water-wet. Drainage experiments were performed on oil-wet, water-wet, mixed-wet, and fractionally-wet sandpacks, Saturations as low as 0.01 were recorded and the relative permeabilities span six orders of magnitude. The main results are:

1. At low oil saturations ($S_o < S_{or}$) in water-wet media, spreading systems show a characteristic form of the oil relative permeability with approximately $k_{ro} \sim {S_o}^2$. This behavior is consistent with a theoretical interpretation of oil layer drainage at the pore scale. For a nonspreading decane system, the layer drainage regime was not observed.

2. Mixed-wet media also exhibit an approximate quadratic oil relative permeability at low oil saturations. The theoretical interpretation is that oil layers are present between water on the water-wet corners of the pore space, and gas occupies the oil-wet center.

3. In oil-wet media, the oil relative permeability is similar to the water relative permeability in water-wet systems. This behavior is consistent with the interpretation that the most-wetting phase occupies the same portion of the pore space in either wetting situation.

4. In oil-wet media, the water has a large and negative spreading coefficient, meaning that water layers do not form in the pore space. The water relative permeability k_{rw} for an oil-wet medium is similar to k_{ro} for a water-wet medium and a nonspreading oil.

5. In oil-wet media, the gas relative permeability is smaller than that for identical water-wet media. This behavior is consistent with the gas and water phases competing for the largest pores in oil-wet media, where gas is not necessarily the nonwetting phase.

2.7 Nomenclature

C_{so} = spreading coefficient for oil
C_{sw} = spreading coefficient for water
I_o = Amott oil index
I_w = Amott water index
g = gravitational constant
k_{ri} = relative permeability to phase i
P_i = pressure of phase i
S_i = saturation of phase i
S_{or} = waterflood residual oil saturation
S_{wc} = connate water saturation
u_i = flux of phase i

Greek Letters

α = power law exponent
β = half angle of pore corner
γ_{ow} = oil/water interfacial tension
γ_{go} = gas/oil interfacial tension
γ_{gw} = gas/water interfacial tension
μ_i = viscosity of fluid i
ϕ = porosity
ρ_i = density of fluid i
θ_{ow} = oil/water contact angle
θ_{go} = gas/oil contact angle
θ_{gw} = gas/water contact angle

Subscripts

i = phase
g = gas
o = oil
w = water (brine)

3. Fast Approximate Solutions for 1D Multicomponent Gas Injection Problems

Kristian Jessen, Yun Wang, Pavel Ermakov, Jichun Zhu, and Franklin M. Orr Jr.

This chapter presents a new approach for constructing approximate analytical solutions for one-dimensional (1D), multicomponent gas displacement problems. The solution to mass conservation equations governing 1D dispersion-free flow in which components partition between two equilibrium phases is controlled by the geometry of key tie lines. It has previously been proven that for systems with an arbitrary number of components, the key tie lines can be approximated quite accurately by a sequence of intersecting tie lines. As a result, analytical solutions can be constructed efficiently for problems with constant initial and injection compositions (Riemann problems). For fully self-sharpening systems, in which all key tie lines are connected by shocks, the analytical solutions obtained are rigorously accurate, while for systems where some key tie lines are connected by spreading waves, the analytical solutions are approximations, but accurate ones. Detailed comparison between analytical solutions with both coarse and fine grid compositional simulations indicates that even for systems with nontie-line rarefactions, approximate analytical solutions predict composition profiles far more accurately than coarse grid numerical simulations. Because of the generality of the new approach, approximate analytical solutions can be obtained for any system whose phase behavior can be modeled by an equation of state. The construction of approximate analytical solutions is shown to be orders of magnitude faster than the equivalent coarse grid compositional simulation. Hence, the new approach is valuable in areas where fast compositional solutions to Riemann problems are required.

3.1 Introduction

Miscible gas injection processes have become a widely used technique for enhanced oil recovery throughout of the world. The understanding of the multiphase, multicomponent flow taking place in any miscible displacement process is essential for successful design of gas injection projects. Due to complex reservoir geometry and reservoir fluid properties, numerical simulations of the flow processes are usually conducted to obtain such understanding. In principle, compositional simulation could be used to study such problems. In practice, however, conventional finite difference simulation is sufficiently slow that three-dimensional (3D) computations are feasible only for very coarse grids. Such simulations are not useful, however, because they are severely affected by numerical dispersion.

Recent progress in the application of streamline methods offers one way to overcome the limitations of 3D finite difference compositional simulations[66, 10, 8]. In the streamline approach, a one-dimensional (1D) solution is mapped onto streamlines that capture the effects of reservoir heterogeneity. Thiele *et al.*[65] described 2D and 3D streamline compositional simulations in which analytical and finite difference approaches were used to solve the 1D flow problem. Thiele *et al.*[65] used a numerical solution of the 1D problem to perform a compositional simulation for a heterogeneous 3D reservoir described with 518,000 grid blocks. At that time, analytical solutions for problems with an arbitrary number of components in the oil and injection gas were not available. In this chapter, we describe an algorithm to obtain analytical solutions for that problem. Use of the

[2]The material in this chapter was presented at the 1999 SPE Annual Technical Conference and Exhibition in Houston, TX, Oct 3-6, 1999, and is published as SPE paper 56608 in the conference proceedings.

analytical solutions in simulations like those of Thiele *et al.*[65] could lead to substantial additional speed-ups in streamline calculations.

A substantial body of mathematical theory now exists for construction of analytical solutions to the dispersion-free 1D multicomponent flow problem[45, 35, 36, 34, 19, 18]. This theory, based on the method of characteristics (MOC), illustrates that the behavior of the solution is controlled by the geometry of key tie lines in compositional space. Wang and Orr[70, 71] and subsequently Jessen *et al.*[33] have developed algorithms for approximating the key tie lines. In this chapter the key tie line approximation is combined with tools from the analytical theory of gas displacement to obtain fast, approximate solutions to the 1D, dispersion-free two phase flow problem.

3.2 Analytical Theory of 1D Miscible Displacements

The analytical theory of gas injection processes describes the complex interactions between two-phase flow and phase equilibrium for 1D dispersion-free miscible displacements. Analytical solutions obtained in this chapter are based on the following assumptions:

- The porous medium is homogeneous.
- Instant thermodynamic equilibrium exists everywhere.
- No gravity or capillary forces act on the fluid.
- Pressure and temperature are constant throughout the porous medium.
- Components do not change volume as they transfer between phases.

The assumption of no volume change is reasonable when pressures are high. For systems at lower pressures where solubility of light components in undisplaced oil is high but gas density is low, effects of volume change can be significant[18] and Dindoruk's formulation of the conservation equations should be used.

Based on these assumptions, the mass conservation equations are written in the form

$$\frac{\partial C_i}{\partial t} + \frac{\partial F_i}{\partial z} = 0, i = 1, \ldots, n_c, \tag{3.1}$$

where C_i is the overall volumetric fraction and F_i is the overall fractional flow of component i, t is dimensionless time, z is dimensionless distance and n_c is the number of components in the mixture. Considering two-phased flow, C_i and F_i are connected to the phase behavior by

$$C_i = c_{il}(1 - S) + c_{iv}S, \tag{3.2}$$

$$F_i = c_{il}(1 - f) + c_{iv}f. \tag{3.3}$$

S is the volumetric vapor fraction and f is the fractional flow of vapor, whereas c_{il} and c_{iv} are the volume fractions of component i in the liquid and vapor phases respectively. C_i and F_i are subject to the constraint

$$\sum_{i=1}^{n_c} C_i = \sum_{i=1}^{n_c} F_i = 1 \tag{3.4}$$

The fractional flow function used for this work is

$$f = \frac{S^2}{S^2 + M(1 - S - S_{or})^2}, \tag{3.5}$$

where M is the viscosity ratio (vapor/liquid), and S_{or} is the residual oil saturation. Finally the initial data are specified by

$$C(z,0) = \begin{cases} C_i^{inj} & z < 0 \\ C_i^{ini} & z > 0 \end{cases} \quad i = 1, \ldots, n_c. \tag{3.6}$$

The specification of constant initial and injection compositions to the mass conservation equations make the construction of analytical solutions to the flow problem possible. Eqs. 3.1-3.6 specify a Riemann problem.

Analytical solutions to Eqs. 3.1-3.6 are constructed by solving the eigenvalue problem associated with the mass conservation equations. In composition space, the corresponding problem is to identify the correct (unique) route that connects the initial oil composition and the injection gas composition. The composition route that describes the analytical solution geometrically is subject to the following requirements.

The composition route must have characteristic wave velocities in the two-phase region that increase monotonically from upstream to downstream locations. This condition is known as the velocity rule. If the velocity rule would be violated by a continuous variation (rarefaction), then a shock must be introduced to insure that the solution remains single-valued. The shock must satisfy the integral form of the mass conservation equations.

$$\Lambda = \frac{F_i^u - F_i^d}{C_i^u - C_i^d}, i = 1, \ldots, n_c, \tag{3.7}$$

where Λ is the shock velocity. Upstream and downstream parts of the shock are denoted u and d respectively. Eq. 3.7 is a Rankine-Hugoniot condition. Any shock present in a solution must satisfy an entropy condition, which requires the shock to be stable in the presence of a small amount of dispersion. In addition, solutions must satisfy a continuity condition with respect to initial and injection data. In other words, small perturbations to the initial or injection compositions must result in small changes in the solution.

For all the examples presented in this chapter the Soave-Redlich-Kwong equation of state was used for phase equilibrium calculation, whereas the Lohrenz-Bray-Clark[43] correlation was used for calculation of viscosity.

3.3 Self-Sharpening Systems

Fully self-sharpening systems are characterized by the feature that all key tie lines are connected by shocks. For such systems the key tie line intersection approach is rigorously accurate because the extension of a pair of key tie lines connected by a shock must intersect[35, 36, 34, 19, 18]. Two types of shocks occur. When the shock velocity matches the tie-line eigenvalue (df/dS) on one side of the shock, the shock is known as a tangent shock. When the shock velocity differs from the wave velocities on both sides of the shock, the shock is called a genuine shock. Both types of shocks occur in typical solutions. Because the tie lines that make up the solution can be found by the intersecting tie line approach[70, 71, 33] a full solution can be constructed if the shock composition points can be determined on each of the key tie lines. The only remaining question is: On which tie line does solution construction begin. We will refer to that tie line as the "primary" tie line.

Solution construction begins with finding the tangent shocks that connect the primary tie line to adjacent tie lines just upstream and downstream. For problems in which the injection gas composition lies on the vapor side of the two-phase region, the composition path lies on the vapor side of the equivelocity curve (where $f = S$)[30]. For such compositions, $f > S$.

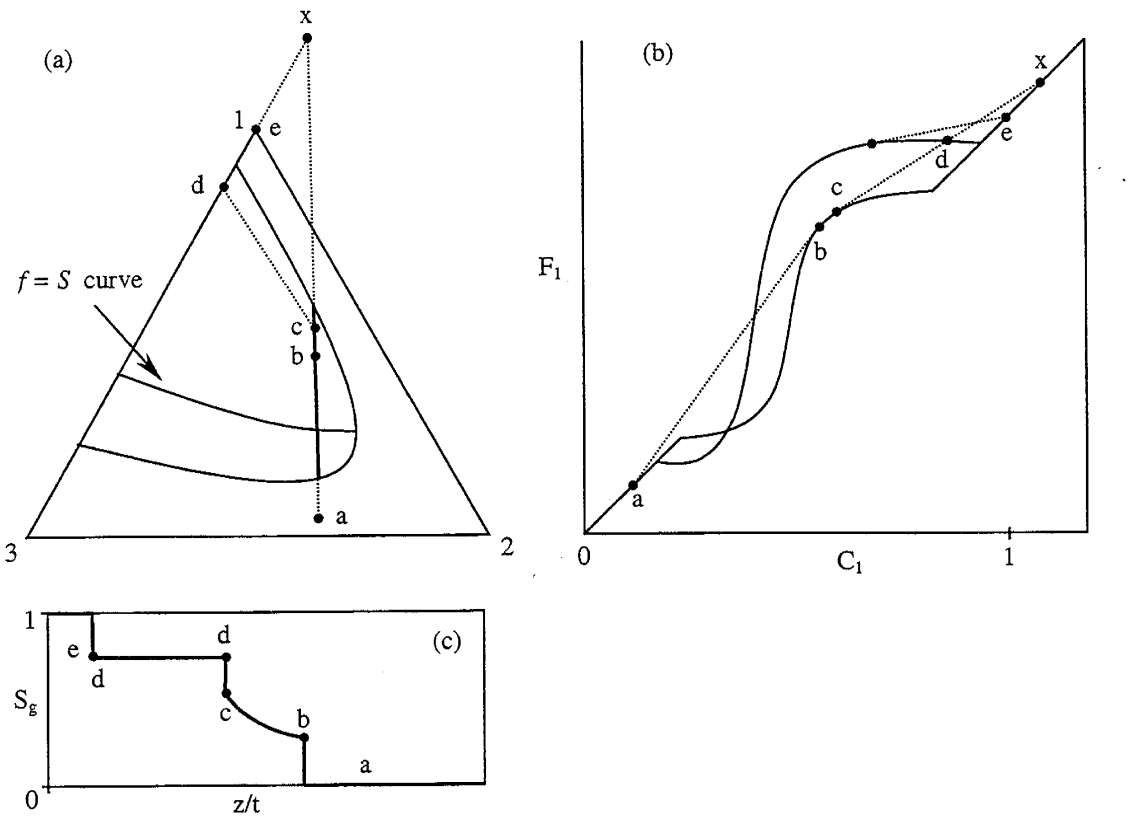

Figure 3.1: Construction of tangent shocks.

We show now that the primary tie line must be the shortest of the key tie lines. To see why this statement must be true, we consider a simple ternary vaporizing gas drive (Fig. 3.1a) in which oil (composition a) is displaced by gas (composition e). Two key tie lines make up the solution: the tie line that extends through the initial oil composition, and the tie line that extends through the gas composition. In this example, the tie lines are connected by a shock because a rarefaction between the oil tie line and the gas tie line would violate the velocity rule. The corresponding overall fractional flow curves for the two key tie lines are shown in Fig. 3.1b, and the saturation profile for the solution is shown in Fig. 3.1c. In this case, the leading shock is a tangent shock, found by constructing the chord from point a in Fig. 3.1b that is tangent to the fractional flow curve for the oil tie line. The shock from point c on the oil tie line is found by constructing a chord from point X that is tangent to the fractional flow curve for the oil tie line. Point X (Fig. 3.1a) is the intersection point of the two key tie lines. Point X in Fig. 3.1b lies on the $F1 = C1$ line. The composition of point d, the landing point on the gas tie is given by the intersection of the chord with the fractional flow curve of the gas tie line. Note that point d lies above the composition at which a chord constructed from the gas composition, point e, would be tangent to the fractional flow curve for the gas tie line. A continuous variation from point d to that tangent point would violate the velocity rule, so a genuine shock from point d to point e is required. The velocity of that shock is given by the slope of the chord from point d to point e.

The tangent drawn from point X to point c in Fig. 3.1b satisfies the following equations[35]:

$$\frac{F_i^c - F_i^d}{C_i^c - C_i^d} = \frac{F_i^c - C_i^x}{C_i^c - C_i^x} = \frac{F_i^d - C_i^x}{C_i^d - C_i^x} = \frac{f^c - S^{cx}}{S^c - S^{cx}} = \frac{S^d - S^{dx}}{S^d - S^{dx}} = \left.\frac{df}{dS}\right|_c, \tag{3.8}$$

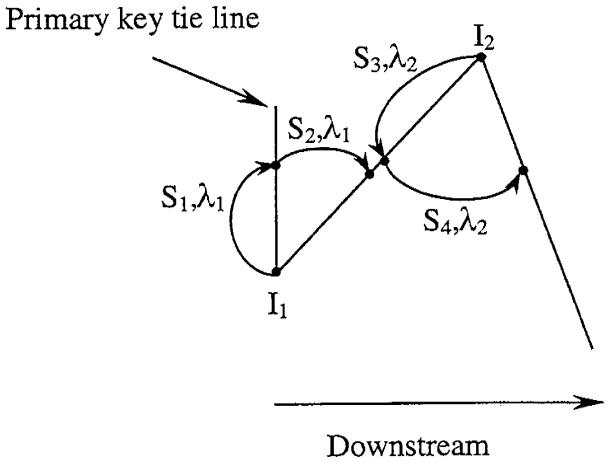

Figure 3.2: Illustration of downstream solution path construction.

where S^{cx} and S^{dx} refer to the saturations at point X measured on the tie lines containing points c and d:

$$S^{cx} = \frac{C_1^x - c_{1l}^c}{c_{1v}^c - c_{1l}^c}, S^{dx} = \frac{C_1^x - c_{1l}^d}{c_{1v}^d - c_{1l}^d}. \tag{3.9}$$

Fig. 3.1b shows that the tangent constructed from point c to X intersects the overall fractional flow curve for the injection gas tie line at point d. If, on the other hand, the chord had been drawn from point X to the tangent point on the gas tie line, the extension of the chord would not intersect the overall fractional flow curve for the oil tie line. Thus it is not possible to satisfy the shock equations if the tangent were constructed to the gas tie line, but it is possible to do so for the oil tie line. Analysis of the shock equations indicates that it is always possible to satisfy the shock equations for this example if $S^{cx} > S^{dx}$. That restriction is controlled by the length of the tie lines. In this example, the oil tie line is short, and the gas tie line is longer, so $c_{1v}^c - c_{1l}^c < c_{1v}^d - c_{1l}^d$. Because the differences in c_{1l}^c and c_{1l}^d are small, the length of the tie lines dominates the saturations in Eq. 3.9. Thus, if a shock between two tie lines is a tangent shock, the tangent must be constructed to the shorter of the two tie lines.

Similar reasoning can be applied sequentially to each adjacent pair of tie lines, with the result that in fully self-sharpening systems the shortest of the $n_c - 1$ key tie lines must be a tie line that is connected to tie lines just upstream and downstream by tangent shocks. The tangents constructed from the intersection points to the shortest tie line. Therefore, the shortest tie line is the primary tie line.

The algorithm for construction of fully self-sharpening 1D solutions is:

1. Locate all key tie lines using the tie line intersection approach. The global solution algorithm of Jessen *et al.*[33] was used here.

2. Locate the primary (shortest) key tie line and start tracing the solution upstream and downstream. For each adjacent pair of tie lines, the possibility of a tangent construction is initially investigated. The construction procedure is illustrated in Fig. 3.2.

3. Downstream construction: A tangent construction is made by solving Eq. 3.8 for (S_1, λ_1) on the primary tie line from the first downstream intersection point (I_1). The landing point

on the down-stream tie line (S_2, λ_1) is subsequently found by solving Eq. 3.8 with the shock velocity fixed.

4. For the next downstream pair, intersecting at I_2, a new tangent construction is examined. From this point and forward the tangent construction may be invalid due to a violation of the velocity rule. That is, if the endpoint of the previous construction (S_2, λ_1) has a velocity that is higher than the jump or landing point from new shock construction (S_3, λ_2). In such a case, the new pair of tie lines is connected by a genuine shock. A genuine shock is followed by a constant state. If, on the other hand, two tangent constructions are made to the same tie line the tangent points are connected by either a direct jump or by continuous variation along the tie line.

5. Step 4 is repeated until the tie line extending through the initial oil is reached. The solution path often enters (and leaves) the two-phase region by a tangent shock. For some systems, (Fig. 3.1, for example), however, variation along the tie line violates the velocity rule and a direct jump is used.

6. From the primary tie line, the solution path is traced upstream by the approach of steps 3 and 4.

3.4 Solution Example for Fully Self-Sharpening System

The algorithm for construction of self-sharpening solutions has been applied for a real reservoir fluid. The reservoir fluid was characterized by the procedure of Pedersen *et al.*[54] into a 15 component fluid description. The properties of the characterized fluid are given in Table 3.1. The reservoir temperature is 387.45 K at which the bubble point pressure of the original oil (A) is 252 atm. The pure component critical volumes V_c, used for the prediction of phase viscosities, were calculated by specifying the critical compressibility factor of all components to 0.307. We seek the 1D solution for the displacement of oil A by gas A at 275 atm.

The fourteen key tie lines (those extending through the oil and gas compositions and twelve crossover tie lines) were determined[33], and the third crossover tie line was identified as the primary (shortest) tie line, the starting point for shock construction. The saturation profile is shown in Fig. 3.3, and the details of the solution are given in Table 3.2. The primary tie line is connected to the first downstream tie line by a tangent shock (d1). The remaining downstream part of the solution consists of genuine shocks, constant states, and a direct jump from the oil tie line to the initial oil composition. The upstream part of the solution starts with a tangent shock (d2) connecting the primary tie line to the next crossover tie line. The remaining upstream shocks are all genuine shocks with associated constant states, and another genuine shock connects the injection gas tie line with the injection gas composition. A continuous variation connects the two shock points (d1 and d2) on the primary tie line.

In order to confirm the analytical solution, a series of finite difference (FD) simulations was performed. Single-point upstream weighting with a Courant number $(\Delta z/\Delta t)$ of 10 was used in all the simulations which were run on a 450 MHz PC. The new two-phase PT-flash algorithm developed by Michelsen[44] was used in the FD simulator to speed up the numerical solutions. The numerical saturation profiles from simulations using 100, 1000 and 10000 grid blocks are compared with the analytical profile in Fig. 3.3. The CPU time required to construct the analytical solution was 0.9 second, compared to 4.4 seconds, 5.4 minutes and 7.8 hours used respectively by the numerical simulations. The coarse grid simulation (100 grid blocks) is not able to describe the details but only the general trend of the dispersion-free solution. More details are captured using 1000 grid blocks and an excellent agreement is observed when using 10000 grid blocks. However, the CPU

Comp.	T_c(K)	P_c(atm)	ω	M_w(g/mole)	x-Oil A	y-Gas A
N_2	126.200	33.6000	0.0400	28.016	0.450	0.49
CO_2	304.200	72.9000	0.2280	44.010	1.640	1.82
CH_4	190.600	45.4000	0.0080	16.043	45.850	81.39
C_2	305.400	48.2000	0.0980	30.069	7.150	9.15
C_3	369.800	41.9000	0.1520	44.096	6.740	4.67
i-C_4	408.100	36.0000	0.1760	58.123	0.840	0.50
n-C_4	425.200	37.5000	0.1930	58.123	3.110	1.24
i-C_5	460.400	33.4000	0.2270	72.150	1.030	0.20
n-C_5	469.600	33.3000	0.2510	72.150	1.650	0.26
C_6	507.400	29.3000	0.2960	86.177	2.520	0.09
C_7	632.800	30.2987	0.1842	109.007	12.440	0.19
C_{11}	659.605	23.4598	0.4773	175.327	6.320	0.00
C_{16}	703.646	19.2900	0.8197	256.674	5.024	0.00
C_{23}	766.497	16.7852	1.2114	370.099	3.240	0.00
C_{33}	892.990	15.1302	1.3718	590.374	1.996	0.00

Table 3.1: Characterized fluid description (SRK - Equation of state).

Point	Tie line	μ_{gas}/μ_{oil}	Log (K_{nc})	Z_{nc}	S	λ
Oil	Initial	0.1719	-5.80352	0.019957	-	1.9972 - ∞
a	Initial	0.1719	-5.80352	0.011376	0.321	1.4501 - 1.9972
b	1	0.1758	-5.70171	0.010801	0.344	1.2170 - 1.4501
c	2	0.1740	-5.73387	0.010972	0.338	1.1270 - 1.2170
d_1	3	0.1879	-5.46043	0.008974	0.424	1.1270
d_2	3	0.1879	-5.46043	0.008732	0.438	1.0187
e	4	0.1782	-5.64053	0.007761	0.509	0.9505 - 1.0187
f	5	0.1774	-5.65381	0.007727	0.512	0.9086 - 0.9505
g	6	0.1674	-5.83705	0.007376	0.547	0.8407 - 0.9086
h	7	0.1608	-5.95911	0.007205	0.567	0.8155 - 0.8407
i	8	0.1500	-6.16425	0.007001	0.595	0.7360 - 0.8155
j	9	0.1281	-6.60241	0.006702	0.646	0.4823 - 0.7360
k	10	0.0705	-7.72998	0.006246	0.780	0.3521 - 0.4823
l	11	0.0391	-8.54209	0.006109	0.862	0.1630 - 0.3521
m	12	0.0219	-9.01158	0.006151	0.927	0.0351 - 0.1630
n	Inj.	0.0150	-9.12906	0.008519	0.960	0.0163- 0.0351
o	Inj.	0.0150	-9.12906	0.000049	1	0- 0.0163
Gas	Inj.	0.0150	-9.12906	0.000000	-	0

Table 3.2: MOC solution for displacement of Oil A by Gas A at 275 atm and 387 K.

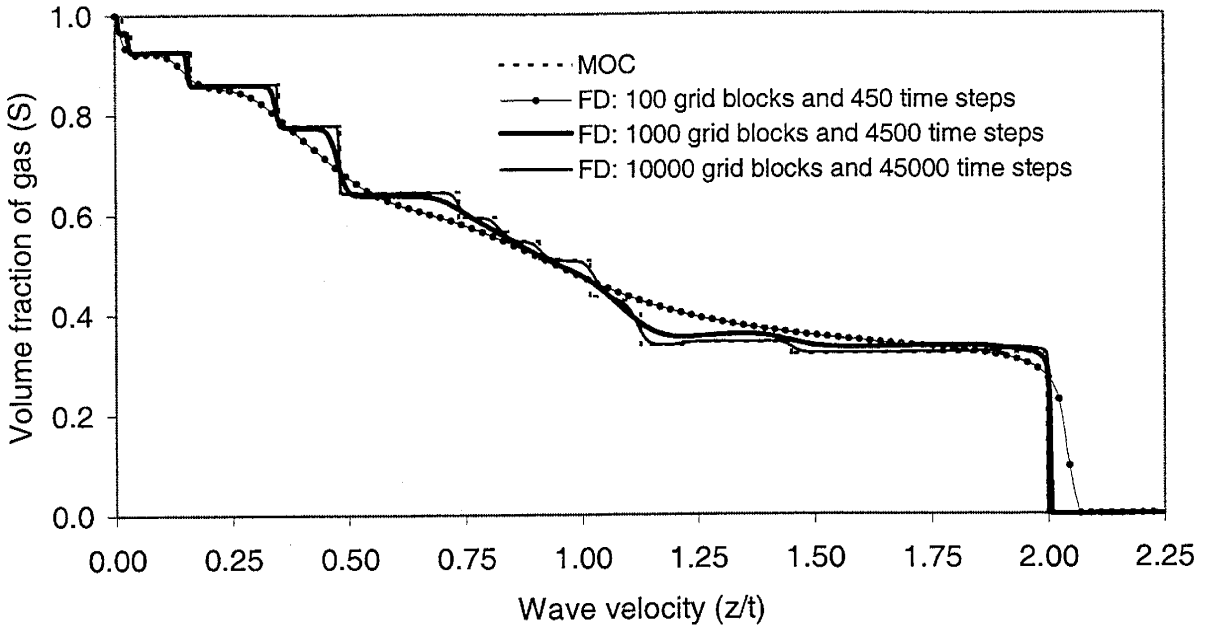

Figure 3.3: Comparison of analytical and numerical saturation profiles for displacement of Oil A by Gas A at 275 atm and 387.45 K. The finite difference (FD) solutions were obtained with 100, 1000, and 10,000 grid blocks and $\Delta z/\Delta t = 10$.

cost for capturing the true dispersion-free saturation profile by numerical simulators is substantially higher.

3.5 Systems with Nontie-Line Rarefactions

The shock solution described in the previous sections can be found even when there is a rarefaction connecting one or more pairs of tie lines. In many problems, rarefaction segments that appear are short, and wave velocities change little over the length of the rarefaction. In such cases, the shock solution is an excellent approximation of the actual solution. For problems with longer rarefactions, a more accurate approximate solution can be obtained by the procedure described in this section.

The mass conservation equations of the 1D flow problem can be rearranged into the eigenvalue problem

$$(A - \lambda I)e = 0, \tag{3.10}$$

where A is a coefficient matrix, I is the unit matrix, λ is the eigenvalue and e the corresponding eigenvector. The elements of the A are given by

$$A_{j,i} = \frac{\partial F_j}{\partial C_i}, \; i,j = 1,\ldots,n_c - 1. \tag{3.11}$$

At any given point in the two-phase region, the $n_c - 1$ eigenvalues represent characteristic wave velocities of compositions subject to variation in the corresponding eigenvector direction. Tie lines are eigenvectors and the remaining $n_c - 2$ admissible directions can be integrated to obtain nontie-line paths. When a nontie-line rarefaction exists in the 1D solution, the solution path switches from a key tie line path and travels along a nontie-line path to end up at a neighboring key tie line. The velocity rule dictates that a path switch from a tie line path to a nontie-line path

can occur only at an equal-eigenvalue point of mixed type. That is a point in compositional space where a tie line eigenvalue coincides with a nontie-line eigenvalue. For a given tie line the number of equal-eigenvalue points of mixed type is $2(n_c - 2)$. Half of them can be disregarded immediately, as they are located on the liquid side of the equivelocity curve. The equal eigenvalue points can be located directly by solving the eigenvalue problem along a given tie line. The direct approach is quite time consuming and hence, the indirect method of Dindoruk (p. 64)[18] for location of equal-eigenvalue points is recommended for problems of the current type.

In the following we assume that two key tie lines, known in advance, are connected by a spreading wave. The question is then: at what equal-eigenvalue point does the tie line path switch to the nontie-line path?

The selection of the appropriate equal eigenvalue point can be done by a geometrical interpretation of the displacement problem. When a rarefaction is present, the key tie lines bound a surface in composition space of tie lines intersected by the path that connects the key tie lines. The nontie-line spreading wave traverses that surface. Experience indicates that the tie-line surface is only slightly curved, so it can be approximated well by a plane determined by the key tie lines. Hence, at the correct equal-eigenvalue point only the tie-line eigenvector and the eigenvector related to the matching nontie-line eigenvalue will point in direction of the plane Q spanned by the neighboring key tie lines. In practice this is done by checking angles between the normal vector to Q and the eigenvectors. Note that for systems with 5 or more components in the mixture, the normal vector to Q is no longer uniquely determined and must be found by a minimization approach.

After the selection of equal-eigenvalue point, the nontie-line path is traced to the next key tie line by integration of the nontie-line eigenvector. For the general case, however, the presence of a spreading wave is not known in advance. Hence, a tool for predicting the existence of nontie-line rarefactions is needed.

3.6 Prediction of Spreading Waves in 1D Solutions

If two key tie lines are connected by a rarefaction, the path switch from the tie line path to the nontie-line path must occur at an equal eigenvalue point on the tie line located closest to the critical locus. This is due to the intrinsic symmetric behavior around critical points. In the work of Dindoruk[18], continuous variation along nontie-line paths is linked to the envelope curve generating the ruled surface traveled by the nontie-line path. This envelope curve is illustrated in a 2-dimensional projection of the general case in Fig. 3.4. The tie lines belonging to the 1-parameter family $\varphi_k(\psi)$ on the kth ruled surface are all tangents to the envelope curve E_k. The overall volume fraction of a given component i at the point of tangency on the envelope curve can be written as

$$C_i = (c_{iv} - c_{il})P_k(\psi) + c_{il}, \tag{3.12}$$

where $P_k(\psi)$ is the superficial vapor volume fraction at the point of tangency. Dindoruk[18] derived an expression for the variation of the nontie-line eigenvalue λ_k along the nontie-line path in the vicinity of the equal eigenvalue point

$$\frac{d\lambda_k}{d\psi} = \frac{f - S}{(S - P_k)^2}\frac{dP_k}{d\psi} \tag{3.13}$$

where λ_t is the tie line eigenvalue at the equal eigenvalue point. While Eq. 3.13 applies strictly only near the equal-eigenvalue point, the indicated sign of the left-hand side applies over the entire nontie-line path[18].

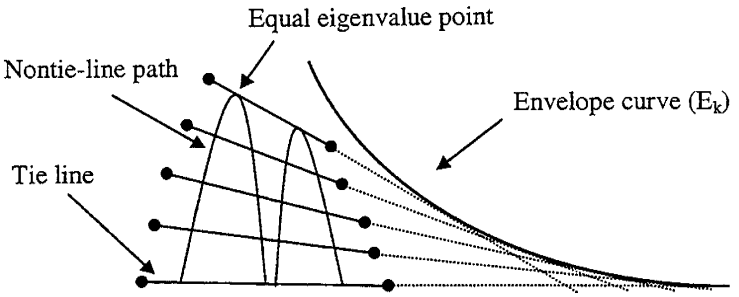

Figure 3.4: Illustration of envelope curve.

3.7 The Fanning Rule (Envelope Rule)

Inspection of Eq. 3.12 indicates that a critical point must be a point on the envelope curve. This fact makes it possible to predict the sign of the derivative of the superficial vapor saturation with respect to ψ and hence the variation of λ_k once the orientation of the key tie lines is known. The absolute distance from the two-phase boundary to the envelope curve increases as the nontie-line path is traced from an equal eigenvalue point. The sign of the superficial vapor fraction depends on whether the tie lines of the ruled surface are fanning from the liquid side or the vapor side of the two-phase region, or equivalently, whether the envelope curve is located in the vapor or liquid side of the two-phase region. Ultimately the shape of the fractional flow curve and the velocity rule are used to determine whether a path switch at an equal eigenvalue point is admissible. Recall that the velocity rule states that a high-speed wave must be found downstream of a low-speed wave. For systems in which the injection composition lies on the vapor side of the phase envelope and the initial composition on the liquid side, the solution path (after the leading shock) lies on the vapor side of the equivelocity curve ($f > S$). This fixes the sign on the numerator on the right hand side of Eq. 3.13, and hence the derivative of the nontie-line eigenvalue has the same sign as the derivative of the superficial vapor saturation P_k. Application of the fanning (envelope) rule in combination with the velocity rule result in four distinct cases illustrated in Figs. 3.5-3.8.

The first case illustrated in Fig. 3.5 is a vaporizing wave where the envelope curve is located on the liquid side of the two-phase region. As the nontie-line path is traced from the equal eigenvalue point located downstream (d) towards the injection point located upstream (u), the superficial vapor saturation P_k decreases. This is consistent with the velocity rule and hence the path switch is allowed and a spreading wave will be present in the 1D solution.

Fig. 3.6 shows a condensing wave in which P_k is increasing as the nontie-line path is traced from a point upstream (u) towards the initial oil. This is consistent with the velocity rule and hence a spreading wave will form in the solution.

In the condensing drive illustrated in Fig. 3.7, P_k is a decreasing function of the nontie-line path when traced from a point upstream (u) towards the initial oil. This is a violation of the velocity rule, as the upstream part of the wave eventually will catch up with the downstream part. In other words, the wave is self-sharpening. The upstream and downstream key tie lines must consequently be connected by a shock. Depending on the compatibility with the solution this can be either a tangent shock or a genuine shock.

Fig. 3.8 shows a vaporizing wave with the envelope curve located on the vapor side of

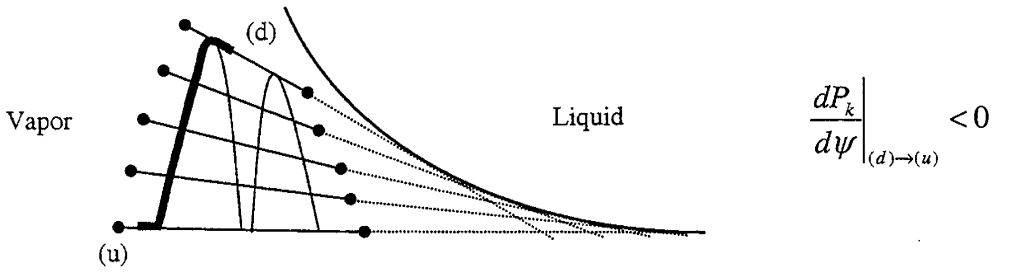

Figure 3.5: Vaporizing wave with liquid side envelope. Upstream (u), Downstream (d).

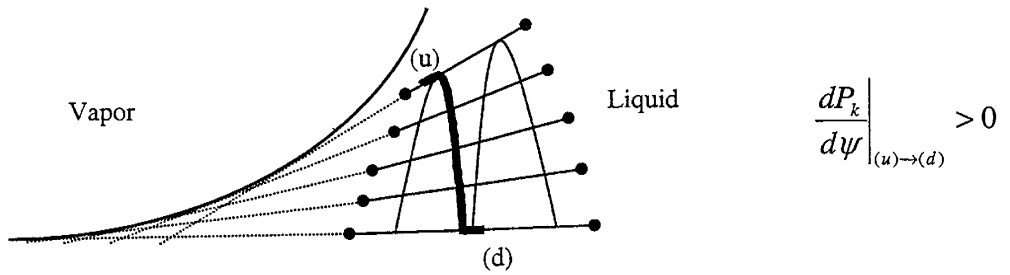

Figure 3.6: Condensing wave with vapor side envelope.

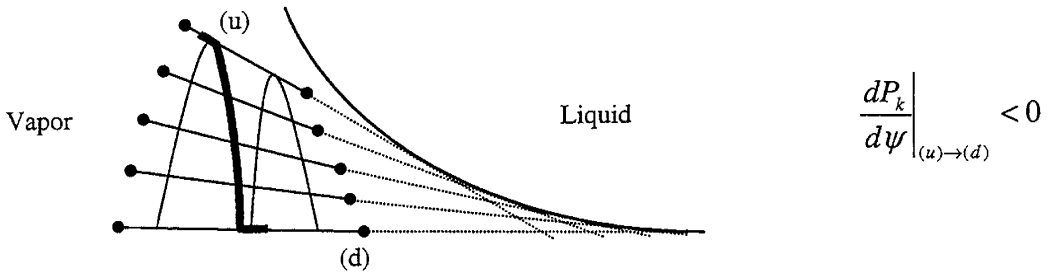

Figure 3.7: Condensing wave with liquid side envelope.

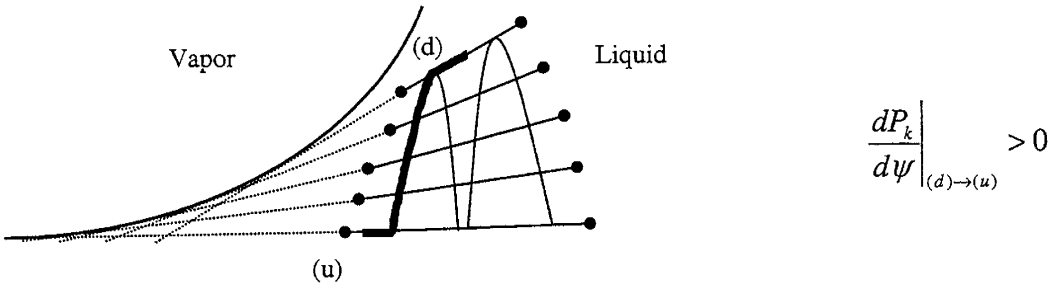

Figure 3.8: Vaporizing wave with vapor side envelope.

Type	Tie line length		Intersection	Wave
	Upstream	Downstream		
Vaporizing	Long	Short	Liquid side	Rarefaction
Vaporizing	Long	Short	Vapor side	Shock
Condensing	Short	Long	Liquid side	Shock
Condensing	Short	Long	Vapor side	Rarefaction

Table 3.3: Summary of the fanning (envelope) rule.

the two-phase region is inspected. As the nontie-line path is traced from a point upstream (u) towards the injection point, the nontie-line eigenvalue increases. Again this behavior will result in a sharpening wave, a path switch at the equal eigenvalue point is not allowed and a shock is required.

The general feature of the four cases presented above is that a spreading wave only will form if the nontie-line path, starting at the equal eigenvalue point, is moving away from the envelope curve. Whether a rarefaction appears between two key tie lines can be summarized easily in terms of tie line length and whether the intersection point lies on the liquid or vapor side of the two-phase region. Table 3.3 reports that summary. Vaporizing segments occur when a longer key tie line lies upstream of a shorter key tie line (see Figs. 3.5 and 3.8), and in vaporizing segments, a rarefaction occurs when the intersection between the key tie lines lies on the liquid side of the two-phase region. In condensing segments, a shorter key tie line is upstream of a longer one (see Figs. 3.6 and 3.7), and a rarefaction occurs when the intersection is on the vapor side. Additional analysis is required to determine whether rarefactions appear if either the initial oil or the injection gas composition is in the two-phase region.

3.8 Algorithm for Systems with Nontie-line Rarefactions

The algorithm for constructing 1D solutions, honoring the existence of spreading waves, is:

1. Locate all key tie lines by the tie line intersection approach.

2. Apply the fanning rule for each neighboring pair of key tie lines. If no rarefactions are predicted switch to the simplified algorithm for fully self-sharpening systems.

3. For each predicted rarefaction, locate the equal-eigenvalue point and integrate the eigenvalue problem to obtain the corresponding nontie-line path.

4. Locate the primary key tie line and start the shock construction downstream. Switch points between the nontie-line paths and the tie line paths are introduced in the solution requirements in parallel with the velocity rule. The downstream solution is traced until the initial oil composition is reached.

5. Continue constructing the upstream solution by the approach of step 4 until the injection gas composition is reached.

3.9 Solution Example with Nontie-line Rarefaction

The appearance of nontie-line rarefactions is commonly observed in the solution path for displacements when N_2 is present in the injected gas. To illustrate the limits of the algorithm used for constructing fully self-sharpening solutions, pure N_2 is now injected into the reservoir fluid (oil A) at the same temperature and pressure as previously. The saturation profile generated by the algorithm for fully self-sharpening systems is compared with coarse and fine grid numerical simulations in Fig. 3.9. The saturation profile from the fine grid simulation clearly indicates a nontie-line rarefaction between the initial tie line and the first crossover tie line. Fig. 3.9 further illustrates the saturation profile obtained by combining an integration of the nontie-line path with shock constructions as described previously.

For this system, the tie line extending through the initial oil is the primary tie line. Application of the fanning rule indicates that a nontie-line rarefaction connects the initial tie line and the first crossover tie line. The nontie-line path ends at an overall composition approximately located on the adjacent tie line. The inaccuracy of the approximation introduced by assuming intersecting key tie lines is quite small, as Table 3.4 shows. The observed deviation is of an order of magnitude where the numerical evaluation of the coefficient matrix A and the step by step integration may contribute significantly. To avoid any violation of the mass conservation equations, the first crossover tie line was connected to the end point of the nontie-line path by a genuine shock. The downstream solution consists of a continuous variation along the initial tie line and a tangent shock to the initial oil. Genuine shocks and constant states make up the upstream part of the solution until the injection tie line is reached. Finally the solution is completed by a direct jump to the injection composition.

Fig. 3.9 indicates that the fully self-sharpening solution is a much more refined approximation than the one obtained by a coarse grid numerical simulation.

3.10 Conclusions

The analysis and examples presented lead to the following conclusions:

1. The tie line intersection approach can be applied to find solutions for 1D-gas displacement problems with an arbitrary number of components in the initial oil and injection gas.

2. The solutions obtained are rigorously correct for fully self-sharpening systems.

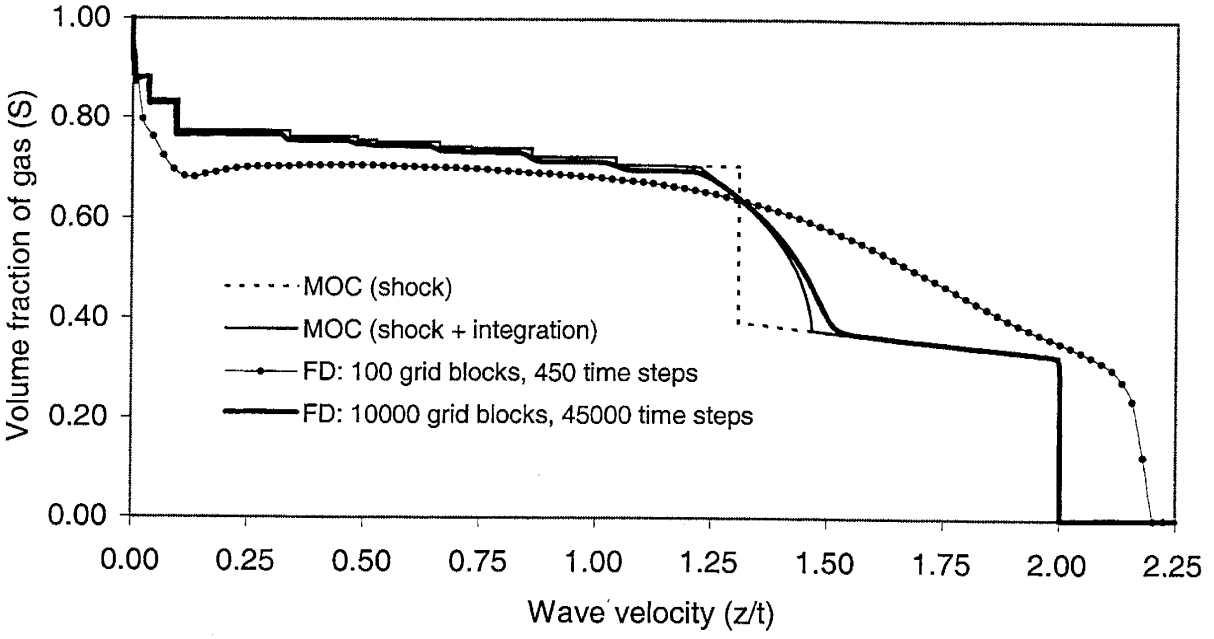

Figure 3.9: Comparison of analytical solutions (with and without integration) with numerical saturation profiles for the displacement of Oil A by pure n_2 at 275 atm and 387.45 K. The finite difference (FD) solutions were obtained using 100 and 10,000 grid blocks and $\Delta z/\Delta t = 10$.

Comp.	x (shock)	x (rarefaction)	Error %	y (shock)	y (rarefaction)	Error %
N_2	0.23695463	0.23657449	0.16	0.86905145	0.87052697	0.17
CO_2	0.00892119	0.00896803	0.52	0.01255008	0.01262557	0.60
CH_4	0.00000000	0.00000000	-	0.00000000	0.00000000	-
C_2	0.06295753	0.06196958	1.59	0.05199391	0.05114823	1.65
C_3	0.07434362	0.07361960	0.98	0.03517118	0.03476156	1.18
i-C_4	0.01007617	0.00998769	0.89	0.00333684	0.00329854	1.16
n-C_4	0.03922843	0.03896883	0.67	0.01076864	0.01066283	0.99
i-C_5	0.01382016	0.01374001	0.58	0.00260091	0.00257527	1.00
n-C_5	0.02260102	0.02248533	0.51	0.00376605	0.00373032	0.96
C_6	0.03645991	0.03630629	0.42	0.00382992	0.00379312	0.97
C_7	0.20213968	0.20233382	0.10	0.00585749	0.00581241	0.78
C_{11}	0.10787320	0.10827271	0.37	0.00095891	0.00095155	0.77
C_{16}	0.08952057	0.09020739	0.76	0.00011148	0.00011053	0.86
C_{23}	0.05901420	0.05964260	1.05	0.00000305	0.00000300	1.37
C_{33}	0.03608969	0.03692364	2.26	0.00000009	0.00000009	0.88

Table 3.4: Comparison of tie line found by MOC integration and by the tie line intersection approach. Gas A displaced by pure N_2 at 275 atm and 387 K.

3. The presence of a rarefaction between key tie lines can be determined easily from the lengths of the upstream and downstream tie lines and whether the intersection point lies on the vapor side or the liquid side of the two-phase region.

4. For displacements that include nontie-line rarefactions, the solutions obtained by the tie line intersection approach are approximate, but they are much more accurate than solutions obtained by conventional finite difference compositional simulation unless impractically fine computational grids are used.

5. Times required to obtain approximate analytical solutions by the key tie line method are orders of magnitude lower than corresponding times for conventional compositional simulation.

3.11 Nomenclature

A = Coefficient matrix
C_i = Overall volumetric fraction of component i
c_{il} = Volumetric fraction of i in liquid phase
c_{iv} = Volumetric fraction of i in vapor phase
e = Eigenvector
F_i = Overall fractional flow of component i
f = Fractional flow of vapor
I = Identity matrix
M = Viscosity ratio (vapor/liquid)
n_c = Number of components in mixture
P = Superficial vapor saturation
S = Volumetric vapor saturation
λ_t = Tie-line eigenvalue
λ_k = kth nontie-line eigenvalue
Λ = Shock velocity

4. Nested Gridding and Streamline Simulation

Yann Gautier, Martin J. Blunt, and Michael A. Christie

Detailed reservoir models routinely contain 10^6 to 10^8 grid blocks. These models often cannot be used directly in a reservoir simulation because of the time and memory required for solving the pressure grid on the fine grid. In this chapter, we propose a nested gridding technique that efficiently obtains an approximate solution for the pressure field. The domain is divided into a series of coarse blocks, each containing several fine cells. Effective mobilities are computed for each coarse grid block and the pressure is then found on the coarse scale. The pressure field within each coarse block is computed using flux boundary conditions obtained from the coarse pressure solution. Streamline-based simulation is used to move saturations forward in time. We test the method for a series of example waterflood problems and demonstrate that the method can give accurate estimates of oil production for large *3D* models significantly faster than direct simulation using streamlines on the fine grid, making the method overall approximately up to 1,000 times faster than direct conventional simulation.

4.1 Introduction

Reservoir models containing millions of grid blocks frequently cannot be used directly in reservoir simulation since the time and memory cost is too high. Instead the reservoir simulation is performed on a coarser grid on which average multiphase flow properties are defined. The process of finding effective properties is called upscaling and in recent years many different methods have been proposed (see [14, 51] for recent reviews).

For single-phase flow problems, the absolute permeability has to be upscaled. Several reliable methods can be found in the literature [51]. In contrast, upscaling for multiphase flow is not so well established although several methods of "pseudoization" have been developed (see Barker [6] and references therein for a review on that subject). However most of the time the results are not robust and depend highly on the particular boundary conditions used.

Recently another approach has been considered: instead of doing the simulation only on a coarse gridding of the reservoir, both the fine and the coarse scales are considered. Gautier and Nœtinger [26] used this idea for single phase flow problems. They upscaled the full absolute permeability tensor using renormalization and they proposed an algorithm to construct the fine grid fluxes based on the the upscaled grid properties. The preferential flow paths were well detected but the orientation of the fluxes wasn't accurate due to a bias of the algorithm.

Ramé and Killough [57] used a multiscale method to solve miscible flow problems. They interpolated on a fine grid the pressure obtained from a coarser grid solution. They first used a collocation finite element method to interpolate, which leads to non physical oscillatory variations of the pressure. The results were then improved using a a spline method. The main problem of their method was that the mass conservation was not ensured from their interpolation scheme. Moreover the fine grid heterogeneities were not directly considered.

Verdière and Guérillot [29, 67] applied a dual scale approach for waterflooding problems that overcome the limitations of the method developed by Ramé and Killough [57]. As before, saturation was computed on a fine grid and the pressure on a coarser grid. They also associated two different time scales to the pressure and to the saturation equations. The algorithm they used

[3]The material in this chapter will be published in Computational Geosciences.

can be divided in different steps. First, considering the fine grid information, they upscaled values of the product of the absolute permeability and of the mobility (the transmissivity) using a simple algebraic rule. They then solved the pressure equation on the coarse grid. In the next step they computed the fine grid pressure and the fluxes using flux boundary conditions derived from the coarse grid pressure. With this information they updated the saturation solving the associated hyperbolic equation. All their computations were done using a finite difference simulator on a *2D* field with simple boundary conditions: prescribed rates or pressures on two opposite corners of the reservoir. They neglected gravity and capillary pressure. The results were on good agreement with the fine grid simulation leading to a precision gain over typical upscaling methods. Guedes and Schiozer [28] used a similar method with a different upscaling step. Instead of an algebraic rule, they used a pseudo method to obtain the upscaled transmissivities. They showed the improvment of their methods with respect to coarse grid simulations using upscaled absolute permeabilities or pseudo relative permeabilities.

In a subsequent paper, Verdière and Vignal [68] showed mathematically that their method converges to the exact solution using a finite volume formalism. They also computed numerical error estimates on a few test cases. In a more general framework, Hou and Wu [31] have developed a multiscale finite element approach for solving pressure-like equations. This is a mathematically rigorous technique whereas the method developed by Verdière and Guérillot is approximate and broadly corresponds to the first step of a multigrid method.

In this chapter, we will apply this type of algorithm to solve the pressure equation within a streamline-based multiphase flow simulation [7, 65]. Streamline-based simulation has been shown to give fast and reliable estimates of the solution of different flow simulation problems. The streamline method is briefly as follows. The grid pressure is first computed and the velocity field is derived using Darcy's law. Streamlines are then traced from injectors to producers. The next step is to solve the one-dimensional saturation equation on every streamline and map the saturations back to the original grid. The grid properties are finally updated and the pressure is solved for the next time step.

A multiscale approach for streamline-based simulation is appealing for several reasons. The first motivation is to increase the speed of the streamline method. Streamline methods can be up to 100 times faster and require less memory than a typical finite difference simulation [7, 65]. As we will see the new method will provide an additional speed-up factor of nearly one order of magnitude, with a saving of up to 40% of the memory cost. Hence, bigger problems can potentially be considered than by using conventional simulation. Another motivation is that using a multiscale method to solve the pressure equation can provide a fully parallel method since all the upscaling problems and the computation of the fine grid pressure are independent and can be made parallel easily. This is also the case for the saturation equation which has been split into series of small one-dimensional problems.

We will implement this nested gridding streamline-based flow simulation within a more general framework than the one used by Verdière and Guérillot [29, 67]. We will show how to treat wells and how to incorporate *3D* effects by computing an equivalent gravity transmissivity. To upscale fine grid transmissivities, we will use the pressure solve technique which has been shown to be more robust than other upscaling methods [51, 53]. This step requires the solution of small linear systems to obtain the fine grid block pressure with prescribed boundary conditions. The exiting flux is then computed and the effective transmissivity is derived using Darcy's Law. To optimize the CPU cost of a pressure evaluation we will select different solvers for the different problems we encounter. For the small problems that we have to solve during the upscaling step and during the pressure computation on the fine grid we use a band solver that is particularly efficient for small linear systems. A multigrid or an iterative solver is used for larger problems on the coarse scale. Therefore nested gridding provides us a flexible way to save CPU time for the computation of the

pressure since we adapt the type of solver used to the size of the problem considered.

First, we briefly review the streamline method, then we develop our new technique, and lastly, we present results in *2D* and *3D* with and without gravity.

4.2 The streamline method

We consider multiphase flow with the following assumptions: we neglect capillary, compressibility and dispersion effects. The streamline method is an IMPES method (IMplicit in Pressure and Explicit in Saturation). The pressure p is solved using the following differential equation [4]:

$$\nabla \cdot \mathbf{k} \ (\lambda_t \nabla p + \lambda_g \nabla D) = Q \tag{4.1}$$

D represents the depth, Q the source terms due to wells, $\mathbf{k}$ the absolute permeability tensor, λ_t and λ_g the total mobility and total gravitational mobility respectively for n_p phases, defined as:

$$\lambda_t = \sum_{j=1}^{n_p} \frac{k_{r_j}}{\mu_j}, \quad \lambda_g = \sum_{j=1}^{n_p} \frac{k_{r_j} \rho_j g}{\mu_j} \tag{4.2}$$

where g is the gravitational acceleration constant and ρ_j is the density of phase j. The material balance for phase j leads to the saturation equation:

$$\phi \frac{\partial S_j}{\partial t} + \mathbf{u}_t \cdot \nabla f_j + \nabla \cdot \mathbf{G}_j = Q_w f_{j,w} \tag{4.3}$$

where f_j represents the Buckley-Leverett fractional flow of phase j:

$$f_j = \frac{k_{r_j}/\mu_j}{\sum_{m=1}^{n_p} k_{r_m}/\mu_m} \tag{4.4}$$

and $\mathbf{G}_j$ is the velocity due to gravity effects:

$$\mathbf{G}_j = g \, f_j \, \mathbf{k} \nabla D \sum_{m=1}^{n_p} \frac{k_{r_m}}{\mu_m} (\rho_m - \rho_j) \tag{4.5}$$

The total velocity $\mathbf{u}_t$ is computed from the pressure solution of Eq. 4.1, using Darcy's law:

$$\mathbf{u}_t = \mathbf{k} \ (\lambda_t \nabla p + \lambda_g \nabla D) \tag{4.6}$$

In a conventional finite difference method, the saturation equation, Eq. 4.3 is solved directly on the *3D* field. With the streamline method, the problem is decoupled into a set of *1D* problems along streamlines.

The streamlines are traced from injectors to producers. Their paths are determined from the total velocity computed for each grid block face using an analytical method developed by Pollock [56]. The saturation is then moved along each streamline using a numerical solution of the *1D* problem. Finally, the saturation is mapped onto the grid blocks. The pressure field is then recomputed and new streamlines are traced. The different steps are pictured in Figure 4.1.

The streamline method has two main advantages over conventional finite difference simulators [7, 65]. It requires fewer simulation time steps and it is less sensitive to numerical diffusion. The maximum time step between two pressure solves in a conventional IMPES simulator is conditioned by a global CFL constraint which requires that the fluid cannot move more than one grid block per time step. Typically, the CFL constraint is determined from the largest flow velocity in the whole field leading to unnecessarily small time steps. In the streamline method, a local CFL constraint

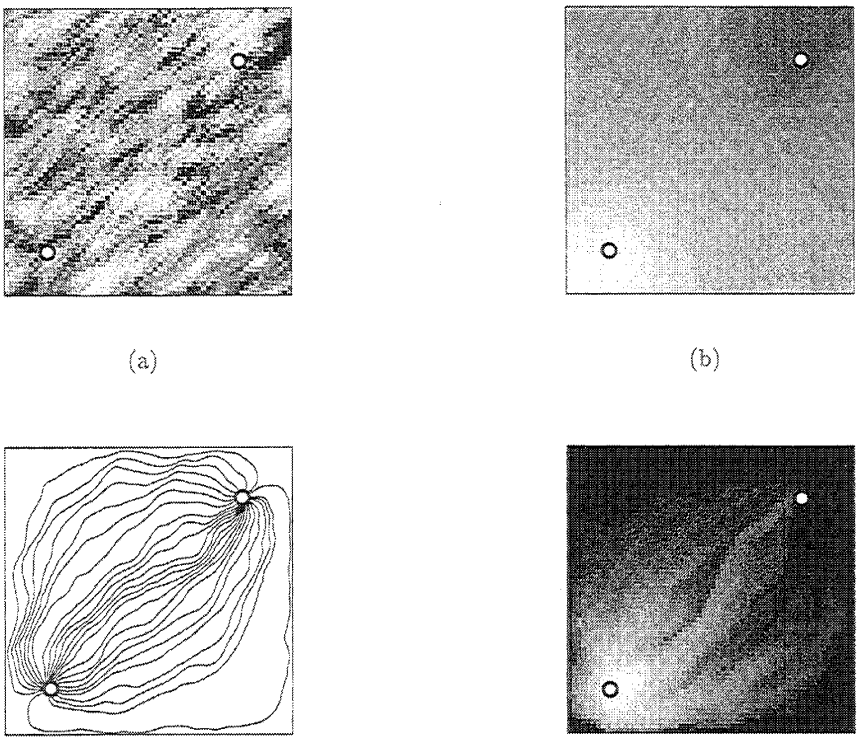

Figure 4.1: Description of the streamline method. Consider a permeability map *(a)* with injector and a producer wells. Solve the pressure field *(b)*. Compute the velocity field and trace streamlines *(c)*. Move saturation along streamlines and compute the values of the saturation on the grid *(d)*.

is defined for every streamline and the saturation is updated using a *1D* solver. Large global time steps can be taken between pressure solves. The most time consuming step for both streamline and conventional approaches is the solution of the pressure equation Eq. 4.1. In our proposal method we use an approximate pressure solver based on nested gridding in order to decrease the CPU time of the simulation.

4.3 Description of the new method

The basic idea of the nested gridding method is to decouple the pressure problem into a set of smaller problems on two scales: we consider a coarse grid superimposed on a fine grid (Figure 4.2). We assume that the initial petrophysical properties are defined on the fine grid. The first step of the nested gridding method is to upscale these properties on the coarse scale. The pressure equation Eq. 4.1 is solved on the coarse scale. The next step is to go back to the fine grid, solving a set of local problems within each coarse grid block using boundary conditions derived from the previous step.

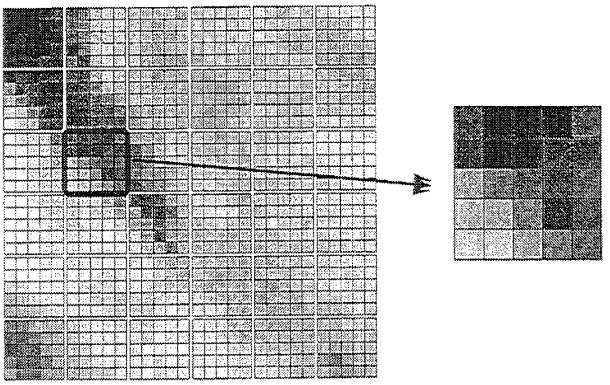

Figure 4.2: Representation of the coarse grid superimposed on a fine grid. The right figure represents a particular coarse grid block

Let us first recall the finite difference equation related to the pressure equation. Using a seven point stencil, the pressure is determined from the classical relation [4]:

$$\begin{aligned} & T_{z,k-\frac{1}{2}} P_{i,j,k-1} + T_{y,j-\frac{1}{2}} P_{i,j-1,k} + T_{x,i-\frac{1}{2}} P_{i-1,j,k} \\ - \; & P_{i,j,k} \left(T_{z,k-\frac{1}{2}} + T_{y,j-\frac{1}{2}} + T_{x,i-\frac{1}{2}} + T_{z,k+\frac{1}{2}} + T_{y,j+\frac{1}{2}} + T_{x,i+\frac{1}{2}} \right) \\ + \; & T_{z,k+\frac{1}{2}} P_{i,j,k+1} + T_{y,j+\frac{1}{2}} P_{i,j+1,k} + T_{x,i+\frac{1}{2}} P_{i+1,j,k} \\ = \; & Q_{i,j,k} + G_{z,k-\frac{1}{2}} D_{i,j,k-1} - G_{z,k+\frac{1}{2}} D_{i,j,k} \end{aligned} \tag{4.7}$$

where the right hand side contains source terms induced by the boundary conditions Q and by the difference of elevation between the considered grid block and its neighbors (for a cartesian grid only the neighbors in the vertical direction have a nonzero contribution). i, j, k are respectively the indices of a block in the x, y, z directions. $T_{\bullet,\bullet\pm\frac{1}{2}}$ represents the inter-block transmissivities which is the harmonic average of the block transmissivities. For example, in the x direction, with $(\Delta x_i, \Delta y_i, \Delta z_i)$ representing the size of the grid block:

$$T_{x,i+\frac{1}{2}} = \frac{2}{\frac{1}{T_{x,i}} + \frac{1}{T_{x,i+1}}} \tag{4.8}$$

where the transmissivity of each fine grid block is:

$$T_{x,i} = \frac{\Delta y_i \Delta z_i}{\Delta x_i} \lambda_{t,i} k_{x,i} \tag{4.9}$$

$G_{\bullet,\bullet\pm\frac{1}{2}}$ represents the inter-block gravity transmissivities which is the harmonic average of the block gravity transmissivities. For example, in the x direction,

$$G_{x,i+\frac{1}{2}} = \frac{2}{\frac{1}{G_{x,i}} + \frac{1}{G_{x,i+1}}} \tag{4.10}$$

where the transmissivity of each fine grid block is:

$$G_{x,i} = \frac{\Delta y_i \Delta z_i}{\Delta x_i} \lambda_{g,i} k_{x,i} \tag{4.11}$$

Eq. 4.7 can also be represented in a matrix form

$$\mathbf{TP} + \mathbf{GD} = \mathbf{Q}; \tag{4.12}$$

where $\mathbf{T}$ and $\mathbf{G}$ are the transmissivity and gravity transmissivity matrices, $\mathbf{P}$ and $\mathbf{D}$ are vectors containing the pressure and the elevation of the different grid blocks.

4.3.1 The upscaling step

In the following we will focus on one particular type of upscaling: the pressure solve technique [9, 51, 53, 55, 42]. This method is widely used and it has been shown to be more robust than other faster techniques such as simple averaging rules and renormalization [51, 40, 26].

In our nested gridding method we compute two different upscaled quantities: the transmissivities and the gravity transmissivities. Let N be the number of coarse grid blocks and m the number of fine grid blocks contained in each coarse grid block. We take an isolated coarse grid block (I, J, K) and solve the pressure equation (Eq. 4.7) on the underlying fine grid with suitable boundary conditions. To compute the effective transmissivities in the direction $d = x, y, z$, Eq. 4.7 is solved using constant pressure boundary conditions on the d direction and no-flux boundary conditions on the other directions. We neglect gravity for these computations. Once the pressure is obtained inside the coarse grid block, the exiting flux q^c is computed and the effective transmissivity of each coarse grid block is derived using Darcy's law. In the x direction:

$$T^c_{I,x} = \frac{q^c}{\Delta X_I \Delta P_x} \tag{4.13}$$

where ΔP_x is the pressure drop and ΔX_I is the length of the coarse grid block in the x direction. This process is repeated in the two remaining directions to obtain $\mathbf{T}^c = \left(T^c_x, T^c_y, T^c_z\right)$ for all the coarse grid blocks. The upscaling process in the x direction is depicted in Figure 4.3.

To compute the effective gravity transmissivity, we are using the same method as before but with different boundary conditions. Since a Cartesian grid is considered, only the z direction effective gravity transmissivity will have a nonzero value which we call $G^c_{I,z}$. To solve the fine scale problem, we consider no-flux boundary condition on the x and y faces of the block and a constant gravity g along the z direction. No pressure drop is applied on the two opposite faces in the z direction. $G^c_{I,z}$ is computed from the exiting flux with:

$$G^c_{I,z} = \frac{q^c}{g\ \Delta Z_I} \tag{4.14}$$

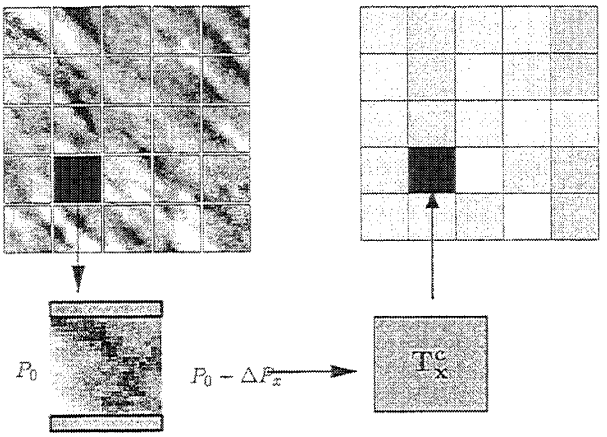

Figure 4.3: Upscaling of the transmissivities: the fine transmissivity map is divided into coarse grid blocks. The pressure equation is solved independently on each coarse grid block with a no flux boundary on all the faces except two opposing faces across which a prescribed pressure drop is applied. The upscaled values of the transmissivities are then obtained from the computation of the flux across the system.

The upscaling is repeated for every coarse grid block. Each coarse block is characterized by three upscaled transmissivities and one upscaled gravity transmissivity. Note that the effects of the fine grid saturation distribution is accounted for in $\mathbf{T}^c$ and $G^c_{I,z}$, and that, in order to compute the different effective parameters we split the influence of the viscous and gravitational forces. The different upscaling steps are described in Figure 4.4.

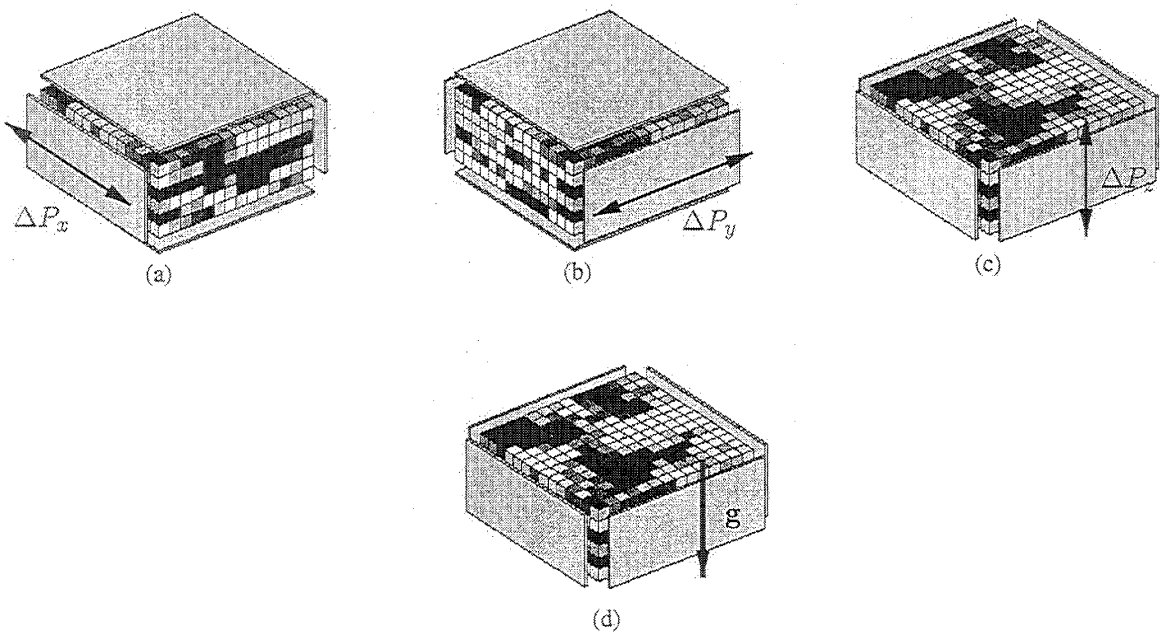

Figure 4.4: Upscaling of the transmissivity in the three directions *(a-c)* where a constant pressure drop ΔP_d is applied on the direction d and the gravity is set to $g = 0$. *(d)* depicts the upscaling of the gravity transmissivity where $\Delta P_z = 0$ and $g \neq 0$.

4.3.2 Pressure solve on the coarse grid

The second step of the method is to compute the pressure on the coarse scale using Eq. 4.7 with the effective transmissivities $\mathbf{T}^c$. Here the right hand side contains the source terms induced by the wells. To represent the wells we use the Peaceman model [52]. In the next step, the pressure at the coarse scale will be used to derive the pressure field at the fine scale.

4.3.3 Computation of the pressure on the fine grid.

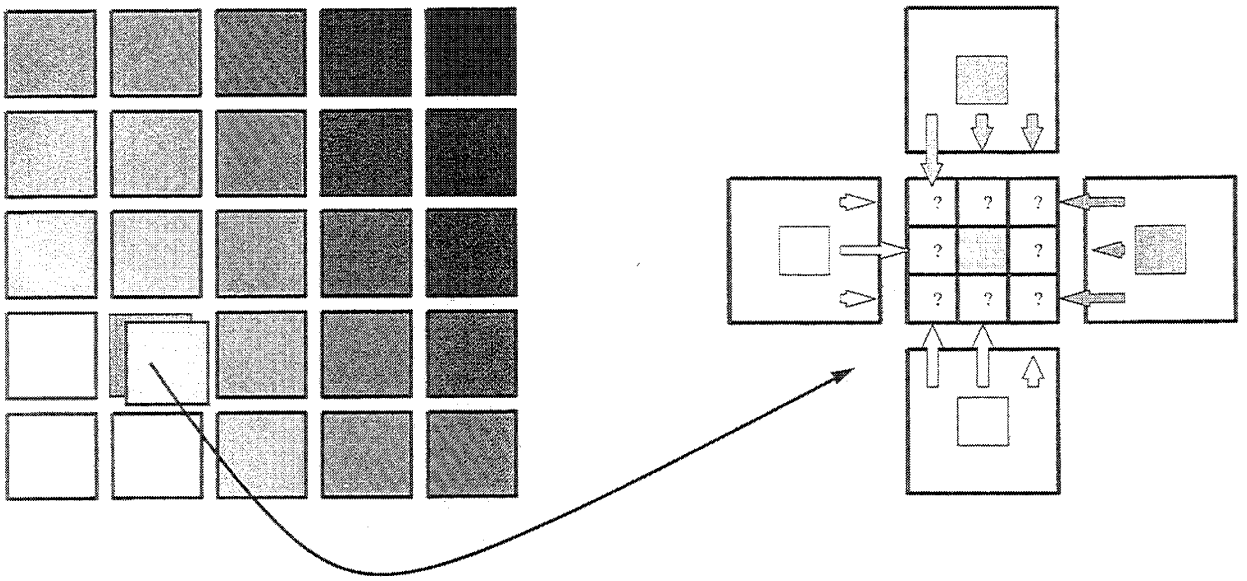

Figure 4.5: Computation of the fine grid pressure field using the pressure of the coarse grid and the fluxes coming from the neighboring coarse grid blocks. The fluxes are computed using Darcy's law and are weighted by the inter-blocks transmissivities.

The pressure on the fine grid is obtained from the former step by solving the pressure equation on each coarse grid block. Let us consider a particular coarse grid block. It contains m fine grid blocks whose pressures will be derived from Eq. 4.7 using the following boundary conditions: the pressure at the central fine grid block is assumed known and equal to the pressure of the coarse grid block. Furthermore, the fluxes at the boundaries of the fine grid are assumed to be equal to q^c (the flux computed from the coarse pressure solution using Darcy's law) weighted by the inter-block transmissivities $T_{\bullet,\bullet\pm\frac{1}{2}}$ [67]. For instance, the fine grid flux in the x direction for a particular grid block (i,j,k) located on the right boundary is:

$$q^f_{x,i} = q^c_x \times \frac{T_{x,i+\frac{1}{2},j,k}}{\sum_{l_j,l_k} T_{x,i+\frac{1}{2},l_j,l_k}} \tag{4.15}$$

In the sum, (l_j, l_k) are the indices in the y and z directions of the grid blocks located on the boundary. The upscaling step is described in Figure 4.5.

For coarse grid blocks perforated by a well, we modify slightly the above algorithm. The fluxes along each faces are still considered to be computed with Eq. 4.15. We will require that the pressures at the grid blocks perforated by the well are defined such that the rates are globally the same on both the fine grid and the coarse grid. Let $q^{c,w}$ be the rate flowing from the well from a particular coarse grid block containing n_l layers. We assume that the well rate coming from

each perforated layer l is equal to $q^{c,w}$ weighted by the well transmissivity of the layer T_l^w which is defined in Peaceman's well model [52, 4]. We thus have:

$$q_l^{f,w} = \frac{T_l^w}{\sum_{i=1}^{n_l} T_i^w} \times q^{c,w} \tag{4.16}$$

$q_l^{f,w}$ is related to the well pressure at the top well grid block completion (k^*), $P_{k^*}^w$:

$$q_l^{f,w} = T_l^w \left(P_{k^*}^w - P_l + \frac{1}{2} \sum_{i=k^*+1}^{l} (\gamma_{i-1} + \gamma_i)(D_i - D_{i-1}) \right) \tag{4.17}$$

where the wellbore specific gravity is defined by:

$$\gamma_i = \frac{\lambda_{g,i}}{\lambda_{t,i}} \tag{4.18}$$

Using Eq. 4.16 and Eq. 4.17 we obtain the pressure of the fine grid block:

$$P_l = P_{k^*}^w - \frac{q^{c,w}}{\sum_{i=1}^{n_l} T_i^w} + \sum_{i=k^*+1}^{l} (\gamma_{i-1} + \gamma_i)(D_i - D_{i-1}) \tag{4.19}$$

This method ensures that the flow will preferentially exit the well through high transmissivity layers.

Once the pressure is defined on the fine grid, we compute the velocity field in order to trace streamlines. To ensure continuity of the fluxes, the velocity field is computed from the fine grid pressure within each coarse grid block volume, and from the coarse fluxes on the boundaries, Eq. 4.15, that were used in the pressure solution on the fine grid. Once the streamlines are defined, the saturation is moved forward in time as in a standard streamline method. The pressure field and streamlines are periodically recomputed during the displacement. The saturation is always defined on the fine grid and is used in the computation of $\mathbf{T}^c$ and $\mathbf{G}$ for the coarse grid.

Figure 4.6 summarizes the different steps of the nested grid method. Note that only the steps *(2-4)* are different from the classical streamline method where they are replaced by a pressure solve over the entire fine grid.

4.4 CPU cost evaluation for the nested gridding method

We will present in this section a comparison of the CPU cost for the conventional streamline-based simulation against our new nested gridding approach. We compare the CPU time needed to solve Eq. 4.7 for both methods. The other steps in the simulation are similar for the two methods. The CPU time needed to solve directly the pressure equation on the fine grid is:

$$t^{(\text{direct})} = t(N \times m) \tag{4.20}$$

In the nested gridding method, the time $t^{(\text{nested})}$ required to solve the pressure equation in $d = 2, 3$ dimensions is the sum of three terms:

$$\begin{aligned} t^{(\text{nested})} &= (d + 1_g)\, N\, t(m) && (4.21) \\ &+ t(N) && (4.22) \\ &+ N\, t(m) && (4.23) \end{aligned}$$

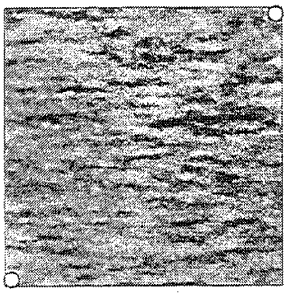

(a) Fine grid transmissivity map

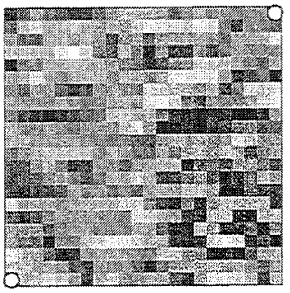

(b) Coarse grid transmissivity map

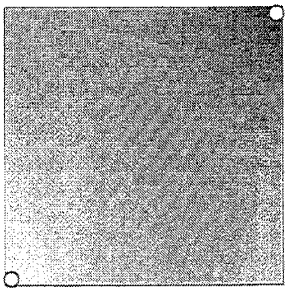

(c) Pressure on the coarse grid

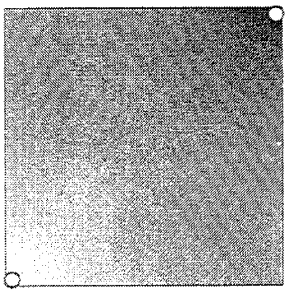

(d) Pressure on the fine grid

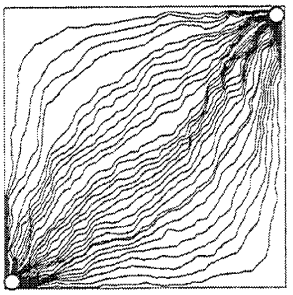

(e) Streamlines on the fine grid

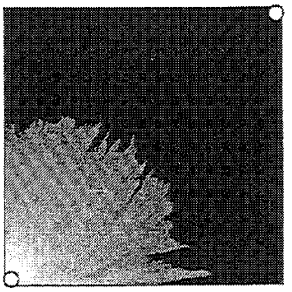

(f) Saturation on the fine grid

Figure 4.6: Description of the different steps of the nested gridding method. We first consider a fine description of the reservoir *(a)*. The transmissivities are then upscaled on a coarse scale *(b)* and a pressure solution on the coarse grid is computed *(c)*. The next step is the computation of the pressure on the fine grid *(d)* which leads to the velocity field. The streamlines are traced from the injector to the producer *(e)* and saturation is moved using the classical streamline method *(f)*.

The first term Eq. 4.21, represents the amount of time necessary to solve the N small linear systems needed to perform the upscaling in d directions of the transmissivities and the upscaling of the gravity transmissivities assuming that the time required to get the solution is $t(m)$. 1_g is equal to 1 or 0 depending on whether or not gravity is considered. The second term, Eq. 4.22, represents the time needed to solve the pressure field on the coarse scale and the last term Eq. 4.23 is the time needed to solve compute the pressure inside all the different coarse grid blocks. Adding these terms we obtain:

$$t^{(\text{nested})} = (d + 1_g + 1)\, N\, t(m) + t(N) \qquad \text{with } d = 2, 3 \tag{4.24}$$

For the upscaling step, for *3D* problems, three or four linear systems have to be solved to compute the effective transmissivities in the three directions and the gravity transmissivities. But, since the same transmissivity matrix, is used three times and is stored in memory, the required time is less than 3 or $4\,Nt(m)$.

The nested gridding method requires us to solve multiple linear systems whose sizes are highly different: typically for the upscaling step and the computation of the fine grid pressure, the system will contain $10 - 100$ unknowns, whereas for the computation of the coarse grid pressure the number of unknowns is $10^4 - 10^5$. One key issue of the nested gridding method is its ability to use the most appropriate solver at each scale to obtain the lowest CPU time cost. In the next section different solvers are presented and tested. We will see that their performances are sensitive to the number of unknowns as well as to the available computer memory.

4.5 CPU requirements of different pressure solvers

The pressure is solved from Eq. 4.7. Typically, considering all the grid blocks, we obtain a banded linear system of equations. The bandwidth depends on the total number of grid blocks and on the numbering of the grid blocks. Figure 4.7 and Figure 4.8 represent the shape of the matrix formed with the transmissivity of the reservoir in *3D* and *2D* (only nonzero elements are represented). Adding well constraints leads to additional off-diagonal terms.

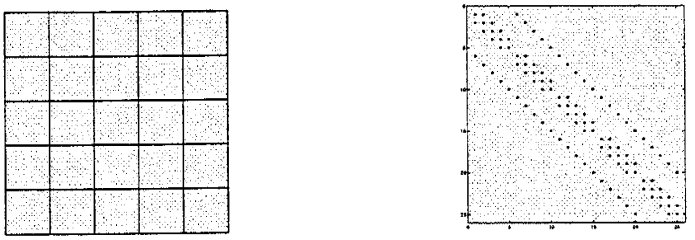

Figure 4.7: *2D*grid with $n_x = 5$, $n_y = 5$ and the corresponding transmissivity sparse matrix. Only nonzero elements are represented.

We will use three different public domain solvers:

- a band solver *DGBSV* from the *LAPACK* library [3].
- an iterative solver from the *ITPACK* library [39].
- a multigrid solver *AMG* [63].

The performance and memory requirements of these two solvers are very different. For the band solver, the data are stored in an $N_b \times N_t$ array, where N_b and N_t represent respectively the bandwidth

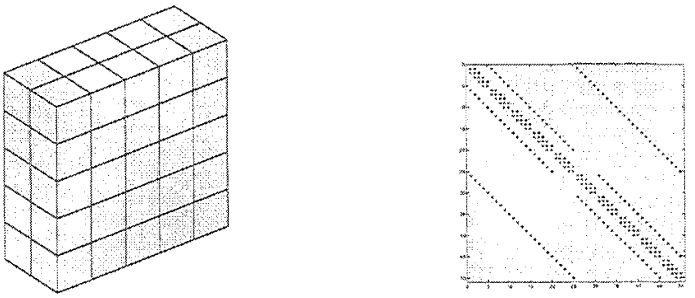

Figure 4.8: *3D*grid with $n_x = 2$, $n_y = 5$ and $n_z = 5$ and the corresponding sparse matrix. Only nonzero elements are represented.

and the total number of grid blocks. The storage space increases quickly with the system size and makes this method only suitable for problems containing less than 30,000 grid blocks in *2D* using a DEC alpha workstation with 512MB RAM. The iterative solver and the multigrid solver both use a storage which is proportional to a weighted sum of the number of nonzero elements and the total number of grid blocks, N_t. The iterative solver takes also advantage of the symmetric properties of the transmissivity matrix. Only one half of the nonzero elements are stored. A 500,000 grid block problem was the largest case we could run with our computer using the multigrid solver, whereas problems with up to two million grid blocks were possible using the iterative solver.

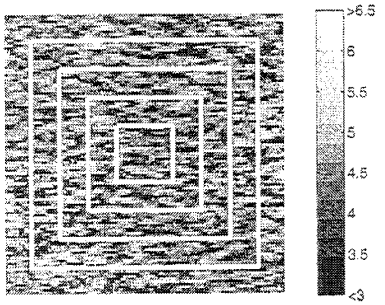

(a)

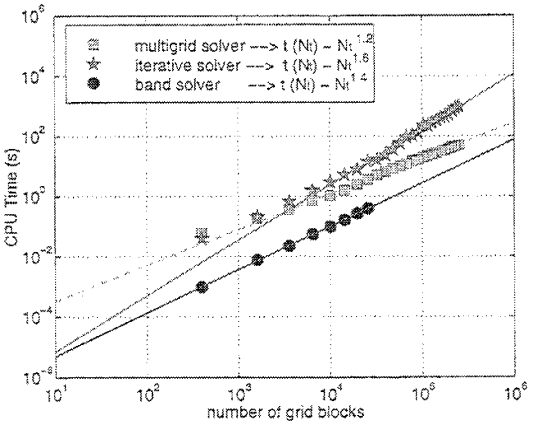

(b)

Figure 4.9: Heterogeneous permeability fields (a), in a log-scale, used to compare the CPU time needed to solve the pressure. There are all extracted from a 500×500 permeability field. (b) is the CPU time comparison for a pressure solve using different solvers for *2D* problems.

We now compare the CPU cost of different solvers for *2D* problems. We consider a permeability field (500×500 grid blocks) generated using a sequential gaussian simulation [16]. The pressure equation is solved for permeability fields extracted from it with a prescribed pressure on two opposing faces and no flux boundary on the two other faces. The construction of the different permeability fields is depicted in Figure 4.9(a). The CPU time needed for the pressure solve is plotted as a function of the total number of grid blocks N_t in Figure 4.9(b) for the three available solvers.

For a sufficiently large number of grid blocks the time for a pressure solve using the multigrid

Table 4.1: CPU time (in s) and memory (in MB) comparisons for a pressure solve on *3D* permeability fields of varying size.

Dimension ($n_x n_y n_z$)	ITPACK		AMG	
	RAM	CPU	RAM	CPU
30^3	11	4.4	27	4.1
50^3	35	52	110	63
70^3	86	250	294	275
90^3	178	703	-	-

solver scales as $N_t^{1.2}$, as $N_t^{1.8}$ for the iterative solver and as $N_t^{1.4}$ for the band solver. The band solver uses less CPU time than the two other methods. The drawback is that the memory requirements are so high that it can be use for only relatively small problems, such as the computation of the pressure within each coarse grid block during the upscaling step. The multigrid solver is always faster than the iterative solver when considering more than ten thousand grid blocks for *2D* problems.

In the nested gridding method, the band solver is used for the upscaling step as well as for the computation of the pressure back to the fine grid. The pressure on the coarse grid is computed using the multigrid method, or the iterative method if the memory requirements are too high. As an example, we can evaluate a first approximation of the speed-up factor for 600×600 grid blocks. The time required to solve the pressure equation directly on the fine grid, using the *AMG* solver, is about 80 s. For the nested gridding approach, using a 3×3 upscaling factor, the time to solve the pressure field from Eq. 4.24 is:

$$\begin{aligned} t^{(\text{nested})}(600 * 600) &= 3 * 200 \times 200 \times t(9) + t(200 * 200) \\ &= 3 * 4.2\,10^{-6} \times 40000 + 6.2 \\ &= 6.7\,s \end{aligned}$$

The speed-up factor is around 10 for this example.

Table 4.1 shows some comparisons of the solvers for *3D* problems. Here, the iterative solver is as fast as the multigrid solver. Hence, the iterative solver will be used to solve the pressure field on the coarse scale since the memory requirements are lower. As an evaluation of the speed-up factor, let us consider a permeability field containing $90 \times 90 \times 90$ grid blocks with an upscaling factor $(3 \times 3 \times 1)$ (The effective transmissivity in the z direction is simply the arithmetic mean of the fine grid transmissivities and the factor $(d+1)$ in Eq. 4.24 is actually close to 3). We neglect gravity effects. Using Table 4.1 and Figure 4.9(b) (since each pressure solve for a single coarse grid block is a *2D* problem), the time needed for the upscaling method is 20 s leading to a speed-up factor equal to 35. In all these evaluations, the construction of the different transmissivity matrices on the coarse and on the fine scale and the different data manipulations involved by the nested gridding method were not considered. Therefore, the speed-up factors may be overestimated.

4.6 Results

In this section, we will compare the results provided by the streamline method with the new nested gridding method. The streamline simulator is 3DSL [7, 65], and the subroutines for the pressure solve have been updated for the new nested gridding method.

The permeability fields used in this part are generated with a indicator algorithm (*SISIM*) from the GSLIB library [16]. These fields are characterized by three (*3D*) or two (*2D*) correlation lengths l_x, l_y, l_z and by the different value of the permeability facies. The cases study are waterflood problems with two wells, a producer and an injector with prescribed pressure. The fluid viscosity

ratio between oil and water is $\mu_o/\mu_w = 10$. The relative permeability curves are quadratic functions of the saturations. We will compare saturation maps and recovery curves for three methods:

1. The nested gridding method.
2. Streamline simulation on the fine grid.
3. Streamline simulation on the coarse grid where the absolute permeability is upscaled as described in this chapter. There is no upscaling of relative permeability. We call this the upscaling method.

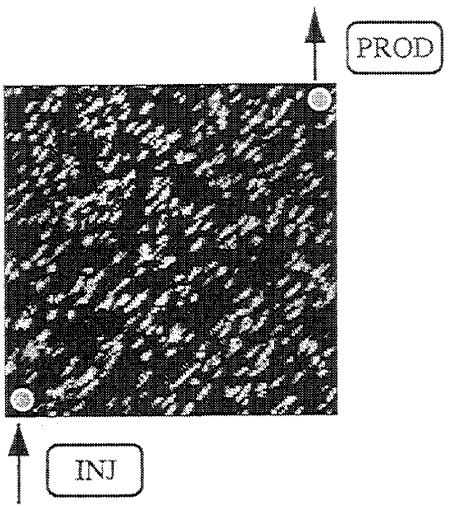

Figure 4.10: Permeability field containing 270 × 270 grid blocks with two facies. Permeability: k(black) = 100 mD and k(white) = 0.1 mD. Proportion of black facies: 90%. Correlation length: 10 grid blocks in the x and y directions with an anisotropy angle of 45°

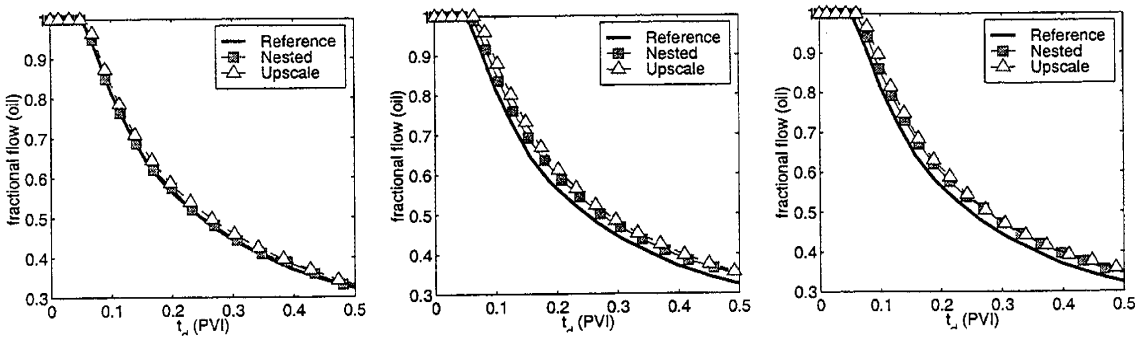

(a) (3 × 3) (b) (9 × 9) (c) (27 × 27)

Figure 4.11: Fractional flow of oil at the producer for different upscaling factors and for the three methods (fine grid, nested gridding and upscaling). Case *RES1*.

4.6.1 Numerical results for two-dimensional reservoirs

Figure 4.10 represents a permeability field *RES1* containing two facies with $n_x = n_y = 270$ grid blocks, $l_{cx} = l_{cy} = 10$ (in grid block units). The black facies represents grid blocks with a

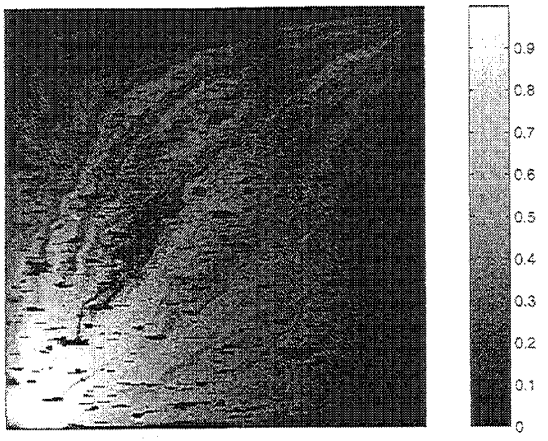

(a) Fine grid simulation

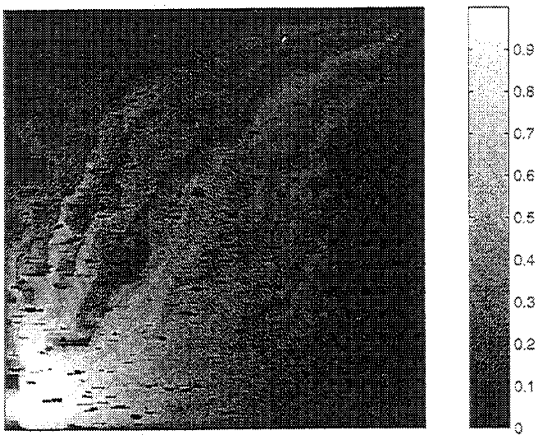

(b) Nested gridding method

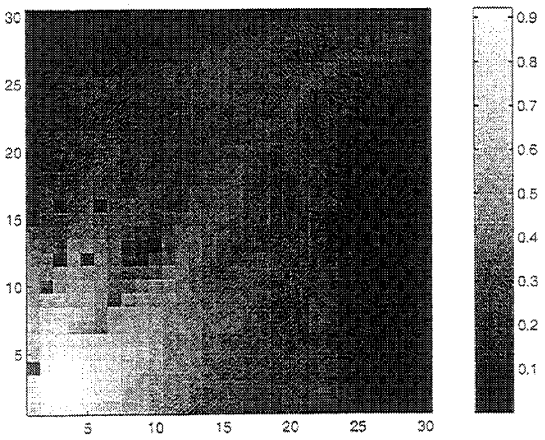

(c) Upscaling method

Figure 4.12: Water saturation maps from the fine grid simulation *(a)*, from the nested gridding simulation *(b)* and from the simulation on the upscaled absolute permeabilities *(c)* for 0.35 PVI. The upscaling factor is 9×9. Case *RES1*.

permeability equal to 100 mD. The white facies permeability is 0.1 mD. The proportion of the black facies is 90%. Water is injected from the lower-left corner well and the fractional flow of oil is observed at the producer (upper-right corner). Results are shown in Figure 4.11 for the three methods and for three upscaling factors (each coarse grid blocks contains 3×3, 9×9 or 27×27 fine grid blocks). We can see that for the smallest upscaling factors, both the nested gridding and the upscaling give good approximations of the reference fine grid simulation. When we coarsen, the difference increases between the fine grid simulation and the two approximate methods. The nested gridding is slightly better than upscaling. The saturation maps for the three methods are shown in Figure 4.6 for a 9×9 upscaling factor for 0.35 PVI. Fine grid details are captured by the nested gridding methods, while only the main features of the flow are detected by upscaling.

We now consider a more demanding problem with greater channeling. Figure 4.13 represents a

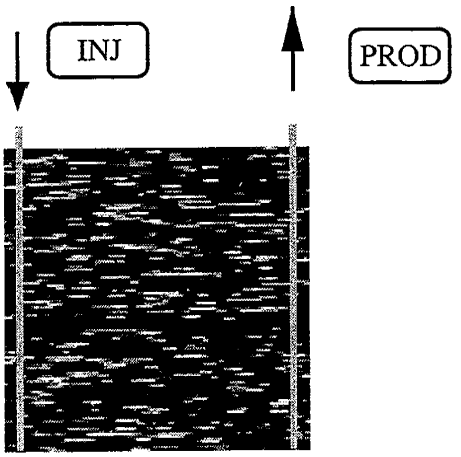

Figure 4.13: Permeability field containing 270×270 grid blocks with two facies. Permeability: $k(\text{black}) = 100\ mD$ and $k(\text{white}) = 0.1\ mD$. Proportion of black facies: 90%. Correlation length: 20 grid blocks in the x and 2 grid blocks in the y direction.

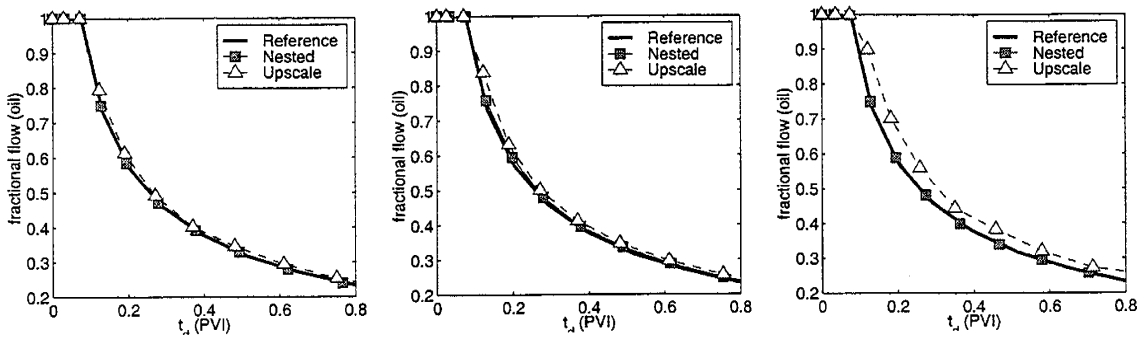

(a) (3×3) (b) (9×9) (c) (27×27)

Figure 4.14: Fractional flow of oil at the producer for different upscaling factors and for the three methods (fine grid, nested gridding and upscaling). Case *RES2*

layered permeability field on the (x, z) plane containing two facies with $n_x = n_y = 270$ grid blocks, $l_{cx} = 20$ $l_{cz} = 2$ (in grid block units). The proportions and permeability of the two facies are similar to the case *RES1*.

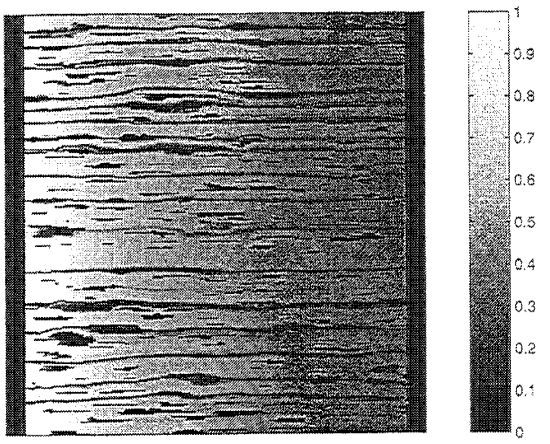

(a) Fine grid simulation

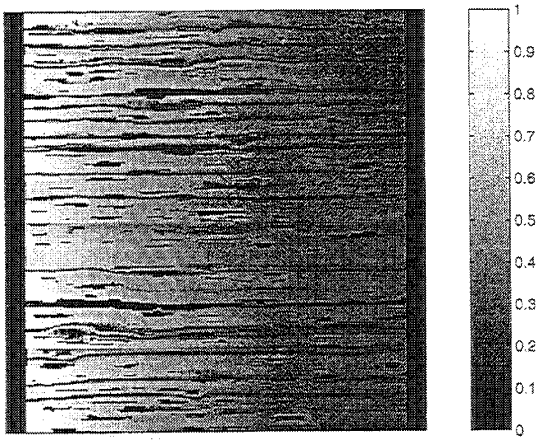

(b) Nested gridding method

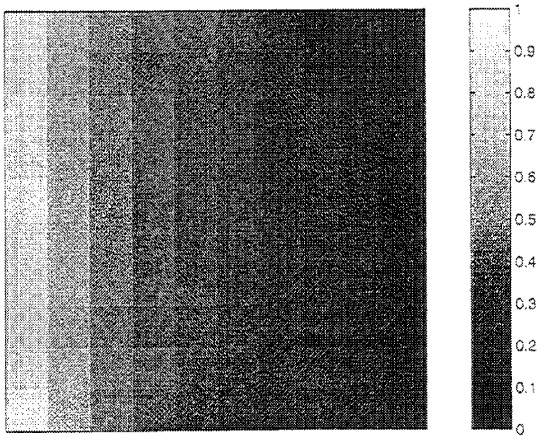

(c) Upscaling method

Figure 4.15: Water saturation maps from the fine grid simulation *(a)*, from the nested gridding simulation *(b)* and from the simulation on the upscaled absolute permeabilities *(c)* for 0.8 PVI. The upscaling factor is 27×27. Case *RES2*

Table 4.2: Speed-up factor and memory requirements of the nested grid method for a pressure solve and for the whole simulation on the two *2D* examples presented in the chapter.

	Upscaling factor	**Speed-up factor**		**Memory**	
		P solve	sim	RAM	% saved
RES1	3×3	3.8	1.2	19	61
	9×9	4.3	1.5	13	73
RES2	3×3	5.6	2.1	19	61
	9×9	6.2	1.6	13	73

Water is injected from the left well and oil is produced from the right. A constant pressure difference is prescribed between the two wells which are fully penetrating. Gravity is neglected. Production curves are shown in Figure 4.14 for the three methods and for three upscaling factors (3×3, 9×9 or 27×27 fine grid blocks). We can see that as the grid is coarsened the results from upscaling get worse. In contrast, nested gridding gives results almost identical to fine grid simulation, even for high upscaling factors. To understand better this behavior we present in Figure 4.14 three maps representing the saturation for 0.7 PVI derived from the three different simulations with an upscaling factor equal to 27×27. The preferential flow paths induced by the permeability pattern are well represented by the nested gridding method since it retains an explicit description of the saturation distribution on the fine grid. The upscaling method gives poor results with an overly smooth saturation profile. Thus fine grid details are not taken into account.

Table 4.2 shows the CPU time and memory comparisons for the nested gridding method and the classical streamline method. The multigrid solver was used to compute the pressure field for the reference case. The average speed-up factor for the pressure solve is 5 and decreases to 1.5 for the entire simulation. This is because there are no time savings for tracing streamlines and moving saturations, since these steps are performed on the fine grid. Up to 73% of the memory is saved since we don't have to store the transmissivity matrix related to the fine grid ($N \times m$ grid blocks) but only the transmissivity matrix related to the coarse grid (N grid blocks) and to the fine grid within a coarse grid block (m grid blocks).

4.6.2 Numerical results for three-dimensional reservoirs

We will now present a *3D* example. We consider a $99 \times 99 \times 99$ permeability field containing two facies. Small low permeability clusters (0.1 mD), characterized by a correlation length of 2 grid blocks in every direction, are embedded into a matrix of higher permeability (100 mD). The proportion of the low permeability clusters is 20%. The permeability map and the well locations are represented in Figure 4.16.

In this *3D* example we will show two different results with and without gravity. We define for that purpose a gravity number which compares the relative contribution of the viscous forces over the gravity forces [22, 64]:

$$N_g = \frac{\Delta\rho \, g \, L^2}{\Delta P_h \, H} \tag{4.25}$$

where $\Delta\rho$ represents the density difference between water and oil, L^2 and ΔP_h are the distance and the pressure difference between the two wells and H is the height of the reservoir. We will consider the case where the gravity can be neglected ($N_g = 0$) and the case where the effects are important ($N_g = 2$).

Water is injected in the injector and we observe the oil fractional flow at the producer for $N_g = 0$ and 2 in Figure 4.17 and Figure 4.18 respectively. Clearly in all the cases, and for

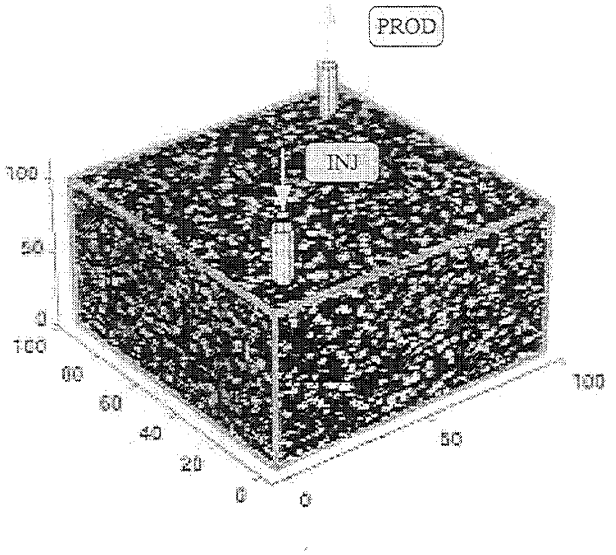

Figure 4.16: Case *RES3*. $99 \times 99 \times 99$ permeability field. The two wells are located on two opposing corners of the reservoir and they penetrate all the layers. The correlation length is equal to 2 grid blocks in all 3 directions. The permeability of the black facies is $100\,mD$ and $0.1\,mD$ for the white facies.

all the different upscaling factors, the nested gridding is more accurate than the upscaling which overestimated the breakthrough time and the overall oil production.

Figure 4.19 represents a zoom of the saturation maps for the case *RES3* when $N_g = 0$. The figure shows four slices of the *3D* array. Only one third of the reservoir is shown. The upper left corner represents the injector. Once again, we can see that the water front advance and fine grid details are accurately captured by the nested gridding method. The upscaling method gives a smoothed representation of the flow pattern.

Finally, saturation maps for the entire reservoir are presented for the case where $N_g = 2$ (Figure 4.20), which shows clearly the important effects of gravity which segregates the two fluids. Here, water which is denser than the oil preferentially moves to the bottom of the reservoir. Gravity effects are also well accounted by our method.

Table 4.3 compares the CPU time and memory requirements of the nested gridding simulation with the fine grid simulation for the *3D* examples. The multigrid solver was used to compute the pressure field for the reference case. In the third column, the numbers shown in parenthesis correspond to the case where gravity is considered. For the pressure solve, the speed-up factor can go up to 37 for an upscaling factor of 3 in all directions. Note that the maximum speed-up factor does not correspond to the maximum upscaling factor. The overall speed-up factor is only 8.5. This is because we have only modified the pressure solve. When adding gravity, the overall speed-up factor is approximately halved mainly due to an additional step used to solve the saturation equation [7].

We have also performed CPU time comparisons between the nested gridding and the upscaling method for the *3D* examples. For a pressure solve, the upscaling method is about 5-7 times faster than nested gridding. For the whole simulation upscaling is between 30-60 times faster than nested gridding.

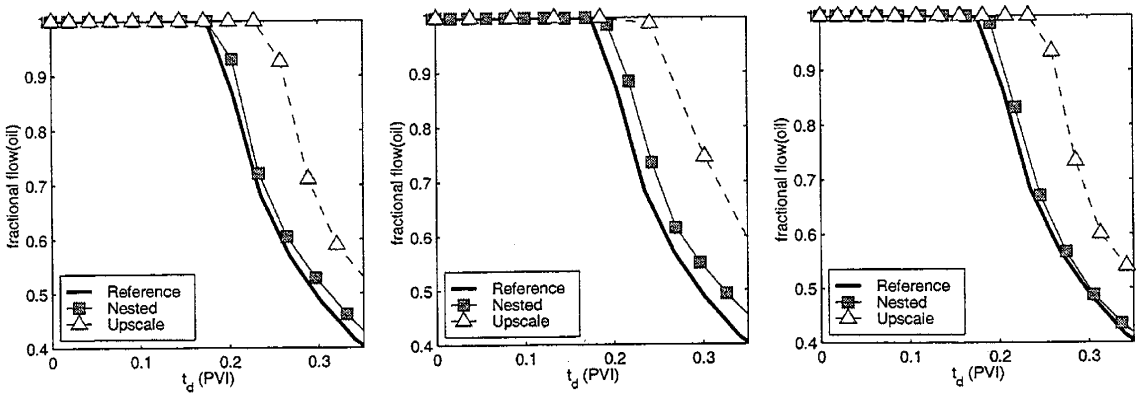

(a) $(3 \times 3 \times 1)$ (b) $(3 \times 3 \times 3)$ (c) $(9 \times 9 \times 3)$

Figure 4.17: Fractional flow of oil at the producer for different upscaling factors and for the three methods (fine grid, nested gridding and upscaling) for the case *RES3*. The gravity number is set to $N_g = 0$.

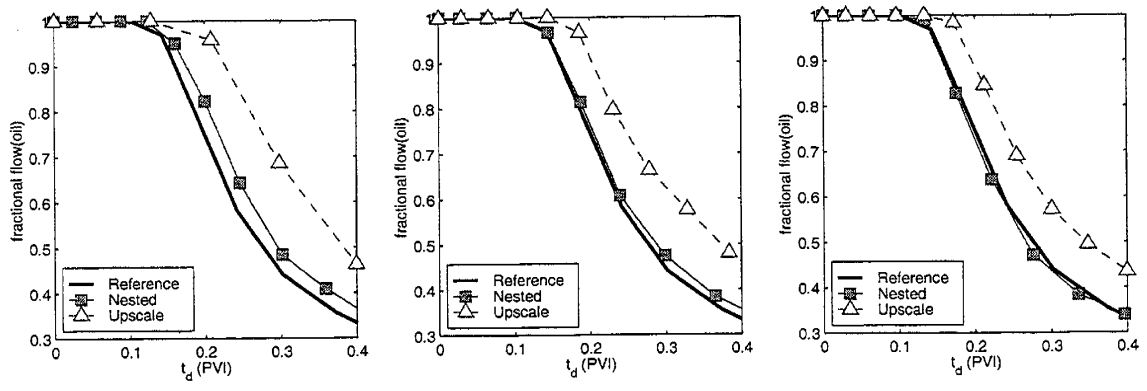

(a) $(3 \times 3 \times 1)$ (b) $(3 \times 3 \times 3)$ (c) $(9 \times 9 \times 3)$

Figure 4.18: Fractional flow of oil at the producer for different upscaling factors and for the three methods (fine grid, nested gridding and upscaling) for the case *RES3*. The gravity number is set to $N_g = 2$.

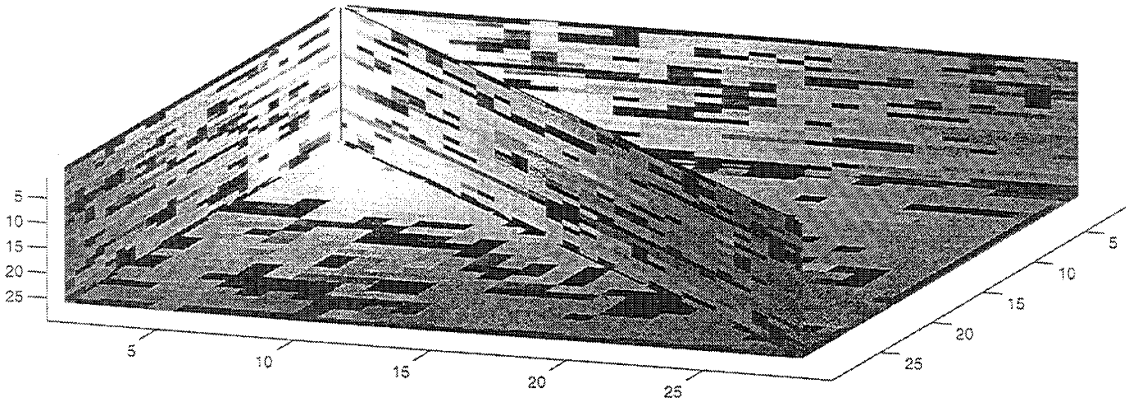

(a) Fine Grid

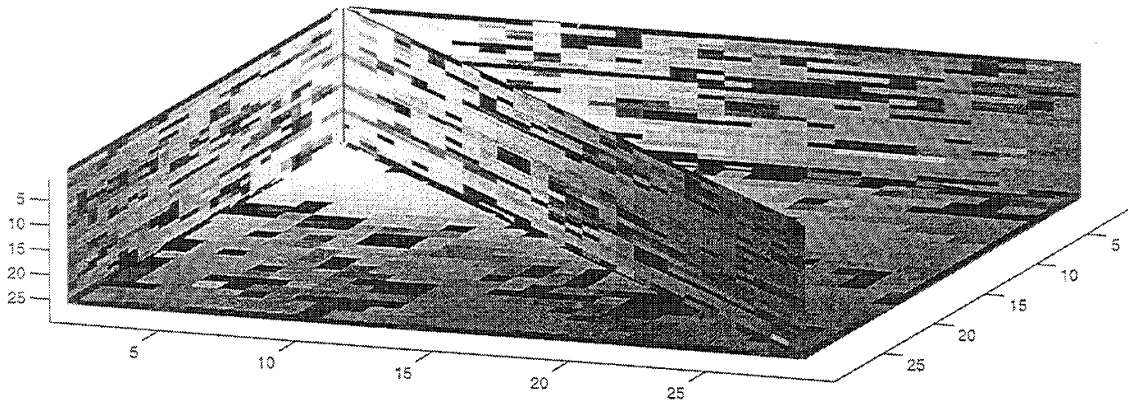

(b) Nested Gridding

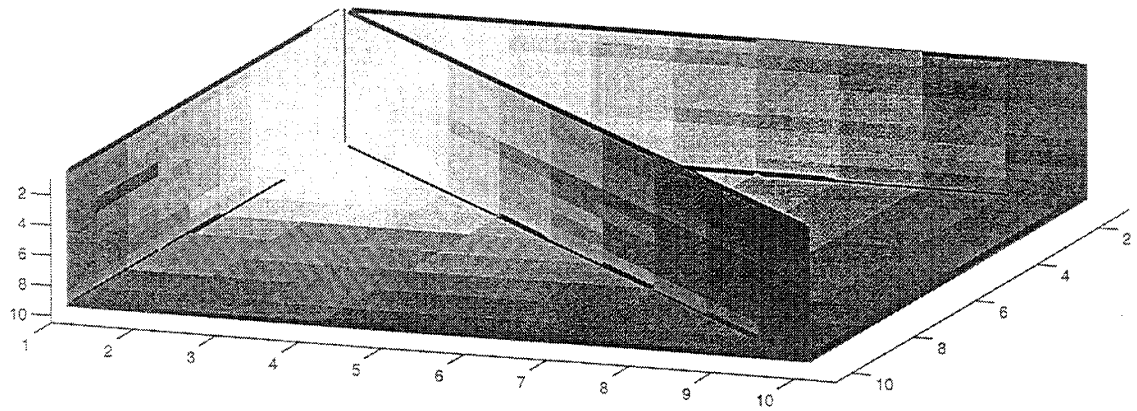

(c) Upscaling

Figure 4.19: Saturation maps for 0.15 PVI using the three methods (fine grid, nested gridding and upscaling) with an upscaling factor equal to $(3 \times 3 \times 3)$. The gravity number is set to $N_g = 0$

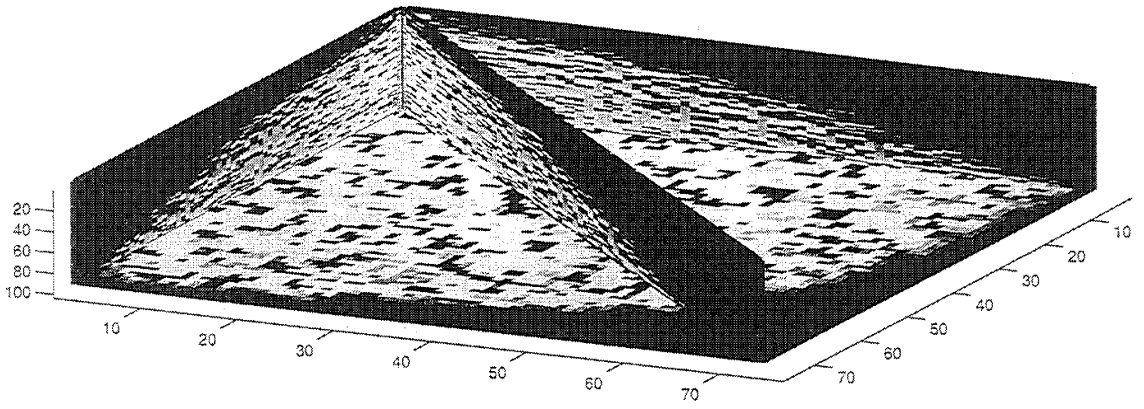

(a) Fine Grid

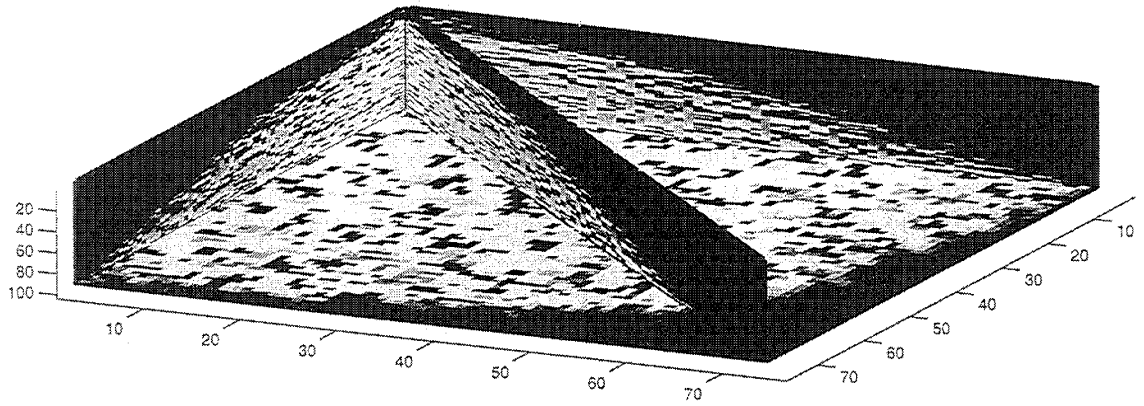

(b) Nested Gridding

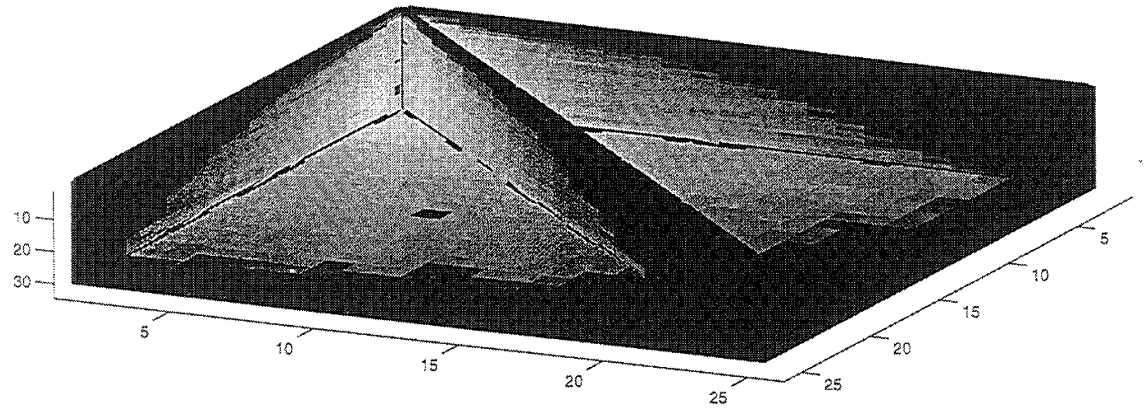

(c) Upscaling

Figure 4.20: Saturation maps for 0.15 PVI using the three methods (fine grid, nested gridding and upscaling) with an upscaling factor equal to $(3 \times 3 \times 3)$. The gravity number is set to $N_g = 2$

Table 4.3: Speed-up factor and memory requirements of the nested gridding method for a pressure solve and for the whole simulation on the *3D* example presented in the chapter. The numbers in parenthesis in the third column are speed-up factors for the case where $N_g = 2$

	Upscaling factor	**Speed-up factor**		**Memory**	
		P solve	sim	RAM	% saved
RES3	$3 \times 3 \times 1$	14	5.8 (3)	200	20
	$3 \times 3 \times 3$	37	8.5 (4)	164	35
	$9 \times 9 \times 3$	17	6.2 (3)	146	42
	$9 \times 9 \times 9$	2.2	2.1	150	40

4.7 Discussion and conclusions

We have proposed an approximate method, using nested gridding, to estimate recovery directly from a fine grid. We showed some simple examples that demonstrated that the method was more accurate than using coarse grid simulation with upscaled permeabilities, while being faster than direct fine grid simulation.

The method used streamline-based simulation to move the saturations on the fine grid. For large *3D* problems it has been shown previously that streamline-based simulation is up to 100 times faster than conventional finite difference methods [7]. Our nested gridding method is almost up to another factor of 8.5 faster for large problems giving an overall speed-up up to 850 while retaining reasonable accuracy.

While the nested gridding method has been shown to give accurate results for the cases studied, the speed-up compared with direct fine-scale simulation is modest. This is because the transport of fluid along streamline on the fine grid dominates the overall CPU time for large *3D* problems. Our streamline code has not been optimized, however. Furthermore the movement of fluid along streamlines is easy to implement in parallel, offering potentially substantial time savings.

Many upscaling techniques are applicable only to a given set of boundary conditions (well rate or locations) [14]. The nested gridding method, since it retains an explicit representation of the saturation distribution on the fine grid, automatically accommodates changing well rates and location.

References

[1] Adamson, A.W.: *Physical Chemistry of Surfaces*, John Wiley and Sons, NY, NY (1990).

[2] Amott, E.: "Observations Relating to the Wettability of a Porous Rock," *Trans. AIME* (1959) **216**, 156–162.

[3] Anderson, E., Bai, Z., Bischof, C., Demmel, J., Dongarra, J., Croz, J. D., Greenbaum, A., Hammarling, S., McKenney, A., Ostrouchov, S., and Sorensen, D.: *LAPACK Users' Guide*, Siam (1992).

[4] Aziz, K. and Settari, A.: *Petroleum Reservoir Simulation*, Applied Science Publishers, London (1979).

[5] Baker, L.E.: "Three-Phase Relative Permeability Correlations," paper SPE 17369 in the proceedings of the 1988 Sixth SPE/DOE Symposium on Enhanced Oil Recovery, Tulsa, OK, April.

[6] Barker, J. and Thibeau, S.: "A critical review of the use of pseudo relative permeabilities for upscaling," SPE 1996 European 3D Reservoir Modelling Conference, Stavanger (April 1996) No. SPE 35491.

[7] Batycky, R.P., Blunt, M.J., and Thiele, M.R.: "A 3D Field Scale Streamline Simulator With Gravity and Changing Well Conditions," *SPE Reservoir Engineering* (November 1997) **11**, No. 4.

[8] Batycky, R.P., Thiele, M.R., and Blunt, M.J.: "A Streamline Simulator to Model Field Scale, Three-Dimensional Flow," Proc. of the 5th European Conference on the Mathematics of Oil Recovery, Leoben, Austria (Sept. 3–6 1996).

[9] Begg, S., Carter, R., and Dranfield, P.: "Assigning Effective Values to Simulator Gridblocks Parameters for Heterogeneous Reservoirs," *SPE Reservoir Engineering* (1989) **4**, 455–463.

[10] Blunt, M.J., Liu, K., and Thiele, M.R.: "A Generalized Streamline Method to Predict Reservoir Flow," *Petroleum Geosciences* (August 1996) **2**, 259–269.

[11] Blunt, M.J., Zhou, D. and Fenwick, D.H.: "Three-Phase Flow and Gravity Drainage in Porous Media," *Transport in Porous Media* (1995) **20**, 77–103.

[12] Buckley, J.S. and Liu, Y.: "Some Mechanisms of Crude Oil/Brine/Solid Interactions," *Journal of Petroleum Science and Engineering* (1998) **20**, 155–160.

[13] Buckley, J.S., Liu, Y., Xie, X. and Morrow, N.R.: "Asphaltenes and Crude Oil Wetting - The Effect of Oil Composition," *SPE Journal* (1997) **2**, 107–119.

[14] Christie, M.: "Upscaling for Reservoir Simulation," *Journal of Petroleum Technology* (Nov 1996) **48**, 1004–1008.

[15] CRC Press, Inc., West Palm Beach, Florida, *CRC Handbook of Chemistry and Physics*, 61st edition (1981).

[16] Deutsch, C. and Journel, A.: *Geostatistical Software Library and User's Guide*, Oxford University Press (1992).

[17] DiCarlo, D.A., Sahni, A., and Blunt, M.J.: "The Effect of Wettability on Three-Phase Relative Permeability," to be published in Transport in Porous Media.

[18] Dindoruk, B.: *Analytical Theory of Multiphase, Multicomponent Displacement in Porous Media*, PhD dissertation, Stanford University, Stanford, CA (1992).

[19] Dindoruk, B., Orr, F.M., Jr. and Johns, R.T.: "Theory of Multicontact Miscible Displacement with Nitrogen," *SPE Journal* (1997) **2**, 268–279.

[20] Dullien, F.: *Porous Media: Fluid Transport and Pore Structure*, Academic Press, San Diego, CA (1992).

[21] Dumoré, J.M. and Schols, R.S.: "Drainage Capillary Functions and the Influence of Connate Water," *SPE Journal* (1974) **14**, 437–444.

[22] Fayers, F. and Muggeridge, A.: "Extensions to Dietz Theory and Behaviour of Gravity tongues in Slightly Tilted Reservoirs," SPERE (Nov 1990) **5**, 487–494.

[23] Fayers, F.J. and Matthews J.D.: "Evaluation of Normalized Stone's Methods for Estimating Three-Phase Relative Permeabilities," *SPE Journal* (1984) **24**, 224–232.

[24] Fenwick, D.H. and Blunt, M.J.: "Network Modeling of Three-Phase Flow in Porous Media," *SPE Journal* (1998) **3**, 86–97.

[25] Firincioglu, T., Blunt, M.J. and Zhou, D.: "Three-Phase Flow and Wettability Effects in Triangular Capillaries," *Colloids and Surfaces A* (1999) **155**, 259–276.

[26] Gautier, Y. and Nœtinger, B.: "Preferential flow-paths detection for heterogeneous reservoir using a new renormalization technique," *Transport in Porous Media* (1997) **26**, 1–23.

[27] Grader, A.S., and O'Meara, D.J., Jr.: "Dynamic Displacement Measurements of Three-Phase Relative Permeabilities Using Three Immiscible Liquids," paper SPE 18293 in the proceedings of the 1992 SPE Annual Technical Conference and Exhibition, Houston, TX, Oct. 2–5.

[28] Guedes, S. and Schiozer, D.: "An Implicit Treatment of Upscaling in Numerical Simulation," SPE Symposium on Reservoir Simulation, Houston (1999) No. 51937.

[29] Guérillot, D. and Verdière, S.: "Different Pressure Grids for Reservoir Simulation in Heterogeneous Reservoirs," 1995 SPE Symposium on Reservoir Simulation, San Antonio, No. 29148.

[30] Helfferich, F.G.: "Theory of Multicomponent, Multiphase Displacement in Porous Media," *SPE Journal* (February 1981) **271**, 51–62.

[31] Hou, T. and Wu, X.: "A multiscale finite element method for elliptic problems in composite materials and porous media," *Journal of Computational Physics* (1997) **134**, No. CP975682, 169–189.

[32] Jerauld, G.R.: "Prudhoe Bay Gas/Oil Relative Permeability," *SPE Reservoir Engineering* (1997) **12**, 66–73.

[33] Jessen, K., Michelsen, M.L. and Stenby, E.H.: "Global Approach for Calculation of Minimum Miscibility Presure," *Fluid Phase Equilibria* (1998) **153**, 251–263.

[34] Johns, R.T. and Orr, F.M., Jr.: "Miscible Gas Displacement of Multicomponent Oils," *SPE Journal* (1996) **1**, 39–50.

[35] Johns, R.T., B. Dindoruk, and Orr, F.M. Jr.: "Analytical Theory of Combined Condensing/Vaporizing Gas Drives," *SPE Advanced Technology Series* (May 1993) **1**, No. 2, 7–16.

[36] Johns, R.T., Fayers, F.J. and Orr, F.M., Jr.: "Effect of Gas Enrichment and Dispersion on Nearly Miscible Displacements in Condensing/Vaporizing Drives," *SPE Advanced Technology Series* (1994) **2**, No. 2, 173–180.

[37] Kantzas, A., Chatzis, I. and Dullien, F. A. L.: "Enhanced Oil Recovery by Inert Gas Injection," paper SPE 17379 in the proceedings of the 1988 Sixth SPE/DOE Symposium on Enhanced Oil Recovery, Tulsa, OK, April.

[38] Keller, A.A., Blunt, M.J. and Roberts, P.V.: "Micromodel Observation of the Role of Oil Layers in Three Phase Flow," *Transport in Porous Media* (1997) **26**, 277–297.

[39] Kincaid, D. R., Respess, J., and Young, D.: *ITPACK 2C: A FORTRAN Package for Solving Large Sparse Linear Systems by Adaptative Accelerated Iterative Methods*, University of Texas, Austin (1997).

[40] King, P.: "The Use of Renormalization for Calculating Effective Permeability," *Transport in Porous Media* (1989) **4**, 37–58.

[41] Kovscek, A.R., Wong, H. and Radke C.J.: "A Pore-Level Scenario for the Devolpment of Mixed Wettability in Oil Reservoirs," *AIChE J.* (1993) **39**, 1072–1085.

[42] Kumar, A. and Jerauld, G.: "Impacts of Scale-up on Fluid Flow from Plug to Gridblock Scale in Reservoir Rock," 10th SPE/DOE Symposium on Improved Oil Recovery, Tulsa (April 1996) No. SPE 35452.

[43] Lohrenz, J., Bray, B.C. and Clark, C.R.: "The Viscosity of Pure Substances in Dense Gaseous and Liquid Phases," *Journal of Petroleum Technology* (Oct. 1964) **16**, 1171–1176.

[44] Michelsen, M.L.: "Speeding up the Two-Phase PT-Flash with Applicatioon for Calculation of Miscible Displacements," *Fluid Phase Equilibria* (1998) **143**, 1–12.

[45] Monroe, W.W., Silva, M.K., Larsen, L.L. and Orr, F.M. Jr.: "Composition Paths in Four-Component Systems: Effect of Dissolved Methane on 1D CO_2 Flood Performance," *SPE Reservoir Engineering* (August 1990) **5**, 423–432.

[46] Naylor, P., Sargent, N.C., Crosbie, A.J., Tilsed A.P. and Goodyear S.G.: "Gravity Drainage During Gas Injection," proceedings of the 8th European IOR Symposium in Sydney, Australia (May 15–17 1995).

[47] Oak, M.J., Baker, L.E. and Thomas, D.C.: "Three-Phase Relative Permeability of Berea Sandstone," *Journal of Petroleum Technology* (1990) **42**, 1057–1061.

[48] Øren, P. E. and Pinczewski, W. V.: "The Effect of Wettability and Spreading Coefficients on the Recovery of Waterflood Residual Oil by Miscible Gasflooding," paper SPE 24881 in the proceedings of the 1992 SPE Technical Conference and Exhibition, Washington, D.C.

[49] Øren, P.-E., Bakke, S. and Arntzen, O.J.: "Extending Predictive Capabilities to Network Models," *SPE Journal* (1998) **3**, 324–336.

[50] Øren, P.E. and Pinczewski, W.V.: "Fluid Distribution and Pore Scale Displacement Mechanisms in Drainage Dominated Three-Phase Flow," *Transport in Porous Media* (1995) **20**, 105–133.

[51] P. Renard, G. d. M.: "Calculating Equivalent Permeability: A Review," *Advances in Water Resources* (1997) **20**, 253–278.

[52] Peaceman, D.: "Interpretation of Well-Block Pressures in Numerical Reservoir Simulation," *SPEJ* (June 1978) **18**, 183–194.

[53] Peaceman, D.: "Effective Transmissibilities of a Gridblock by Upscaling-Comparison of Direct Methods with Renormalization," *SPEJ* (1997) **2**, 338–349.

[54] Pedersen, K.S., Fredenslund, A.A. and Thomassen, P.: *Properties of Oils and Natural Gases*, Gulf Publishing Company, Houston, TX (1989).

[55] Pickup, G. and Sorbie, K.: "The Scaleup of Two-Phase Flow in Porous Media Using Phase Permeability Tensors," *SPEJ* (1996) **1**, 369–381.

[56] Pollock, D.: "Semianalytical Computation of Path Lines for Finite Difference Models," *Ground Water* (Nov-Dec 1988) **26**, No. 6, 743–750.

[57] Ramé, M. and Killough, J.: "A New Approach to the Simulation of Flows in Highly Heterogeneous Porous Media," 1991 SPE Symposium on Reservoir Simulation, Anaheim, No. 21247.

[58] Sahni, A., Burger, J.E. and Blunt, M.J.: "Measurement of Three Phase Relative Permeability during Gravity Drainage using CT Scanning," paper SPE 39655 in the proceedings of the 1998 SPE/DOE Improved Oil Recovery Symposium, Tulsa, OK, April.

[59] Salathiel, R.A.: "Oil Recovery by Surface Film Drainage in Mixed Wettability Rocks," *Journal of Petroleum Technology* (1973) **25**, 1216–1224.

[60] Skauge, A., Eleri, O. O., Graue, A. and Monstad, P.: "Influence of Connate Water on Oil Recovery by Gravity Drainage," paper SPE 27817 in the proceedings of the 1994 SPE/DOE Symposium on Improved Oil Recovery, Tulsa, OK, Apr. 17–20.

[61] Soll, W.E., Celia, M.A. and Wilson, J.L.: "Micromodel Studies of Three-Fluid Porous Media Systems: Pore-Scale Processes Relating to Capillary Pressure-Saturation Relationships," *Water Resources Research* (1993) **29**, No. 9, 2963–2974.

[62] Stone, H.L.: "Probability Model for Estimating Three-Phase Relative Permeability," *Journal of Petroleum Technology, Trans. AIME* (1970) **249**, 214–218.

[63] Stueben, K.: "Algebraic Multigrid (AMG): Experiences and Comparisons," *Appl. Math. Comp. Proceedings of the International Multigrid Conference* (1983) **13**, 419–452.

[64] Tchelepi, H. and Orr, F.M., J.: "Interaction of Viscous Fingering, Permeability Heterogeneity, and Gravity Segregation in Three Dimensions," *SPE Reservoir Engineering* (November 1994) **9**, No. 4, 266–271.

[65] Thiele, M.R., Batycky, R.P., and Blunt, M.J.: "A Streamline-Based 3D Field-Scale Compositional Reservoir Simulator," paper SPE 38889 in the proceedings of the 1997 SPE Annual Technical Conference and Exhibition, San Antonio, TX, Oct. 5–8.

[66] Thiele, M.R., Batycky, R.P., Blunt, M.J., and Orr, F.M.: "Simulating Flow in Heterogeneous Media Using Streamtubes and Streamlines," *SPE Reservoir Engineering* (February 1996) **10**, No. 1, 5–12.

[67] Verdière, S. and Guérillot, D.: "Dual Mesh Method in Heterogeneous Porous Media," 5th European Conference on the Mathematics of Oil Recovery, Leoben (Sept. 1996).

[68] Verdière, S. and Vignal, M.: "Numerical and Theoretical study of a dual mesh method using finite volume schemes for two phase flow problems in porous media," *Numerische Mathematik* (1998) **80**, 601–639.

[69] Vizika, O. and Lombard, J-M.: "Wettability and Spreading: Two Key Parameters in Oil Recovery With Three-Phase Gravity Drainage," *SPE Reservoir Engineering* (1996) **11**, 54–60.

[70] Wang, Y. and Orr, F.M., Jr.: "Analytical Calculation of Minimum Miscibility Presure," *Fluid Phase Equilibria* (1997) **139**, 101–124.

[71] Wang, Y. and Orr, F.M., Jr.: "Calculation of Mininum Miscibility Pressure," paper SPE 39683 in the proceedings of the 1998 SPE/DOE Symposium on Improved Oil Recovery, Tulsa, OK, Apr. 19–22.

[72] Zhou, D. and Blunt, M.J.: "Effect of Spreading Coefficient on the Distribution of Light Non-Aqueous Phase Liquid in the Subsurface," *Journal of Contaminant Hydrology* (1997) **25**, 1–19.

[73] Zhou, D. and Blunt, M.J.: "Wettability Effects in Three-Phase Gravity Drainage," *Journal of Petroleum Science and Engineering* (1998) **20**, 203–211.

[74] Zhou, D., Blunt, M.J. and Orr, F.M., Jr.: "Hydrocarbon Drainage Along Corners of Noncircular Capillaries," *Journal of Colloid and Interface Science* (1997) **187**, 11–21.